2018

3D Visualization and Interactive Image Manipulation for Surgical Planning in Robot-assisted Surgery

Mohammadreza Maddah
Wright State University

3D Visualization and Interactive Image Manipulation for Surgical Planning in Robot-assisted Surgery

A Dissertation submitted in partial fulfillment
of the requirements for the degree of
Doctor of Philosophy

By

Mohammadreza Maddah
B.S. University of Tehran, Iran, 1999
M.S. Semnan University, 2011

2018
Wright State University

Wright State University
Graduate School

April 27, 2018

    I HEREBY RECOMMEND THAT THE DISSERTATION PREPARED UNDER MY SUPERVISION BY <u>Mohammadreza Maddah</u> ENTITLED <u>3D Visualization and Interactive Image Manipulation for Surgical Planning in Robot-assisted Surgery</u> BE ACCEPTED IN PARTIAL FULLFILMENT OF THE REQUIREMENTS FOR THE DEGREE OF <u>Doctor of Philosophy</u>.

<div align="right">

_____

Caroline. G.L. Cao, Ph.D.
Dissertation Director

_____

Frank W. Ciarallo, Ph.D.
Director, Ph.D. in Engineering Program

_____

Barry Milligan, Ph.D.
Professor and Interim Dean of the
Graduate School

</div>

Committee on
Final Examination

_____
Caroline. G.L. Cao, Ph.D.

_____
Thomas Wischgoll, Ph.D.

_____
Zach Fuchs, Ph.D.

_____
Xinhui Zhang, Ph.D.

_____
Cedric Dumas, Ph.D.

ABSTRACT

Maddah, Mohammadreza. Ph.D., Engineering Ph.D. Program, Department of Biomedical, Industrial, and Human Factors Engineering, Wright State University, 2018. 3D visualization and interactive image manipulation for surgical planning in robot-assisted surgery.

Robot-assisted surgery, or "robotic" surgery, has been developed to address the difficulties with the traditional laparoscopic surgery. The *da Vinci* (Intuitive Surgical, CA and USA) is one of the FDA-approved surgical robotic system which is widely used in the case of abdominal surgeries like hysterectomy and cholecystectomy. The technology includes a system of master and slave tele-manipulators that enhances manipulation precision. However, inadequate guidelines and lack of a human-machine interface system for planning the ports on the abdomen surface are some of the main issues with robotic surgery. Unreachable target and mid-surgery collisions between robotic arms are the major problems that surgeons complain about in robotic surgery. The objective of this research is to design a new decision-support tool for planning port placement in robotic surgery. The decision-support system will be able to determine the optimal location of the entrance ports on the abdomen surface that is specific to the patient.

Contents

List of Figures

List of Tables

Acknowledgement

I dedicate this dissertation to my mother for nursing me with affections and love and her dedicated partnership for success in my life.

Chapter 1

Introduction

In robotic minimally invasive surgery (MIS), port placement is a pre-operative surgical procedure in which the surgeon makes three or four small incisions (ports) on the patient's body in the operating room [1]. The surgical instruments (including an endoscope to see inside the patient) are inserted into the patient's body through the ports, and the tools and the endoscope are connected to the robot arms, allowing the surgeon to perform the operation remotely. The most commonly used robot in MIS procedures is *da Vinci*, which has three main components: the robot (including three manipulators and one endoscope), a monitoring tower, and a console for controlling the robot manipulators through a master-slave telecommunication system [2]. In robotic MIS, the surgeon's ease of access to the diseased organ depends on the location of the ports on the patient's body. The patient's body—the abdominal or the thoracic cavities—is inflated with a gas (CO_2); this process is called pneumoperitoneum or insufflation. Due to insufflation, the patient's body shape (abdominal or chest surface) is deformed, and the target organ are usually moved and shifted from its original position. Thus, the surgeon needs to consider all these alterations in the patient's body shape, and the target organ, before planning the ports on the patient's body. This makes port placement a crucial task in most robotic laparoscopic procedures. Moreover, the robot's (manipulator's) position relative to the patient is another factor that has a direct impact on finding the optimal port locations on the patient's body. An optimal port placement must provide enough working volume for the surgical tools in the patient's body, and prevent the instruments from colliding frequently during surgery. Besides, it increases the

dexterity of the robot arms to manipulate the tools for reaching to the desired area inside the patient [3]. Surgeons usually use their experience about the target organ position for deciding about the optimal positions of the ports on the patient's body. However, because of the alterations in the abdominal shape and the target organ position after insufflation, the likelihood of wrong decisions (about the ports' positions) will increase when the robot is docked on the patient. Poor accessibility to the target organ, and insufficient vision of the diseased areas, are the reasons that even experienced surgeons may need to make several new incisions for the entry ports. This will cause the surgeon to feel exhausted in the operating room and increase trauma to the patient after surgery. Moreover, the results of a survey, conducted by researchers at Wright State University, showed the port placement is a challenging task for the surgeons in using the robotic system [4].

To date researchers have used various techniques (medical image processing and robot modeling) to come up with different solutions for optimal port placement in robotic surgery [5,6]. Most of the previous studies used a 3-dimensional pre-operative patient-specific model and a descriptive optimization algorithm for finding the optimal location of the entry ports. The goals of the optimization were to maximize the accessibility to the target organ and minimize a possible collision between the surgical instruments. However, the robot (*da Vinci Si*, Surgical Intuitive) was not modeled mathematically in those optimization algorithms. Instead, simple cylinders and spheres were used for the robot modeling [7]. Other researchers used a kinematics analysis to model the robot manipulators, and they measured the manipulators' performance by using performance indices that are defined in the field of robotics [8]. In another study, researchers simulated the patient's body with a small box for port placement. They introduced an efficiency index to determine the visibility of the operation area (inside the box) during surgery. Similar to the previous studies, an optimization algorithm was proposed for maximizing the performance and efficiency indices and simultaneously minimizing the collision between the instruments (in a small cubic box) [9].

To our knowledge, the use of all existing port placement systems is limited to certain MIS procedures such as coronary artery bypass surgeries [10]. Also, because of using pre-operative medical images, the significant changes in the body shape, and the organs' displacement (because of insufflation) were not foreseen in the design of such systems. Thus, most of the previously designed systems are not applicable for laparoscopic procedures such as hysterectomy or cholecystectomy in abdominal or pelvic cavities.

1.1   Motivation

The primary goal of this dissertation is to develop a more accurate port placement system to assist surgeons in planning the optimal ports on the patient's body. The system will be able to find the optimal locations of the ports based on the patient's body shape and the robot pose and configuration in the operating room. The

patient's body shape is usually altered because of some variations in the operating room such as tilting or changing the position of the operating table and the insufflation process. We will focus on some MIS procedures (specially hysterectomy procedures) where the ports' locations are significantly influenced by such changes in the operating room. We will use a 3D scanner (Kinect V2, Microsoft) for creating a patient-specific model to calculate the optimal locations of the ports, considering the robot position relative to the patient in the operating room.

1.2 Contributions

This dissertation includes three main contributions that improve the components of the current port placement systems (the patient-specific model, the optimization algorithm, and visualizing the optimal regions of the ports on the patient model) in robotic laparoscopic surgery. The three contributions are detailed in the following subsections.

1.2.1 Developing a comprehensive port placement system

In this dissertation, we present a comprehensive solution to the port placement problem that includes both the robot and the patient model (after insufflation) for finding the optimal location of the ports on the patient's body surface. The three components of our port placement system are the patient-specific model, the robot model, and the optimization algorithm. The following is a brief description of the port placement system.

We use a 3D range imaging camera (Kinect V2 version, Microsoft) for imaging the abdominal shape in the operating room and creating a 3D model of the patient's abdomen after insufflation, called the external model. Using pre-operative medical images, we create another 3D model of the patient's abdomen, called the internal model. The external and the internal model are aligned for positioning the target organ (operation area) in the external model, the result of the alignment is called the patient-specific model. Unlike the previous systems, this patient-specific model is a post-insufflation 3D shape of the abdomen (containing the target organ). Thus, our port placement system foresees the abdominal shape deformation, and the target organ's shift due to insufflation.

The constructed patient model is used for planning the ports with respect to the configuration and position of the robot arms. That is why we need to represent the robot arms' configuration in mathematical terms, called the robot model. We use D-H convention for modeling the robot arms (manipulators) [11]. Considering the target organ location in the patient model, the accessibility of the patient model to the robot manipulators is verified by solving an inverse kinematic equation [8]. The accessible points are marked and

highlighted on the patient model. Then, the performance index of the robot manipulators at each accessible point (on the patient model) is calculated. We select the points whose index is greater than a specific threshold (these points are called the preliminary points for each of the robot manipulators); the rest of the points are filtered out from the further optimization process.

The preliminary ports for each of the manipulators are given to an optimization algorithm for selecting the optimal ports' locations on the patient model. For every combination of four ports from the preliminary points, the optimization algorithm calculates the collision between the tools (an efficiency index [9]) and decides about the optimal ports based on Pareto efficiency [12].

1.2.2   Measuring the organs' motion due to insufflation

In laparoscopic surgery, increasing abdominal pressure (because of insufflation) provokes morphological changes in the abdominal organs [13]. However, the impact of gas pressure on the abdominal organs' motion (displacement) are still unknown. Using four female pigs in the actual condition of insufflation, we measure the abdominal organs' displacement under gas pressure in Chapter 3. The measured organs' shift (in the animal study) are used to estimate the target organ shift in the human body after insufflation. Also, we show that the organs' motion can change the ports' location on the abdominal surface.

1.2.3   Reducing the need for pre-operative medical images

As explained in section 1.2.1, the patient model is constructed from 3D depth images, captured by a 3D scanner in the operating room, and from pre-operative computed tomography (CT) scans. The purpose of using CT scans and the result of the animal study (for estimating the organs' shift) is to position the target organ in the patient model. However, we still need to reduce the dependence of the system on the multiple inputs (CT and range imaging scanner) in the design of the port placement system. With a sufficient number of the subjects (seven patient models), we can predict and estimate the location of the target area (in the patient model) without using pre-operative medical images. In other words, the need for using the pre-medical images can be eliminated in our port placement system. We use the target organ (operation area) information (size and position) from seven patients to estimate the size and position of the operation area in a patient model without the target organ embedded.

1.3 Outline of Dissertation

In Chapter 2 we review the literature on MIS and robotic surgery. In addition, we provide background material about previous port placement systems. In Chapter 3 we present our comprehensive solution to the

port placement problem, including the patient model, the robot model, and the optimization algorithm. In Chapter 4 we show the results of our port placement system for finding the optimal locations on four different patients who underwent a hysterectomy procedure. In Chapter 5 we validate the results of the port placement system on a body phantom. Moreover, we verify reducing the need for pre-operative medical images in the design of our port placement system. Finally, in Chapter 6 we summarize the dissertation and offer some thoughts regarding follow-on research in this area.

Chapter 2

Background and Research Objectives

2.1   Literature Review

2.1.1 Laparoscopic Surgery

In conventional open surgery, a big incision is made on the patient's body, the surgeon inserts the instruments into the patient's body and performs the surgery. The surgical field (operation area inside the patient) is accessible to the instruments, and the surgeon can visualize, handle, and manipulate the tissues directly. Long post-operative recovery and delayed hospital discharge are the most well-known disadvantages of open surgery.

Considering the disadvantages of traditional open surgery, there is also a tremendous patient demand for improved cosmesis, which has caused open surgery in thoracic and pelvic cavities to be gradually replaced by minimally invasive surgery (MIS) [13, 14]. MIS is a surgical procedure that is performed through three or four small incisions (entry ports) on the patient's body. The surgical tools are inserted into the patient (through the incisions), and the surgeon can manipulate the tools to remotely access the desired region in the patient's body. One of the tools is dedicated to a high-quality video camera (called the

endoscope) for visualizing the surgical site (inside the patient) through a monitoring system in the operating room. Depending on the type of surgery, the surgical tools can perform different surgical tasks such as tissue dissection, clipping, suturing different parts of the target organs, and cauterizing the blood vessels.

MIS procedures in the abdominal and pelvic cavities are called laparoscopic surgery. Laparoscopic surgery has been developed since the first successful cholecystectomies were carried out by Lukichev, Muhe, and Mouret in 1983-1987 [15]. Since then, laparoscopic surgery has been the mostly used method for operations in the abdominal and pelvic cavities. Hysterectomy, cholecystectomy, and prostatectomy are three examples of well-established laparoscopic procedures for removing the uterus, gallbladder, and prostate from the patient's body [16,17].

In laparoscopic surgery, the surgeon determines the location of the incisions (ports) on the abdominal surface for inserting small plastic tubes (called trocars) into the patient's abdomen as shown in Figure 2.1. The diameter of the trocars is between 11~15 mm. Trocars are placed within the incisions for guiding the rigid surgical instruments and the endoscope toward the diseased area in the abdominal or pelvic cavity. The endoscope provides a magnified view of the instruments and anatomy for the surgeon during surgery as shown in Figure 2.1.
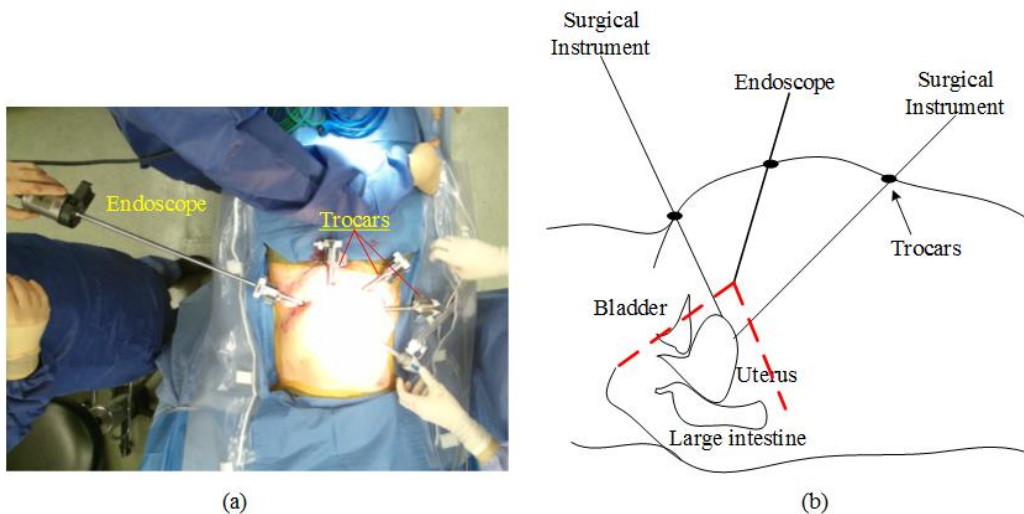
Figure 2.1 (a) The arrangement of the endoscope and surgical instruments in a laparoscopic surgery
(b) a schematic of a hysterectomy procedure for removing the uterus from the patient's body

After planning the ports on the abdominal surface, the space within the abdominal or thoracic cavity is inflated with gas (carbon dioxide) through a process called insufflation, or pneumoperitoneum. A Veress needle is a special spring-loaded needle used in the insufflation for injecting carbon dioxide into the abdominal cavity. Insufflation creates an intra-abdominal pressure (IAP) (10 to 15 mm Hg) that provides a larger working volume for the surgical tools during surgery.

2.1.1.1 Advantages and disadvantages

Many papers report the benefits of laparoscopic surgery as compared to traditional laparotomy [18,19]. Shorter hospital stay, less bleeding during surgery, and faster rehabilitation are some of the significant advantages of laparoscopic surgery. In addition, most patients who underwent laparoscopic surgery experience less post-operative discomfort, pain and trauma.

Lack of tactile perception and restricted 2D vision of the endoscope are the most common issues with laparoscopic surgery [20]. The 2D monitoring of the surgical site cannot provide a depth perception of the target anatomy for the surgeon. Moreover, the endoscope is held by an assistant in the operating room and the camera is unstable during surgery. This may cause the surgeon and the assistant to feel more fatigued during the operation. This poor ergonomic situation for the surgeon is another disadvantage of the traditional laparoscopic surgery.

In traditional laparoscopic surgery, the surgical tools have a few degrees of freedom (movements) in the surgical site inside the patient. There are no wrist movements at the tools' tips for performing surgical tasks such as suturing in a tiny space of the surgical site.

Recent studies have reported several complications of laparoscopic procedures [21, 22, 23]. Most of the complications were related to the entry technique and injuries during operation [23]. Margina et al. summarized and reported the complications associated with inserting the surgical tools, pneumoperitoneum, and operative procedures [24]. The injuries related to the entry of instruments (used for establishing IAP) into the patient's abdomen are outlined as follows:

- Bowel injuries
- Urinary tract injuries
- Ureteral injuries
- Bladder injuries
- Abdominal wall vascular injuries
- Major blood vessel injuries
- Hernia at the site of the abdominal wall trocar

Misplacement of the ports may lead to some or all of the above complications. Therefore, planning incisions on the abdominal surface is a challenging task for surgeons in laparoscopic procedures. The difficulty comes from different patients' body size (and anatomic structure) that makes it hard to establish a standard decision-making guideline to choose the right position of the ports.

2.1.2 Robotic Surgery

Robot-assisted surgery, or "robotic" surgery, has been developed to address the difficulties with traditional laparoscopic surgery. The *da Vinci* (Intuitive Surgical, CA and the USA) is one of the FDA-approved surgical robotic system that is widely used in gynecological (e.g. hysterectomy and cholecystectomy) and gastrointestinal procedures [2]. The system consists of three major components: an ergonomically designed console (including a 3D HD vision system) where the surgeon sits while operating, a patient-side cart where the patient is positioned during surgery, and interactive robotic arms (three manipulators and one endoscope arm). The console contains a user interface for visualizing the surgical site, and two grips for controlling the robot manipulators through a telecom system. The robotic part is a complex of four slave arms (manipulators), three are manipulators and one is dedicated to an endoscopic camera [2]. Each of the robot manipulators consists of a mechanical chain of links and joints. The links are connected through the joints, and the trocars, on the patient's abdominal surface, are attached to the last link of the manipulators. A *da Vinci Si* model is shown in Figure 2.2.
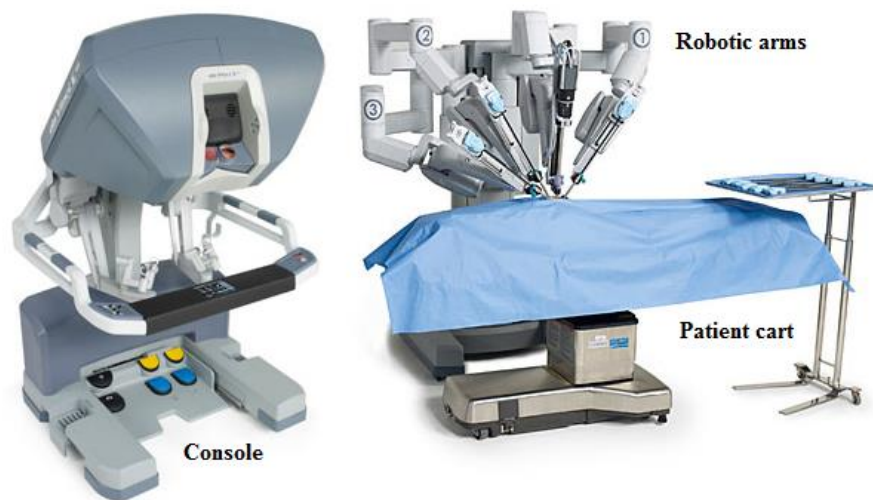
Figure 2.2 *da Vinci Si* HD surgical system [2]

9
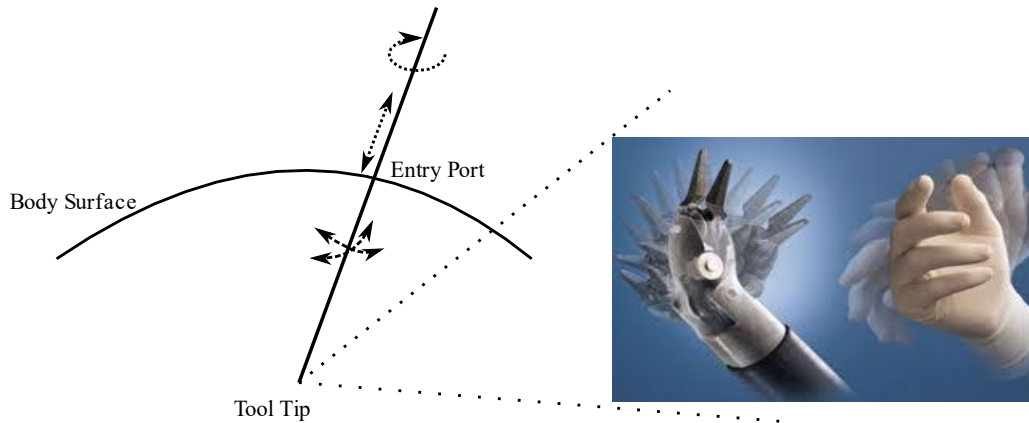
Figure 2.3 Left: Four degrees of freedom at the entry port (three rotations and one translation)
Right: *da Vinci* Endo-Wrist design of the surgical tool tip [2].

The 3D stereo visualization system is equipped with a high-quality camera (and image processing equipment) that provides an immersive view (and consequently a depth perception) of the surgical fields for the surgeon [25]. This 3D vision system is a remarkable advantage over the 2D monitoring system that is used in conventional laparoscopic surgeries.

The *da Vinci* master-slave telecommunication system allows the surgeon's hand movements to translate precisely into the manipulators' tips in the operative landscapes. Besides, large hand movements can be scaled to micro motions of the tools' tips that are required in the smaller regions of an operation field. The surgical tools in robotic surgery have seven degrees of freedom (movements), three rotations and one translation at the entry port, and three rotations at the tool tip (called Endo-Wrist in *da Vinci* system) as shown in Figure 2.3. These three more rotations at the tool tip provide the surgeon with natural dexterity (similar to the wrist movements) in the surgical site.

In robotic surgery, the surgeon sits in front of the console in an ergonomic position and grasps the grips with the wrist and fingers positioned naturally relative to his or her body. The ergonomic and remote design of the workstation (behind the console) prevents the surgeon from feeling discomfort and fatigue during surgery. This ergonomic position eliminates the surgeon's needs to twist and turn to simultaneously see the monitor and work with the instruments, as in traditional laparoscopic surgery. The *da Vinci* software system is designed in such a way that it compensates the surgeon's tremor on the tool tip location in the surgical site (end-effectors) [26].

Two main drawbacks of robotic surgery are lack of haptic feedback and critical mechanical failure. Robot system malfunctions have been reported (and well documented) in the literature for different laparoscopic procedures [27]. The lack of haptic feedback has remained unresolved for the *da Vinci* robotic system. It is

mainly related to the execution of complex tasks in which the surgeon needs to identify tissue consistency to discriminate between tumor and healthy tissue [28].

A common issue in both laparoscopic and robotic surgery is to decide about the optimal locations of the entry ports on the abdominal surface before surgery. In both traditional and robotic laparoscopic surgery, each of these entry ports must provide enough access to the operation area for the surgical tool inside the patient (the endoscope port must provide enough vision of the diseased region). In robotic surgery, the position of each of the entry ports relative to other ports is an important factor to prevent the surgical tools colliding inside and outside of the patient during operation.

2.1.3 Port Placement

In robotic procedures, preparation of the patient for the surgery is not as straightforward as for open surgery. The surgeon needs to determine the optimal locations of the entry ports on the patient's body before the operation; this process is called the planning phase of robotic surgery. The optimal port placement provides enough accessibility to the target organ (the surgical field) for the surgical instruments. It also provides sufficient vision of the surgical site for the endoscope during operation, as demonstrated in Figure 2.4.
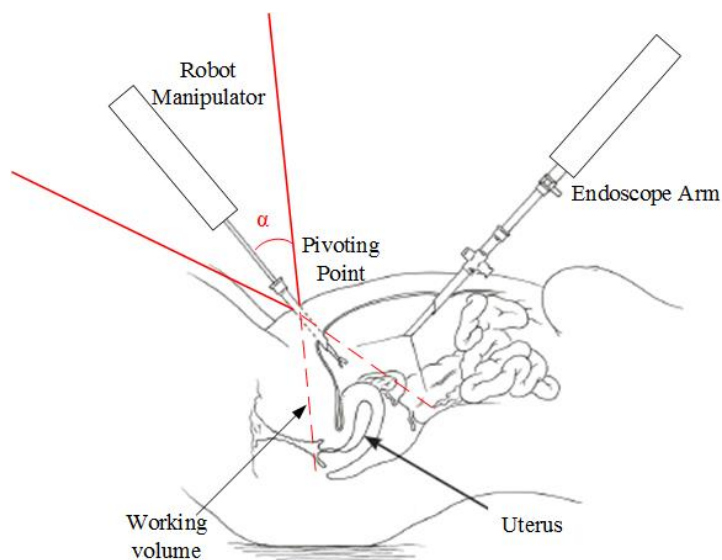
Figure 2.4 Working volume of a robot manipulator (surgical tool) and the endoscope in a hysterectomy procedure.

Each of the entry ports acts like a pivoting point on the abdominal surface. The surgical tools pivot about

11

the entry ports on the abdominal surface and create a conic working volume around the target organ. A sample of a working volume for the endoscope arm (the area between two dashed lines in red) in a hysterectomy procedure is shown in Figure 2.4.

The working volume of the surgical tools must include the whole area around the target organ. This means that the surgical instruments must reach all sides of the target organ during operation. However, the surgical tools' length and the robot manipulators' pivoting angle at the entry ports might restrict the working volumes inside the patient. Therefore, the patient's torso size, the target organ position inside the patient, and the robot arms' configuration and position relative to the patient (called the robot model) are the determinative factors for deciding about the optimal locations of the ports in the planning phase of a robotic surgery.

Poor decision-making (about the ports' locations) may lead to serious complications and injuries in MIS procedures [24]. Moreover, misplacing the ports may restrict the endoscopic view of the target organ (visibility of the target organ), and limit the surgical tools' access to the diseased area inside the patient (accessibility of the operation area) [29, 30]. Accurate port placement in the planning phase avoids the need for replacing the ports during the operation, which may cause extra post-operative injuries to the patient. Thus, optimal port placement prevents a long pre-operative procedure and decreases the surgeon's fatigue during the operation [9].

The position of the target organ (inside the patient) is primary knowledge that a surgeon needs to possess before planning the ports on the patient's body surface. In MIS, the surgeon usually estimates the surgical target position inside the patient and determines the ports' locations based on the patient's torso size and some external landmarks on the patient's body such as nipples, sternum, and umbilicus. For example, Cestari et al. identified three external landmarks for planning the ports in robotic radical prostatectomy (RALP) surgery: the upper margin of the pubic bone, the antero-superior iliac spines, and a point at the midline (the line that connects the pubic bone to the umbilicus) [31]. They used these landmarks (assisted by a nautical inclinometer) for finding the incisions' (ports') location on the patient's body in the Trendelenburg position. The efficiency of Cestari's port placement was validated by implementing the method on 30 patients who were divided randomly into two groups. The ports in the first group were planned according to Cestari's method; in the second group the ports were positioned based on the surgeon's experience. The results showed that less time was needed to place the ports in Cestari's method, and the ports' locations were correct for all the cases. However, lack of an imaging system (for determining the right position of the target organ inside the patient, patient model), and a computational tool for simulating the robot's arms movements (robot model), made Cestari's method unreliable and inaccurate in robotic surgery. Additionally, in Cestari's method the external landmarks do not necessarily corresponded to the individual patient's internal anatomy.

12

In addition to the target anatomy (size and position), the patient's body size and the operation settings (e.g. operating table position) are parameters that must be included in any port placement system in robotic surgery. Also, avoiding possible collisions between the robot manipulators is an additional constraint that needs to be considered [32].

Previous studies on port placement problems mostly proposed general guidelines and instructions that were only applicable in some MIS procedures. For example, Tabaie et al. used some external (natural) landmarks on a cadaver for estimating the location of the surgical sites (target organ) in coronary artery bypass surgery. They presented a simple patient model (2D body diagrams) to introduce the optimal locations of the ports, considering the target organ (IMA and LAD arteries) and the robot arm positions relative to the patient model (ZEUS robot arms that are attached to the patient table rails) [33].

Other studies proposed a solution to the port placement problem in robotic cardiac surgery [34]. They divided the port placement solution into four main phases as below:

- *Preliminary processing*: pre-operative medical images such as magnetic resonance imaging (MRI) or CT scans were used to construct a patient-specific 3D model (with the target organ embedded). Moreover, a simple robot model (a combination of cylinders and spheres) was made for evaluating possible collisions between the robot manipulators.

- *Planning*: using the patient and the robot models, the optimal positions of the ports were determined by an optimization process. The optimization process was a descriptive algorithm for choosing the points (on the patient models) that could maximize the target organ reachability and minimize the risk of a possible collision between the surgical tools inside the patient.

- *Validation*: the feasibility of surgery by using the planned ports (the ports that were obtained from the planning step) was validated by comparing the planned ports with the ones introduced by surgeons in the operating room.

- *Simulation*: A computer user interface was designed for presenting the suggested ports to the surgeons, so the surgeons could practice the interventions through different port placement strategies on the surface. They could judge the suggested ports by comparing them with their experience.

In another study, Chiu et al. used pre-operative CT scans to create a 3D patient model—called virtual cardiac surgical planning platform (VCSP)—for port placement in coronary artery bypass grafting (CABG) surgery [10]. Three virtual ports were positioned on the VCSP, two for manipulators and one for the endoscope. The user could change the virtual ports through a user-interface station. The shape and location of the targets (left coronary artery and the heart) were extracted from pre-operative CT images and placed in the VCSP platform. It allowed the users to visualize the tools and targets and determine the best locations of the ports appropriately. Using a thorax phantom, the accuracy of the port placement on the virtual model was verified by measuring the distances between the actual and virtual entry ports. The results showed that

13

the average distance between the virtual and actual port configurations was around 4mm. This means that the VCSP could be used as a 3D image-guided system for optimizing the port locations on the thorax surface. However, since VCSP was constructed on pre-operative medical images, it was not able to update positional changes of the target organ caused by insufflation.

The patient-specific model plays a significant role in introducing the optimal locations of the ports on the patient's body. However, there are some issues with using a pre-operative patient 3D model in a port placement system:

- In cardiac surgery, the external shape of the thoracic cavity does not change too much due to insufflation. However, in other types of laparoscopic procedures, the pre-operative patient model cannot be registered on the inflated abdomen in the operating room.

- The target organ's shape and location are not invariant under IAP. Therefore, the position and shape of the target organ in the pre-operative patient model are altered after insufflation.

In addition to the patient model, other studies proposed a method for modeling the robot manipulators' movements in robotic-assisted surgery [35]. The robotic arms' movements (during a robotic procedure) were recorded by tracing the positions of light indicators (LEDs) that were attached to each of the robot arms. Using the recorded movements (robot model), the possibility of robot arms colliding as an effect of changing the entry ports' position was investigated (collision detection system). The results showed that small variations in the parameters (ports' position) may have large effects on the robot's (ZEUS) movements: they can decrease the distances between the robot arms or equally increase the possibility of a clash between them.

In another study, Cannon et al. presented an optimization algorithm with two goals: maximum reachability of the target organ inside the patient, and minimum risk of the robot arms colliding during operation. They minimized the difference between the ideal position of the instrument tip (maximum reachability) and the actual position of the instrument that was achievable through the entry point on the surface [29].

Adhami and Coste-Marine proposed a descriptive optimization algorithm by using a patient model in minimally invasive coronary artery surgery. Considering the target location, they verified the suitability of all candidate locations (entry ports) on the surface of the patient model. "Tool tip distance to the target", "anatomical barriers between the port and destination", "visibility of the target" and "enough dexterity" were the goals of the port placement optimization problem [3].

Similar criteria for port placement optimization were implemented in later studies in which the patient's insufflated abdominal surface was simulated with a torso 3D model. The patient's abdominal surface was simulated with a simple torso model that was a combination of a hemisphere and a cylinder. The target

organ was put in a torso model, and the ports were placed on the surface to achieve the highest reachability of the target organ and minimize collision between the robot arms [5].

2.2 Research Objectives

The primary goal of this study is to come up with a decision-aid system to help surgeons to achieve accurate port placement in laparoscopic procedures. The decision-aid system determines the optimal locations of the ports in the operating room based on the patient's abdominal shape, the target organ position inside the patient, and the robot manipulators' position relative to the patient.

A simple workflow of the decision-aid system for finding the optimal ports' position is shown in Figure 2.5. The process begins with selecting four preliminary points (ports) on the patient's abdominal surface, three for the robot manipulators' entry ports and one for the endoscope arm. The next step is to verify the accessibility of the target organ by the surgical tools through the preliminary ports. Similarly, the selected port for the endoscope arm should provide a complete vision of the target organ area for the endoscope. Other criteria such as the manipulators' dexterity for manipulating the surgical tools through the selected ports on the patient's abdominal surface can be added to the evaluation system. Moreover, the three selected ports for the manipulators should minimize the collision between each pair of the manipulators inside the patient (common area between the two manipulators' working volumes in Figure 2.4).
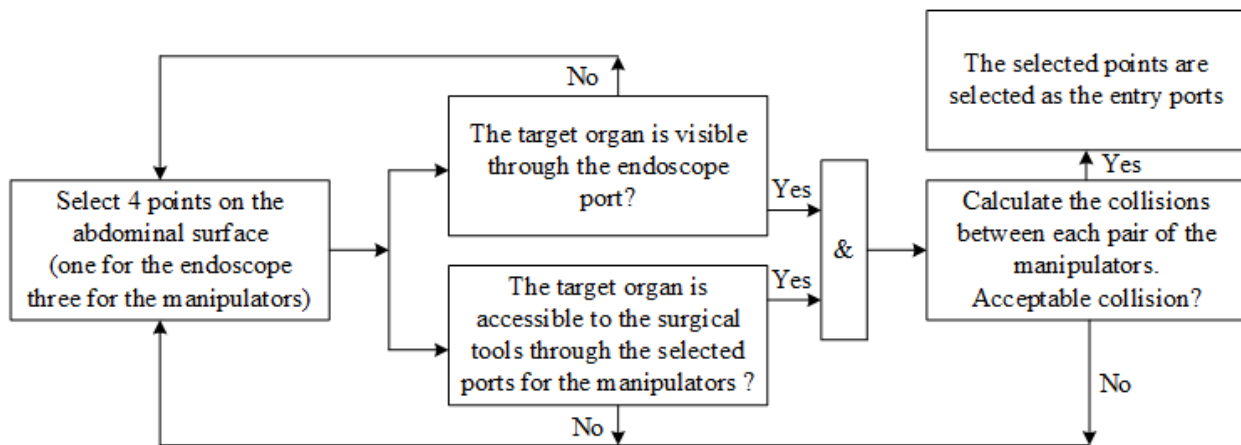
Figure 2.5 Working flow for selecting the ports in a laparoscopic procedure

To summarize the workflow in Figure 2.5 we used three different criteria for checking the goodness/suitability of the points to be selected as the entry ports: the target organ accessibility, the visibility of the target organ, and the collision between the surgical tools inside the patient. However, we need to quantify these criteria in mathematical terms to find the optimal position of the ports on the patient's

abdominal surface. The mathematical representation of the patient's abdominal surface is a virtual 3D model of the inflated abdomen in the operating room, called the patient-specific model. The coordinates of the points on the patient's abdominal surface can be found from the patient-specific model.

The robot is mathematically represented by a kinematic model in which the possible position and configuration of the manipulators—for bringing the manipulator endpoint (end-effector) to a certain position on the abdominal surface—is represented by the links and the joints angles.

Figure 2.6 presents a schematic of our comprehensive decision-aid system in the port placement problem. The system has three main components: the robot model, the patient model and the decision-making unit. The patient model must contain the target organ and the external shape of the abdominal surface after insufflation. The patient model can be made directly from the medical images that are captured from the abdominal cavity under IAP. However, the operating room is usually too small to use medical imaging scanners (such as computed tomography (CT) or magnetic resonance imaging (MRI)) and the robotic system simultaneously. Instead, in this dissertation we use a range imaging camera (e.g. Kinect V2, Microsoft [36]) to image the external shape of the patient's abdomen after insufflation. The captured image from the abdominal surface is a cloud of 3D points that is given to a surface reconstruction algorithm (alpha shape method) to generate a 3D mesh of the inflated abdomen, called the external model. The external model is not a complete patient model since it does not contain the target organ. Therefore, the next step of creating a patient model is to place the target organ inside the external model.
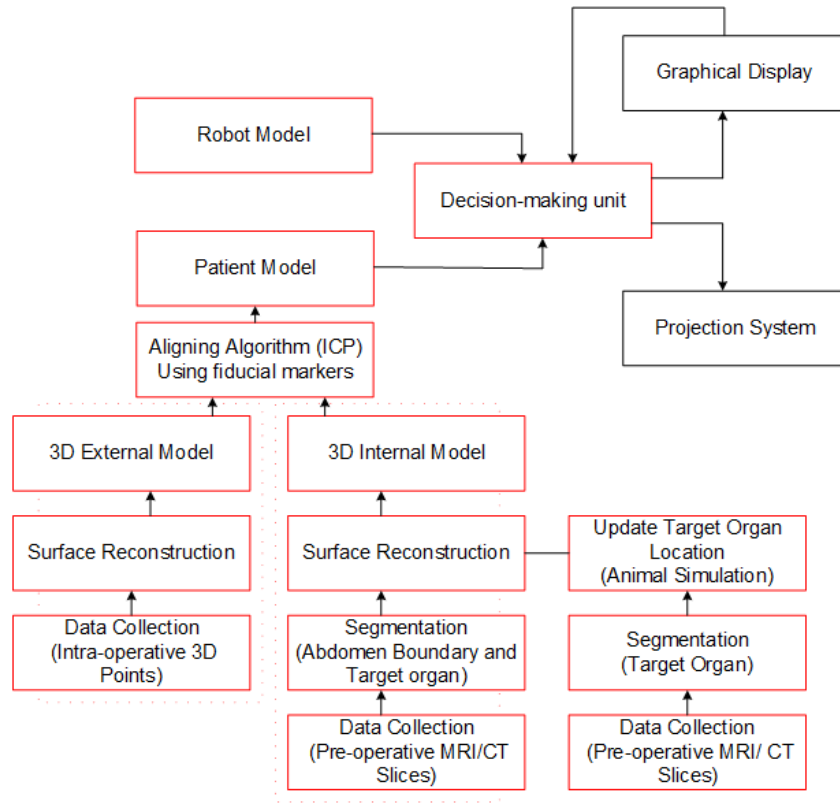
Figure 2.6 The proposed plan for planning ports in a laparoscopic surgery

We use pre-operative medical CT scans for finding the target organ's shape and position in the patient's body. The idea is to create another 3D model of the patient before the operation which includes the target organ, called the internal model. The internal model is aligned with the external model to place the target organ within the external model, and the result of the alignment is the patient-specific model. However, the original position of the target organ in the internal model is altered due to insufflation and, consequently, needs to be updated in the patient model under IAP.

To update the position of the target organ inside the patient model, we need to measure the shift of the target organs under IAP conditions in laparoscopic procedures. We used four pigs under same conditions to measure the organs' displacement due to insufflation. The estimated shift of the organs in the pigs' bodies is considered for similar organs in the human body, so we can correct the position of the target organ in the human's body due to insufflation. In this dissertation, we focused on the hysterectomy procedure, in which the uterus is the target organ.

The next component of the decision-aid system is the robot model. The *da Vinci SI* (*Intuitive*) robot consists of three manipulators and one endoscope arm (Figure 2.2). From the robot model, we can determine the position of the manipulators' end-effectors relative to the patient's position in the operating room. In fact, having the patient and the robot models in the decision-aid system, the manipulators' end-effectors'

position relative to the patient's body, and the coordinates of the points on the patient's body are the known parameters in the decision-making unit in Figure 2.6. The decision-making unit is responsible for performing two major tasks: first checking the accessibility of the points on the patient's model (respect to the target organ position) to each of the robot arms and selecting and marking the accessible areas on the patient model. After finding the accessible areas for the manipulators, the second task of the decision-making unit is to use an optimization algorithm to minimize the collision risk between each pair of the manipulators inside the patient model. The output of the optimization algorithm is the optimal locations of the ports on the patient model that can be either projected on the patient's abdominal surface or displayed on a monitor in the operating room.

The second goal of this dissertation is to reduce the pre-operative planning and set-up time in our port placement solution. We can eliminate the need for making the internal model if we have enough knowledge about the target organ's shape and position. We constructed the patient models for seven patients (who underwent a hysterectomy procedure) to estimate the position and the volume of the operation area inside the patient. As a result, having only the external model, we will able to predict the target organ position inside the patient after insufflation without constructing the internal model.

The final goal of the project is to validate our port placement system by verifying its performance in determining the optimal locations of the ports on the patients' abdominal surface. We use a body phantom (including a target organ) with known optimal locations of the ports that were obtained from previous surgical procedures. We use our port placement system to determine the optimal locations of the ports on the phantom surface and compare them with the actual ports' location from the surgical procedures.

2.3   Chapter Summary

In this chapter, we reviewed several background items that provide context for the port placement problem in the dissertation. This includes a short description about MIS procedures and the port placement difficulties in robotic surgery. We also briefly described the goals of our research in the dissertation, which include a comprehensive solution to the port placement problem in the hysterectomy procedure. Finally, we introduced the main components of our port placement system (the patient model, the robot model, and the decision-making unit) that are discussed with more details in subsequent chapters.

Chapter 3

General Approach (Methodology)

In this chapter we will introduce our methodology to solve the port placement problem in hysterectomy procedures. This methodology is applicable to other laparoscopic procedures in the abdominal or pelvic areas (such as prostatectomy). Based on the project workflow in Figure 2.6, our design of the port placement system includes three main components: a patient-specific model, a kinematic model of the robot manipulators (*da Vinci SI*), and an optimization algorithm.

The patient model is a 3D mesh that is constructed from 3D images of the patient's abdominal surface—a range imaging camera (3D scanner) is used for imaging the inflated abdominal surface in the operating room. This patient model, called the external 3D model, does not include the target organ and the diseased areas inside the patient. Thus, we first need to make a 3D shape of the target organ, and then put it inside the external model. We will use image processing segmentation techniques to extract the shape of the target organ and the patient's body shape from pre-operative 2D medical images. Using the segmented images and a surface reconstruction algorithm (alpha shape), another 3D model of the patient is constructed that contains the target organ, called the internal model.

The target organ is placed inside the external model by superimposing the external model on the internal model. However, these two models are not aligned well, because the external model is constructed after insufflation, whereas the internal model is built from the patient's abdominal surface prior to insufflation. We will find a transformation matrix for aligning the internal and the external models, using four points on the patient's body that are assumed to be fixed during insufflation.

The result of the alignment is the patient-specific model that contains the target organ. The abdominal surface in the patient model represents the patient's abdomen after insufflation, however, the target organ's position is changed in the patient model under IAP. To update the target organ's position in the patient model, we will measure the shift of abdominal organs in the animals' body due to insufflation (see subsection 3.4). The measured shift of the abdominal organs in the animals' body is used for estimating the shift of similar organs in the human body (patient model) under IAP.

After completing the patient model (the 3D model of the inflated abdomen with the updated location of the target organ), we simulated the robot arms docking on the patient. The robot arms' configuration, and the positions of the arms' end-points relative to the patient's body (patient model), are demonstrated by a robot model (see subsection 3.2).

Using the generated patient model and the robot model, we will introduce an optimization algorithm (section 3.4) for finding the optimal locations of the entry ports on the patient's abdomen (patient model). This optimization algorithm minimizes possible collisions between the manipulators, and maximizes an efficiency index that is defined as the ratio of the volume of the manipulation and the volume of the endoscope view.

3.1 Patient-Specific Model

The patient-specific model is a 3D mesh representation of the patient's abdominal surface in the operating room. There are two ways to create a patient-specific model after insufflation: the intra-operative method and the combined technique. The idea in the intra-operative method is to scan the patient's abdominal cavity after insufflation in the operating room. The captured 2D scans of the patient's body are used to generate two 3D meshes of the patient's abdomen and the target organ (see section 3.1.2 for more details). The main drawback of this method (in robotic surgery) is the scanning difficulties in the operating room. The operating room is usually too limited a space to use MRI/CT scanners and the robot simultaneously. MR scanners are too bulky to be used during robotic surgery, so the patient needs to be moved for the image acquisition. Also, using advanced portable CT scanners (e.g. mobile C-arm) is an expensive and complex procedure for making a patient 3D model in the operating room [37, 38].

In the combined method, we create two different 3D models of the patient's abdominal cavity before and after insufflation. These two models are called internal and external model respectively. The work flow for constructing the internal and the external models is illustrated in Figure 3.1.

Unlike the patient's intra-operative model, the internal model is constructed from pre-operative medical images, and it contains the target organ which is extracted (segmented) from the images and placed in the internal model. However, the abdominal surface and the target organ's shape and location are changed

after insufflation. This means that the outer shape of the abdomen and the target organ's position in the internal model need to be updated after insufflation. To update the outer shape of the abdomen after insufflation, we image the abdominal surface in the operating room by using a 3D scanner or a range imaging camera in the operating room. The 3D scanner generates a depth (3D) image of the patient's abdomen after insufflation, called the external model—we used the Kinect V2 camera (Microsoft [36]) for imaging the patient's body in the operating room as shown in Figure 3.2.
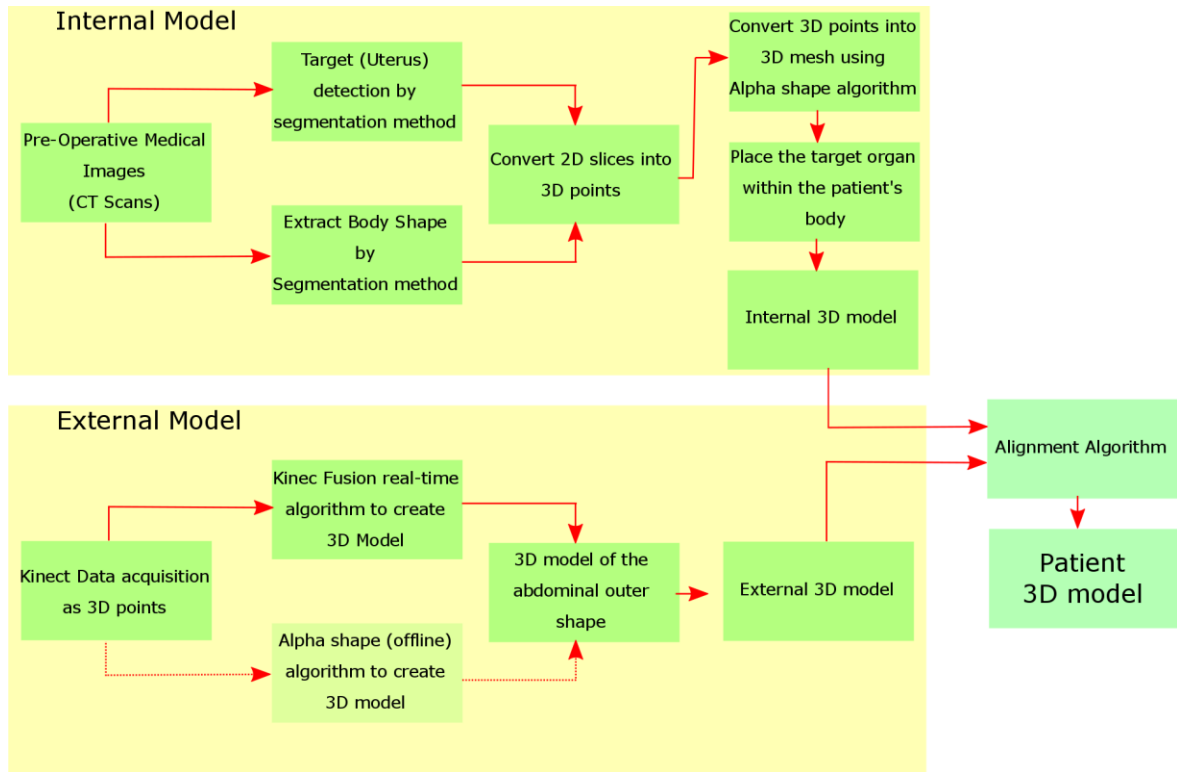
Figure 3.1 Workflow to construct the patient-specific model in "combined" method
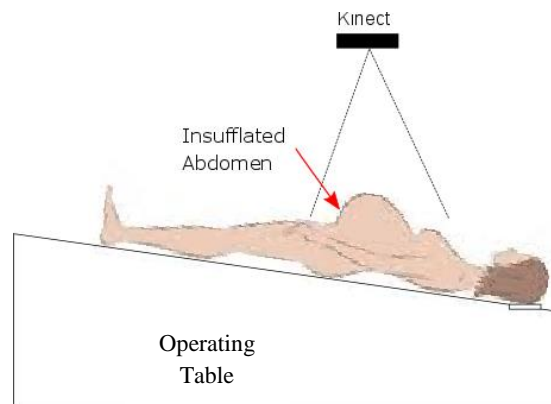
Figure 3.2 Experimental set-up to capture 3D points from the abdominal surface in the operating room

The generated external model is superimposed on the internal model to create a patient-specific model. In fact, the patient-specific model is the internal model with the updated abdominal surface after insufflation. We use animal bodies (sows) for measuring the abdominal organs' motion under IAP. The results of the animal study are used to estimate and update the target organ's location in the patient-specific model. In the following subsections, we will discuss more details about constructing the patient-specific model (the internal and the external models, and an alignment technique) in hysterectomy procedures. The target organ in hysterectomy procedures is part of the reproductive system, including the uterus and ovaries.

3.1.1   External 3D Model

In laparoscopic surgery, CO_2 pressure (in insufflation) acts on the internal surface of the patient's abdomen and the abdominal outer shape is expanded and warped after insufflation. Researchers used different methods to track and monitor the deformation of the abdominal wall. For example, Song et al. measured mechanical properties of the inflated abdominal wall (such as abdominal wall curvature) in gastrointestinal laparoscopic surgery [39]. An infrared motion analysis system—consisting of twelve markers on the abdomen surface and three infrared cameras—was used to track abdominal wall alterations during insufflation. It showed that the curvature (radius) of the abdominal wall in the sagittal plane changed more than the transverse plane [40].

In another study, researchers proposed an algorithm to estimate the morphological changes of the abdomen after insufflation [41]. Two pigs (abdomen) were imaged by a CT scanner to create initial volumetric meshes (3D models) before insufflation. The insufflation process was simulated by applying gas pressure (around 12-15 mmHg) on the initial meshes, and the final shape of the abdomen (after insufflation) was calculated by using a finite element analysis. The imposed pressure on the internal abdominal surface was assumed to be distributed equally over the initial mesh's vertices. A comparison between the simulated abdomen (3D model) and the actual inflated abdomen (constructed from CT images after insufflation) showed that the Euclidean distances between the two closest vertices (not corresponding) on the two models was between 0.5 cm to 2 cm. However, the difference between the actual and simulated abdomen (after insufflation) was highly dependent on the mechanical input parameters (Young's modulus and Poisson ratio) in the simulated abdomen.

To avoid the arbitrary input of mechanical parameters in the finite element analysis and the complexity of the infrared system, we used a range imaging camera for imaging the abdominal surface during insufflation (Figure 3.2). The resulting images, the range images, have pixel values that correspond to the distance to the camera. Thus, the pixels of a range image can be represented by 3D points in a 3D coordinate

system that is attached to the camera. The generated 3D points from an object in front of the camera are given to a surface construction algorithm to create a 3D mesh of the object. In this dissertation we used Kinect V2 to create a 3D mesh of the patient's inflated abdominal surface, called the external model. In the following subsection we will discuss more details about the Kinect technology and the surface reconstruction techniques for creating an external model of the patient in the operating room.

3.1.1.1   3D Scanners: Kinect

Three-dimensional (3D) scanners reproduce the dimensions and positions of objects in the form of digital 3D points on the computer screen. Time-of-Flight, Laser Scanning, Laser Speckle Pattern Sectioning, and Structured Light are some of the dominant and highly accurate techniques to obtain 3D information in a variety of 3D reconstruction applications [42]. However, most 3D scanners may not be appropriate for use in a sterile clinical environment. The complexity of use, long scanning times, and high costs (for some scanners as much as \$10,000–\$60,000) are some of the limitations of using advanced 3D scanners in clinical applications [43].
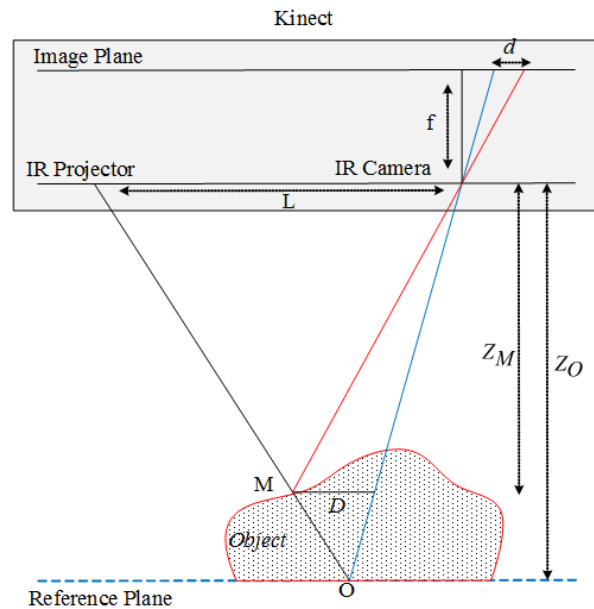
Figure 3.3: Schematic representation of Kinect depth-disparity relation

Microsoft's Kinect device was first released in 2010 as part of a natural interaction system in the Xbox 360 game package. Researchers now use it in different areas such as health, biomedical engineering, and 3D printing. The next generation, Kinect V2, retains all the features of the previous device as well as features marked improvements in audio, RGB, and infrared cameras (Microsoft Kinect V2) [36]. Among other useful features, the ability to acquire in-depth information makes Kinect an attractive tool for 3D

modeling and scientific visualization. In comparison to other 3D scanners, the Kinect structure is straightforward and easy-to-use for most of the applications. The old version of the Kinect device exploits a light structure technique for depth measurements. It consists of an infrared projector, an infrared camera, and an RGB camera. The infrared projector projects a pattern of structured light (speckles) on objects in its field of view. The RGB camera records a color image, and the infrared camera captures the infrared light reflections (infrared image) from a scene as shown in Figure 3.3.

The captured infrared image is correlated against a reference plane image that is stored in the memory of the Kinect device. The reference plane distance to the infrared camera is known and used to measure the shifts of a speckle's image due to the presence of an object in a scene. For example, reflected light from "O", on the reference plane in Figure 3.3, is distorted by "M" on the object surface. As a result, the pre-set image of "O" is shifted by "d" in the image plane which is called disparity of the speckle "O". Having a disparity image and using a simple triangulation [44], the depth of "M", on the object surface can be calculated from following equations:

$$\frac{d}{D} = \frac{f}{Z_M} \tag{3.1}$$

$$\frac{D}{L} = \frac{Z_o - Z_M}{Z_o} \tag{3.2}$$

$$Z_m = \frac{Z_o}{1 + \frac{Z_o}{Lf}d} \tag{3.3}$$

in which Z_O is the distance of reference plane to the Kinect camera, "L" is the distance between the infrared camera and the infrared projector, "f" is the focal length of the infrared camera, and Z_M indicates the measured depth of the point "M" on the object.

According to the manufacturer (Microsoft), Kinect V2 has same components of RGB and infrared cameras and an infrared projector. However, the depth-measuring method has been changed to indirect Time-of-flight instead of structure light that was used in the old version of the Kinect. In the indirect method of Time-of-flight, the phase shift between emitted and reflected lights in Figure 3.3 is calculated in Kinect's sensor, and the depths are estimated with the following equation [45]:

$$Z_m = \frac{\Delta \varphi}{4\pi f} . c \tag{3.4}$$

in which $\Delta \varphi$ is the phase shift, and "f" and "c" are the frequency and speed of infrared light respectively.

Kinect's accuracy for estimating the objects' distance to the camera (depth information) has been investigated in several studies [46]. For example, Khoshelham et al. showed that the Kinect error in measuring depth is between a few millimeters and 4 cm. They also demonstrated that the error in depth measurement increases with increased distance between the object and the Kinect sensor (camera) [47]. Other studies reported depth accuracy in the most recent version of the Kinect (Kinect V2) by placing some points on an experimental planar surface in front of the camera. They showed that to reduce the error of depth measurement the object should be placed within the range of 0.5-3 meters from the Kinect device [48].

Similar to other 3D scanners, Kinect depth images are a cloud of three-dimensional points from the real-world objects in front of the camera, so the accuracy of Kinect in measuring 3D coordinates of the points needs to be validated under practical conditions. For example, Henseler et al. verified the Kinect accuracy for measuring breast size in cosmetic surgery. They created a 3D shape of the breast from a set of 3D points captured by the Kinect camera. The volume of the breast was calculated and compared with the manual measurements. The mean difference between the calculated volume (by Kinect) and the manual measured volume was about 10% [49]. In another study, researchers evaluated Kinect accuracy for measuring the distances between some natural landmarks on the patients' bodies in cosmetic surgery. The results showed that there were small differences between manual and Kinect measurements (1.9~2.0 mm) [50].
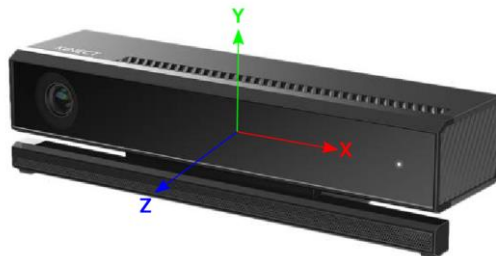
Figure 3.4 Kinect coordinate system (attached to the camera)

Considering Kinect accuracy in depth measurements, the shape of any object in front of the camera (Kinect) is estimated in the Kinect microprocessor. Every point on the object (e.g. the patient's abdomen in Figure 3.2) is represented in a three-dimensional coordinate system that is attached to the Kinect as shown in Figure 3.4.
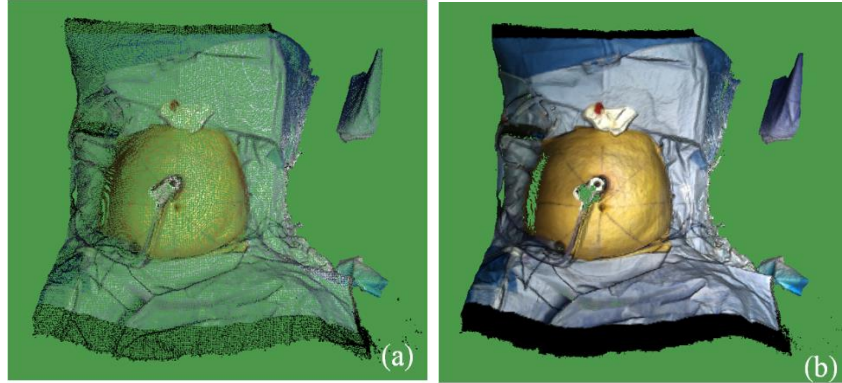
Figure 3.5 (a) A sample of 3D colored points, captured by Kinect in the operating room.
(b) A sample of generated 3D mesh by Kinect fusion (from a patient's abdominal surface)

"The Kinect for Windows SDK" provides tools and APIs for developing Kinect-based applications in different operating systems (e.g. Widows) [36]. Kinect fusion is one of the real-time SDK toolkit techniques for creating a mesh from the 3D points captured by Kinect. The Kinect fusion technique uses consecutive 3D images (frames) of an object from different perspectives and fuses them into a single representation [51], so when a Kinect camera is mounted in a fixed position (Figure 3.2), consecutive depth frames are only captured from one point of view, and the fusion forms a single 3D mesh as shown in Figure 3.5. The primary shape of the object in the Kinect fusion method is assumed to be a cube that is made up of a certain number of voxels. Regarding the acquired depth information (z axis in Figure 3.4), and x-y position of the voxels, some of the voxels are kept or removed from the cubic volume to generate the final shape of the object (e.g. the patient body in Figure 3.5).
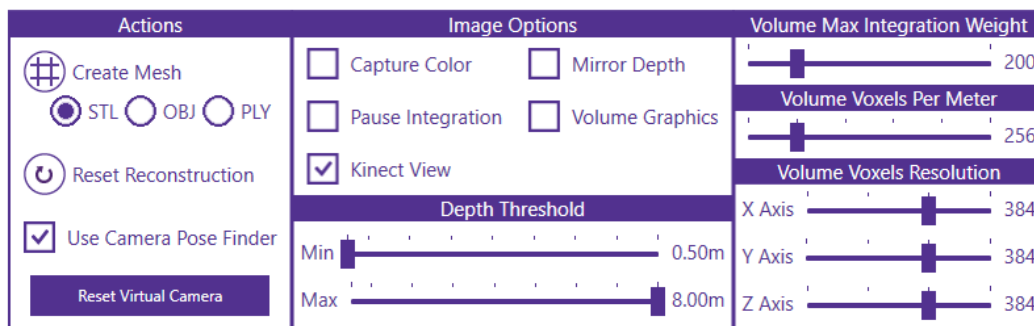
Figure 3.6 Kinect fusion user interface

The Kinect fusion user interface for constructing a 3D mesh (volume) from the objects in front of the Kinect camera (e.g. the patient's abdomen) is shown in Figure 3.6. The number of voxels to create an image of the patient's body depends on the amount of memory in the reconstruction device (e.g. a laptop used for

26

data collection in the operating room). Typically, the number of voxels can be up to 640x640x640 = 262144000 voxels; that is determined in the "Volume Voxel Resolution" part of the Kinect fusion (KF) user interface in Figure 3.6.

The "Voxels Per Meter" member of the KF user interface scales the size that one voxel represents in the real world. For example, if we want this value to be 128 vpm (voxel/meter), and the voxel resolution is set to $384\times384\times384$, then the volume represents a cube with 384/128=3m length in the real world. In fact, the combination of voxel resolution (in x,y, and z axis) and the number of voxels per meter enables us to specify a cubic volume with different sizes and resolutions. To achieve more accuracy in constructing the patient model, we chose the resolution as $384\times384\times384$, and the "Voxels per Meter" was selected as 256 vpm.
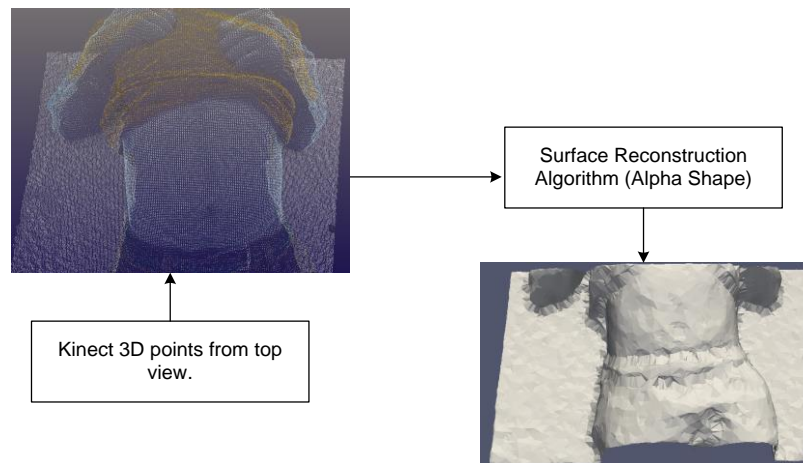
Figure 3.7 A sample set of 3D points and the generated 3D mesh by alpha shape algorithm (external 3D model)

The created mesh can be stored in different 3D formats such as "PLY", "OBJ", and "STL". In this dissertation, we used the PLY file format to represent the 3D objects (the patients' bodies) [52].

Instead of using the real-time KF, the 3D points of the patient's body can be given to another surface reconstruction algorithm such as the alpha shape method to reconstruct the patient's body mesh in the computer [53]. We will discuss the alpha shape method in more detail in section 3.1.2.3. A sample set of 3D points and the resulted mesh, generated by an alpha shape algorithm, is shown in Figure 3.7.

The accuracy of the external 3D model (dimensions and surface detail) depends on the type of 3D scanners and the surface reconstruction algorithm. The Kinect camera is a simple device for imaging the patients in the operating room. It can be easily mounted above the patient and be fixed during insufflation. However, for more accurate 3D external shape of the patients' abdominal surface, other advanced 3D scanners can alternatively be used in the operating room [54].

3.1.2 Internal 3D Model

Based on the workflow in Figure 3.1, the next step of creating a real-time patient-specific model is to construct the internal 3D model. A typical algorithm to construct a 3D internal model is illustrated in Figure 3.8. A series of 2D images (pre-operative scans), acquired from computed tomography (CT) or magnetic resonance imaging (MRI), are converted into a cloud of 3D points. A segmentation process (manual or semi-automatic) is required to extract the boundaries of the abdomen shape (points in white) and the target organ shape (points in yellow) in Figure 3.8 (see section 3.1.2.2 to find more details about different segmentation techniques).

The physical distance between adjacent pixels (in the 2D images), and the distance between consequent slices are used to convert 2D images into a set of 3D points. The resulting 3D points are given to a surface reconstruction algorithm to generate 3D meshes (models) of the patient's body and the target organ as illustrated in Figure 3.8. We used the alpha shape method to reconstruct the patient's abdominal surface in the internal model (see section 3.1.2.3). The target organ's position in the internal model needs to be updated due to insufflation. In section 3.4 we will present the animal study results that give us an estimate of the abdominal organs' motion under IAP.
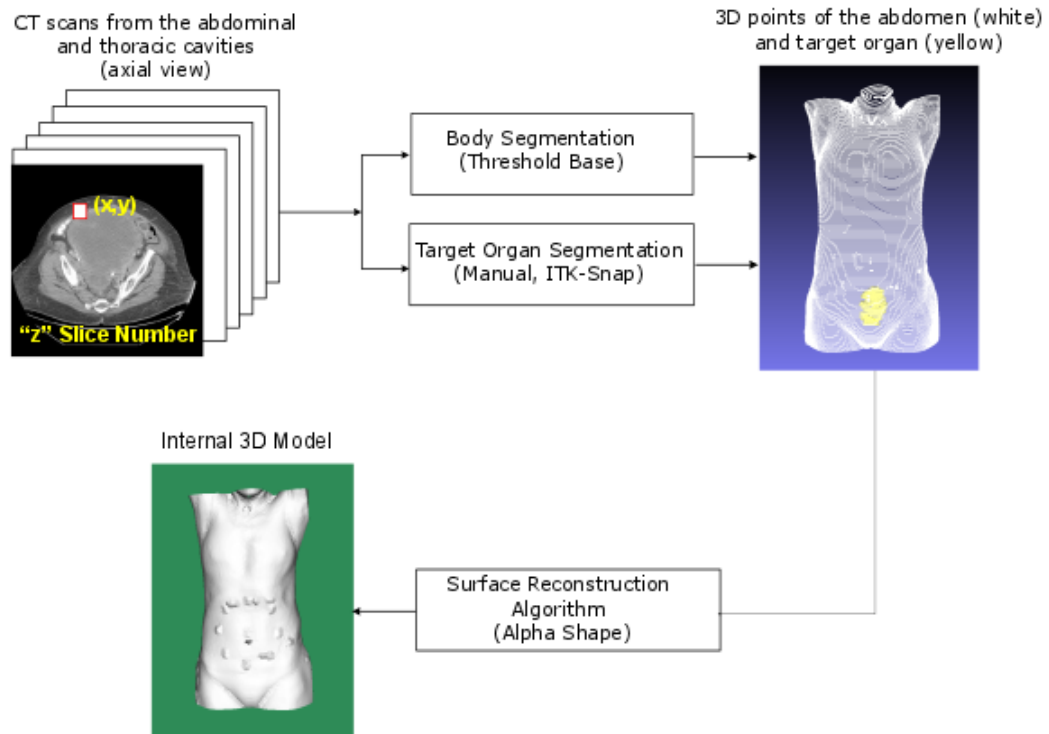
Figure 3.8 Algorithm to construct a 3D internal model

The algorithm steps (in Figure 3.8) were written in ITK-VTK pipeline [55, 56]. ITK is an open-source software for image processing (such as segmentation and registration), and VTK is a visualization toolkit to form and render 3D shapes in the field of computer graphics. A brief description about ITK and VTK pipeline and the relevant libraries used to construct the internal 3D model algorithm will be presented in subsection 3.1.2.4. Moreover, we will briefly discuss medical image structure, and the image processing segmentation methods in section 3.1.2.1 and 3.1.2.2 respectively. The alpha shape algorithm for surface reconstruction will be detailed in subsection 3.1.2.3.

3.1.2.1   MRI, CT scan data structure

Computed tomography (CT) is a medical imaging technique that uses special X-ray equipment to create detailed pictures (or scans) of the areas inside the body. The quality of CT images to make a 3D model is estimated by several parameters, whereby image contrast, noise, resolution and artifacts are the most common influences.

The highest CT possess image quality occurs under ideal conditions, where the radiation dose is very high, X-rays only consist of a single wavelength, and the detectors have the highest resolution. Moreover, no scattering or motion occurs during scan. However, in the real world, there are always clinical constraints on the radiation dose for the patient's safety. Moreover, an ideal X-ray source (to generate a pure single wavelength) and ideal detectors are never found. Hence, the existence of artifacts and noise is inevitable in a real-world imaging system.

Motion artifacts and noise are the most common factors that may negatively affect the quality of CT images:

Noise:

The random noise in CT images is the statistical noise that arises from the error/fluctuation of counting the number of photons hitting the detector. This statistical noise appears as thin streaks on the images. It usually obscures low-contrast regions of an image, especially soft tissue. To reduce the destructive effects of statistical noise in CT images, the number of photons (dose) to the detectors must be increased. This may drastically damage the patients' healthy tissue. However, new advances in CT protocols (iterative reconstruction techniques) provide a balance between image quality (noise) and the dose to the patients [57]. Besides, image processing techniques such as image enhancement can reduce the effects of statistical noise on most CT images.

Motion Artifact:

The sources of these artifacts are the patients' respiratory and cardiac motions that are inevitable during abdominal CT scanning and may cause the images to be blurred and doubled. A sample of a CT image degraded by respiratory motion artifacts (caused by patient's breathing during the scan) is shown in Figure 3.9.
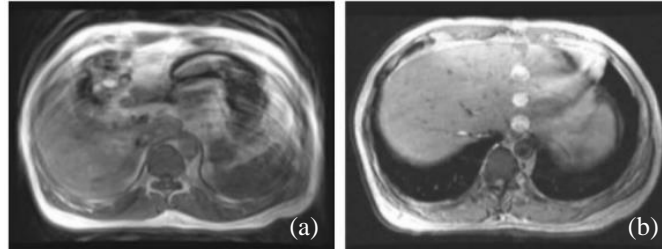
Figure 3.9 (a) Abdominal CT image without holding breath (resulting in respiratory motion artifact, double image) (b) Abdominal image holding breath (no respiratory motion artifact)

To avoid motion artifacts in CT images, the patient's scanning must be faster. This reduces the scanning time, and consequently the patient has less time to move during the image acquisition. Nowadays, new generations of CT machines are equipped with either gantry rotation or more X-ray sources to accomplish faster scanning time [58].

3.1.2.2   Segmentation Methods

The goal of the segmentation process in the internal 3D model algorithm (Figure 3.8) is to extract the boundaries of the abdomen and the target organ from the CT images simultaneously. Based on the patient-specific workflow (Figure 3.1), constructing the internal model is a pre-operative process. Therefore, the whole segmentation procedure (separating the patient's abdomen and target organ from CT slices) can be performed manually before the operation. However, when the number of CT slices is too large, manual segmentation can be a time-consuming and exhausting procedure. For instance, the boundaries of the patient's body (shown in Figure 8.3) must be separated from 100~300 CT. Thus, the segmentation process is easier to perform with automatic techniques rather than manual segmentation.

We used ITK (section 3.1.2.4) and ITK-SNAP segmentation tools for creating the 3D shape of the target organ from CT slices. ITK-SNAP is an open-source software for segmenting different tissues in medical images. It provides manual and automatic segmentation for extracting the regions of interest (such as soft tissue) in an image as colored contours [59]. The validity of ITK-SNAP for medical image segmentation was investigated in several studies [60].

The automatic segmentation speeds up the process of extracting the boundaries of the target organ

within the abdominal cavity, especially when the CT or MRI slices are low-contrast images and the edges (and borders) are not visibly detectable. There are various well-known methods in image processing that have been used for soft tissue segmentation in medical applications, whereby thresholding, edge-based and region-based are the most commonly used techniques for visceral organ segmentation [61]. Below we briefly explain these segmentation techniques and the use of thresholding and region growing methods in our project:

Thresholding

Thresholding is the simplest way of separating different regions in an image. In the thresholding method the input image is converted into a binary image based on the intensity value of the pixels, a lower and an upper threshold that are defined by the user. The upper and lower threshold values are usually chosen by using the image histogram. The pixels with an intensity level between the lower and upper limits are set to one, and the remaining pixels' values are converted to zero. The result is a binary image that is called the binary filter. Multiplying the binary filter by the input image, the desired region is separated from the other parts of the entry image. The main problem in using the thresholding method is that the lower and upper thresholds are not always easy to find, especially for blurry or low-contrast input images. Besides, adjacent organs' pixels in most medical images are in same range of intensity, and distinguishing between the adjacent organs is not practically possible with the threshold method.

Region growing

This is another method of segmentation, based on grouping the pixels in an image in a particular region of interest. A set of starting pixels is selected inside the region of interest, called seeds. The adjacent pixels are then appended to the seeds if they fall into the same category of similarity (feature). Texture, color, and intensities are the features that are usually used as criteria for grouping similar pixels in the area of an image [62]. The initial search for the seeds, long computation time and high noise sensitivity are the main disadvantages of the region growing technique.

Merging and splitting

The merging and splitting method is another segmentation technique that can be used for detecting the boundaries of the target organ in the patient's CT images. Similar to the region growing method, the pixels are categorized based on their common features such as text, color and intensity. Two basic operations of merging and splitting are performed on an input image to find the regions that are separated by boundaries. Unlike the region growing algorithm, splitting operators take the whole image as a single, big area and

subdivide it into smaller regions while the condition of homogeneity (being in the same category of color, intensity, etc.) is not satisfied.

The convergence of the merging-splitting algorithms is usually satisfied with one of the typical criteria such as:

- The variance of intensity levels of the segments is lower than a threshold value.
- The variance of texture/color measures in the segmented areas is lower than a threshold value.
- The entropy of the segments is lower than a threshold.

Edge-based method

In an edge-based algorithm, the regions of interest are extracted from an image by using various edge detection techniques. These methods scan the image for discontinuities to identify the objects' boundaries. Most of these techniques are available in VTK and ITK software (as edge detection filters). The most well-known edge detection filters are gradient, LoG, Laplacian, Sobel and Canny edge detection. In this dissertation, we used canny edge detection to extract the boundaries of the abdomen. The step by step procedure for the segmentation process with Canny edge detection can be summarized as follows [63]:

- Applying a smoothing filter such as a Gaussian filter to reduce the noise effects on the input image.
- Calculating gradient strength and direction for the pixels using gradient filters.
- "Non-maximum suppression" which removes the pixels that are not part of the edges.
- Double thresholding and hysteresis, which discerns between the edges created by noise and the actual edges. As a result, only the stronger edges are preserved in the image.

The segmentation algorithm should work for both 2D and 3D input images. If the input of the algorithm is a series of 2D images, the segmentation filter operates on each slice of the database separately. Then the processed 2D slices are converted to 3D points by the procedure explained in section 3.2.

3D segmentation is another method in which a 3D image is directly fed to the algorithm. Pixels are replaced with the voxels in the 3D image, and the same segmentation techniques as for 2D images are applicable. For example, in the region growing algorithm, the number of the adjacent pixels for a pixel in a 2D image is nine, whereas the number of neighbor voxels for a voxel in a 3D image is twenty-one. This increases the process time of the region growing algorithm in 3D images, because the algorithm needs to check twenty-one neighbors for each voxel. As a result, 2D image segmentation is more precise and faster than 3D image segmentation. Figure 3.2 shows the 3D shape of the target organ (uterus) that was made from segmented 2D CT slices.

3.1.2.3   Surface Reconstruction Algorithm (Alpha Shape)

There is a variety of methods available in the field of graphical representation and data visualization to construct a surface from a set of given unorganized 3D points. Most of the existing algorithms have been used for surface reconstruction of an object in the real world. The data in these methods are usually acquired from 3D scanners, cameras, or mathematical models [64]. The most commonly used surface reconstruction algorithms are based on the interpolation (B-Spline) method [65], the least-square method [66], Poisson surface reconstruction [67], and Voronoi/Delaunay triangulation [68]. The implementation technique is selected based on its strength in dealing with specific features of the object being reconstructed. Traditionally, the B-Spline method is used for curve fitting over a set of points in two and three dimensions. A spline is a piecewise polynomial function that covers all the space to form a curve/surface in two or three dimensions [69]. Least square is another fitting method in which the errors are calculated based on the differences between points on the reconstructed surface and the given data. The obtained errors are iteratively minimized to achieve the most similarity between the real object and the constructed model [70]. The Poisson method is a technique used for reconstructing surfaces based on 3D data points. In this method, a set of oriented 3D points, V, are used to find a gradient surface. The oriented points are supposed to be fitted on the gradient surface χ which is obtained by solving the Poisson equation: $\nabla.\nabla\chi=\nabla.V$. The Poisson algorithm uses all the given points at the same time to generate a surface, hence it is known as a global solution for surface reconstruction problems. Poisson surface reconstruction produces a smooth surface over the given points. It usually fills all the holes (low density areas) in the dataset. In the case of given 3D points on the abdominal surface, the created Poisson surfaces include all the points. This results in a larger surface than expected, for example the background areas (operating table) are also smoothly connected to the created surface. Therefore, the abdomen's edges (connection lines between the abdomen and the operating table) in the Poisson method are not sharp and not suitable for our purposes.

The Delaunay triangulation (DT) method has been shown to be efficient and accurate for dense and noise-free data [68]. It generates a mesh of triangles that can cover most of the points. DT algorithms check for the possibility of the nearest points' triangulation: a circle (sphere if in 3D) crossing any three points in the data must not include any other point in the enclosed space. Figure 3.10 shows the accepted and rejected triangulation for four sample points {A, B, C, and D}.

A drawback with the Delaunay triangulation method is that it does not have any control over the size of the triangles. It produces larger triangles in sparsely populated regions in which points are far from one another, and smaller triangles in dense regions in which points are very close to one another. Hence it takes all unwanted points into account for surface reconstruction. This could cause the reconstructed surface to resemble a large convex hull with a larger measured area than the actual object.

Alpha shape algorithm is a method derived from DT methods [68]. The major difference between DT and the alpha shape algorithm is the additional constraint in the latter method—the radius of each circle passing through the three vertices of the triangles must be less than a predefined value, alpha (α), as shown in Figure 3.10. The alpha value ranges from zero to infinity, and the alpha algorithm generates different shapes, called alpha shapes, depending on its alpha value. For $\alpha=0$, the alpha shape is the point itself. When α is chosen large enough (infinity), the alpha shape is a convex hull that is the output of the DT algorithm. The optimal alpha can be determined experimentally to achieve a balance between size and shape/surface contours. Alternatively, a pre-determined alpha value can be set to compare the sizes and shape/surface of reconstructed data sets.
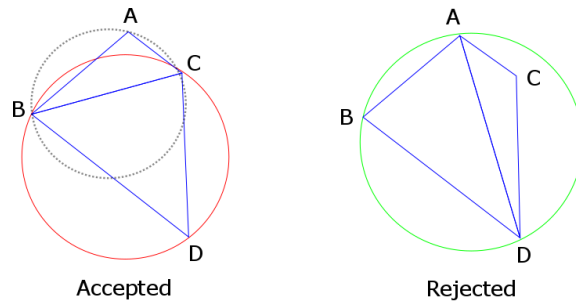
Figure 3.10 Accepted triangulation: A and D do not lie in the interior of the circles passing through "BCD" (red circle) and "ABC" (black-dashed circle), respectively. Rejected triangulation: C lies in the interior of the circle passing through "ABD" (green circle).

The concept of alpha shapes can be generalized to data points in three dimensions. According to the formal definition in Edelsbrunner's [71] earlier work, for a given set of 3D points S, an α-ball was defined as a sphere with the radius of α. The α-ball, b, moves around the entire space S and their intersection $T=$ b∩S can then include a number of points ranging between a single data point ($\alpha=0$) and all the data points ($\alpha=0$, $b=S$). Any subset T of S ($T \subseteq S$) with the size of k+1, $0 \leq k \leq 3$, defines a k-simplex, which is a convex hull of the points in T. For the larger size of the T inside the α-ball, the convex hull (obtained from Delaney triangulation and consisting of k-simplexes with $0 \leq k \leq 2$) is called an α-exposed shape $F_{k,\alpha}$. In fact, inside any α-ball in the S, the alpha shape is a polytope in which $F_{2,\alpha}$ triangles are its boundary, $F_{1,\alpha}$ lines are the edges and $F_{0,\alpha}$ points are the vertices of the triangles. The α parameter can play a role in controlling the surface size which makes it an attractive feature for data analysis. It can be used to remove the noisy and irrelevant data points from the dataset.

3.1.2.4　　Image Analysis (ITK) and Visualization Toolkit (VTK)

ITK is an open-source, cross-platform software that provides image processing tools (such as segmentation and registration) for developers. ITK is organized based on the input objects (images), and processing filters (image processing tools) that operate on the input objects. This structure of the ITK software is called ITK pipeline. The ITK pipeline is demonstrated in Figure 3.11.
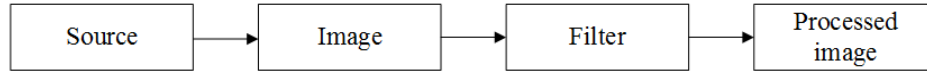
Figure 3.11 ITK pipeline
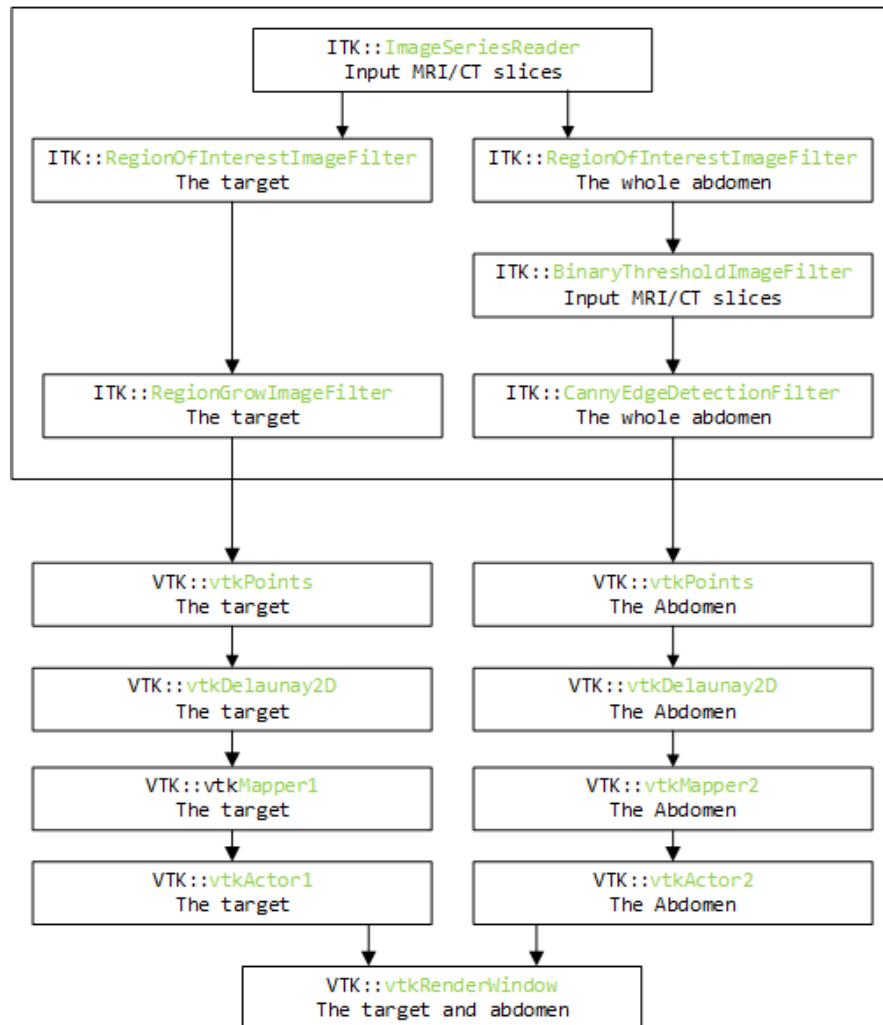
Figure 3.12 ITK-VTK pipeline (flow chart) to generate a 3D internal model.

Sources of the images in the ITK pipeline can be different types of medical images [56]. The image information, such as number of pixels (voxels in 3D), resolution, and the distance between adjacent

pixels/voxels is directly available from the source of the image data in the "Source" block of the ITK pipeline. The "Image" block in Figure 3.11 is the way in which the input data are represented in the ITK pipeline. 2D and 3D images can be optionally processed in the ITK pipeline. The "Filter" block is an image processing algorithm that operates on the input image pixel by pixel. For example, "*itkCannyEdgeDetectionImageFilter*" is a filter that detects the edges of the input image by the Canny edge method [63].

In this dissertation, the ITK pipeline was used to determine the boundaries of the patient's abdomen and the target organ in the internal model (Figure 3.8). Figure 3.12 shows the procedure of constructing the internal model in laparoscopic surgery. The upper block of the diagram in Figure 3.12 is the ITK pipeline for separating the abdominal shape and the target organ boundary from the input medical images. The ITK pipeline starts with "*itkImageSeriesReader*" to read a series of 2D images (the patient's abdominal/pelvic pre-operative CT scans). The procedure is followed by "*itkRegionOfInterestImageFilter*" to specify the region of interest around the abdomen or the target organ (uterus) in each slice of the input images. The next step ("Body Segmentation" in Figure 3.8) is segmentation in which the boundary of the abdomen and the target organ are extracted from the selected regions in each slice. "*BinaryThresholdImageFilter*" (at the right side of the ITK block in Figure 3.12) was implemented for binarizing the input images of the abdomen, and "*itkCannyEdgeDetectionImageFilter*" separated the shape of the abdomen from every slice of the input images. Similarly, in the parallel ITK pipeline (left side of the ITK block in Figure 3.12), "*RegionGrowImageFilter*" was implemented to detect and extract the shape of the target organ (uterus) in each slice of the input CT scans.

The resulting images from the ITK pipeline are converted into 3D objects (*vtkPoints* in Figure 3.12) and given to the surface reconstruction algorithm (*vtkDelaunay2D* in Figure 3.12) in VTK (visualization toolkit) software [72]. VTK is an open-source software for 3D computer graphics, image processing and visualization. It is an object-oriented program that can be implemented in high-level languages such as C++, TCL, Python, and Java. VTK is a well-adopted software that runs on multiple platforms. VTK has been widely used in numerous research areas from fluid mechanical to medical applications. A functional model of the visualization, called VTK pipeline, is shown in Figure 3.13. The pipeline starts from a source of information to an image (3D model) rendered on the screen.
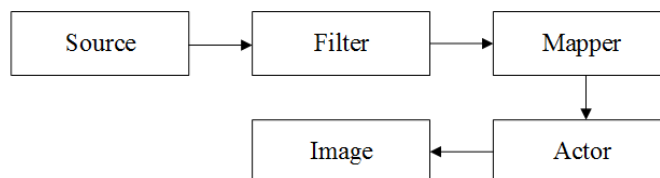
Figure 3.13 VTK pipeline

"Source" block in Figure 3.13 represents different "dataset" objects such as "cell" and "point" data. "Filter" (called process objects) is a function that operates on the input from the source block (e.g. an edge detection filter). "Mapper", in VTK pipeline, maps the input data (usually from the filters) to a graphical manifestation that can be rendered by the "Renderer" engine. Finally, "Actor" adjusts and adds the visible properties (such as transparency, color, and texture) to the object data before rendering on the output screen [72].

The dataset types in VTK are categorized into six different groups: image data, rectilinear grid, structured grid, unstructured points, polygonal data, and unstructured grid. In this dissertation, two types of the dataset were used: image data (CT/MRI slices), and unstructured point data that are captured by the Kinect device as mentioned in section 3.1.1. Image data is a matrix of 2D or 3D cells (pixels/voxels) in a rectangular/cubic shape, and unstructured points are irregular points in the space without any specific topology. The geometry of unconstructed points is completely irregular.
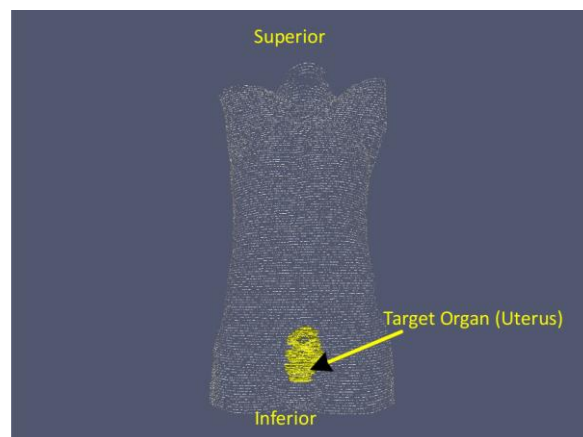
Figure 3.14 A sample 3D internal model generated in the ITK-VTK pipeline (hysterectomy procedure).

A sample of a 3D internal model by using VTK filters is shown in Figure 3.14. The output image data (processed CT scans) from ITK pipeline (the commands inside the dashed box in Figure 3.12) are converted to the 3D points for both the target organ (left side of the diagram in Figure 3.12) and the patient's external abdominal surface (right side of the diagram in Figure 3.12). Then the generated 3D points are given to the alpha shape reconstruction filter ("*vtkDelaunay2D*") to create the 3D mesh of the abdomen and target organ (Figure 3.8).

3.1.3 Alignment technique

According to the patient model workflow in Figure 3.1, the final step of creating the patient model is to align the internal model with the external model. To date, various registration techniques were proposed

for matching two congruent objects (3D models) in different applications such as object recognition, retrieval, clustering and classification. Most of the registration (alignment) algorithms use common features such as corresponding points, lines, and angles for quantifying the similarities between the two 3D models. Typically, one of the 3D objects is assumed to be the reference and the other one is transformed to be aligned with the reference shape, called the target shape. If the reference and target objects are congruent the transformation will be a linear matrix (i.e. scaling, translation, and rotation) that maps the 3D points on the target shape to their corresponding positions on the reference object. For example, four pairs of the corresponding points in Figure 3.15 can be used to calculate a linear transformation matrix that maps all the corresponding points from the target to the reference object:

  A'=TA, B'=TB, C'=TC, D'=TD (twelve equations)   (3.5)

where A,B, C and D are selected 3D points on target object, and A',B', C' and D' are the corresponding points on the reference object. **T** is the affine 4×4 transformation matrix.
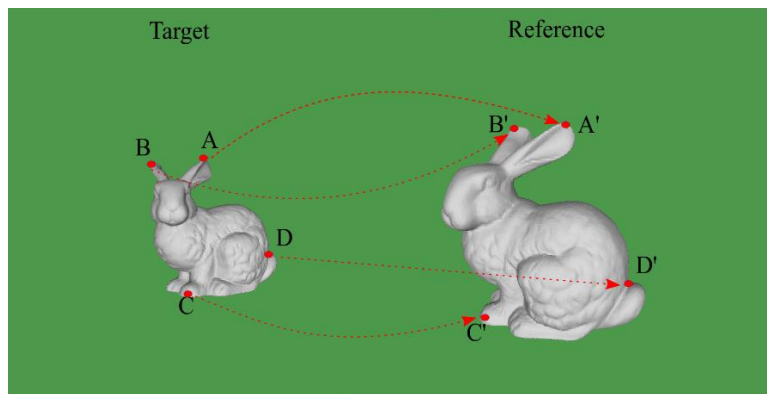
Figure 3.15 The corresponding points on the surface of two 3D objects (Stanford Bunny [52])

For aligning the internal and the external model we need to put four markers as the corresponding points on the patient's abdomen. These markers must be detectable or visible in both the internal and the external models. Having the coordinates of the markers on both models, we can use equation (3.5) for superimposing the external model on the internal model. However, using equation (3.5) for aligning the internal and the external model is not as straightforward as aligning two congruent 3D objects. The 3D medical images (captured by CT) and 3D points (captured by 3D scanners e.g. Kinect) are always accompanied by computational errors, noise, and artifacts due to the imperfect data acquisition systems. As a result, the created internal and external models are not perfectly matched, even before insufflation. It means that if we pick four pairs of the corresponding points on both internal (reference) and the external

(target) models, and put them in the equation (3.5), we will get a non-linear transformation matrix. This non-linear matrix is not a rigid transformation, and it cannot preserve the shape of the target object (the external model). In other word, the transformation matrix deforms the target object (the external model) when the corresponding points are mapped to the reference object (the internal model). Other difficulties in aligning the internal and external are as follows:

- We need to put some markers on the abdominal surface during MR/CT scanning. These markers can serve as the corresponding points for aligning the external model with the internal model. However, the markers must remain in place on the abdomen in the time interval between the MRI/CT scanning and the surgery.

- Surgical draping (to create a sterile field on the abdominal surface during surgery) usually occludes parts of the abdomen in the external model. Therefore, putting markers on the abdominal surface is not an easy task in the operating room.

- The external model is constructed from the insufflated abdomen whereas the internal 3D model is created from pre-operative images. Therefore, the transformation matrix will not be a linear map between the two models.

Instead of placing the visible markers on the abdominal surface pre- and post-insufflation, we used four points on the abdominal surface that are assumed to be fixed during insufflation. We selected the points (corresponding positions) on the anterior superior iliac (ASI position on the pelvic bone), and the two others on the 10th rib of the thoracic cage as shown in Figure 3.16.
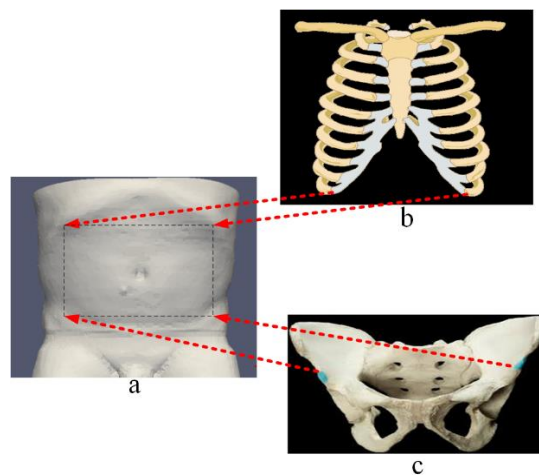
Figure 3.16 (a) Natural landmarks on the internal model
(b) Two points on the 10th rib of the rib cage
(c) Two points on the pelvic bone: Anterior superior iliac (ASI)

The points on the front edges of the rib cage and the pelvic bone can be found and segmented in the CT scans. These points are also detectable on the abdominal surface by examining the patient's abdomen before surgery. Hence, the surgeons are asked to find these points (on the abdominal surface) in the operating room and mark them so that the points can be seen in the Kinect depth images. Figure 3.17 shows a sample of the corresponding points on the internal and external models.
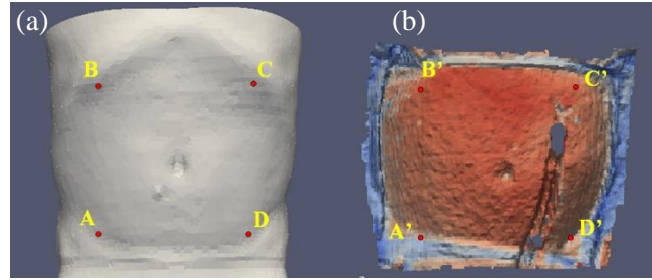
Figure 3.17 (a) Corresponding points on the internal model.

(b) Corresponding points on the external model.

Instead of using the affine transformation in equation (3.5), we can use a least-square method to align the external model with the internal model. Let $P= \{p_1, p_2...p_N\}$ and $Q= \{q_1, q_2...q_N\}$ be two sets of **N** corresponding $\mathbf{R}^3$ points in the two 3D models (for example, the number of corresponding points in Figure 3.17 is **N**=4). $\bar{p}$ and $\bar{q}$ are the average of P and Q respectively. Our goal is to find a rigid transformation (that is a linear combination of translation and rotation transformations) for aligning the two sets optimally. Here the optimal transformation is defined such that the sum of the least-square distances between the corresponding points, *L*, is minimized:

$$L= \sum_{j=1}^{N}(\mathbf{R}p_i + \mathbf{T}) - q_i)^2 \tag{3.6}$$

$$(\mathbf{R}, \mathbf{T}) = \min (\mathbf{L}) \tag{3.7}$$

in which **R**, and **T** are the unknown rotation and translation that are obtained after minimizing *L* in above equations.

After a little computation, **T**, and **R** matrices are found as:

$$\mathbf{T}= \bar{q}\text{-}\mathbf{R}\bar{p} \tag{3.8}$$

$$\mathbf{R}= V\begin{bmatrix} 1 & 0 & 0 \\ 0 & 1 & 0 \\ 0 & 0 & \det(VU^+) \end{bmatrix} \tag{3.9}$$

in which V, and U are the singular value decomposition matrices of XY^T, where X, and Y are the $3 \times N$ matrices that have $x_i = p_i - \bar{p}$, and $y_i = q_i - \bar{q}$ as their column respectively.

It should be noted that increasing the number of corresponding points makes the rotation and translation matrices (**R** and **T**) more accurate. However, choosing more than four corresponding points in the operating room is sometimes difficult, because most of the patient's abdominal surface is draped before surgery. The result of aligning the internal model with the external model is the patient-specific model as shown in Figure 3.18.
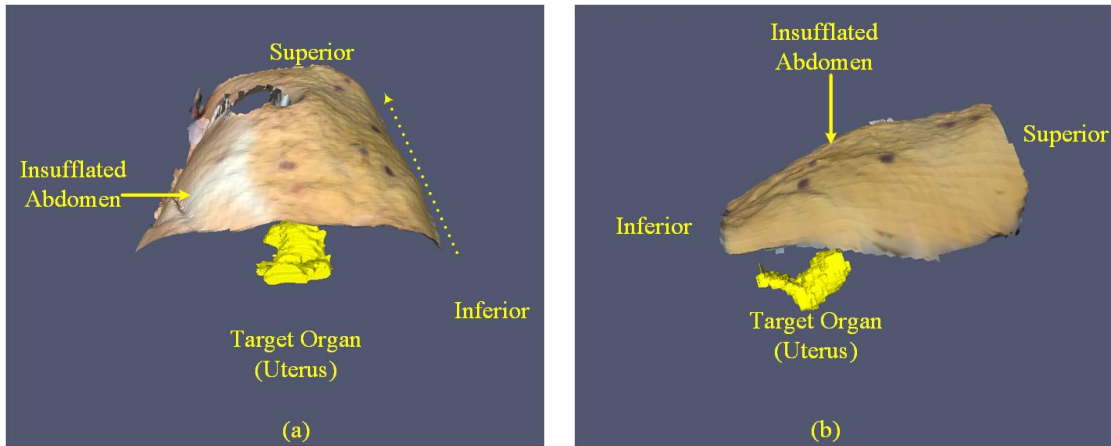
Figure 3.18 The result of aligning the external model with the internal model:

The patient-specific model (a) Front view (b) Side view

We already completed the patient-specific model, i.e. a 3D model of the patient's abdominal surface after insufflation, with the target organ embedded. This patient-specific model assists us in finding the optimal locations for the entry ports on the abdominal surface. We can first choose four entry ports on the patient-specific model, and then the goodness of our selected points is evaluated based on the accessibility of the target organ by the robot manipulators. Therefore, the robot manipulators' configuration in the space should be such that it can manipulate the surgical tools to easily reach the surgical field. That is why we need to have a mathematical representation of the robot arms, called the robot model. In fact, after docking the robot to the patient, the robot model provides necessary information about the position and configuration of the robot manipulators relative to the patient model. In the following section we will construct a robot model for the *da Vinci*, the most commonly used robotic system in hysterectomy procedures.

3.2 Robot Model

Each of the robot's (*da Vinci*) arms is a sequence of links that are connected through the joints. The

robot arms' access to the points on the patient model is a function of the robot pose and the configuration of the joints (angles) in the space, called the robot model. In the following sections we will discuss the *da Vinci Si* robot model in more detail.

3.2.1 da Vinci Manipulator Design

The robotic system used in this study is *da Vinci* surgical system [2]. The old version of *da Vinci* robot, the *Si* model, consists of four arms (manipulators), one for the endoscope and three for surgical tools; they are named ArmNo1, ArmNo2, and ArmNo3 as shown in Figure 3.19. In the *Si* model, the robot arms are attached to a central column through prismatic and revolute joints (Figure 3.19).
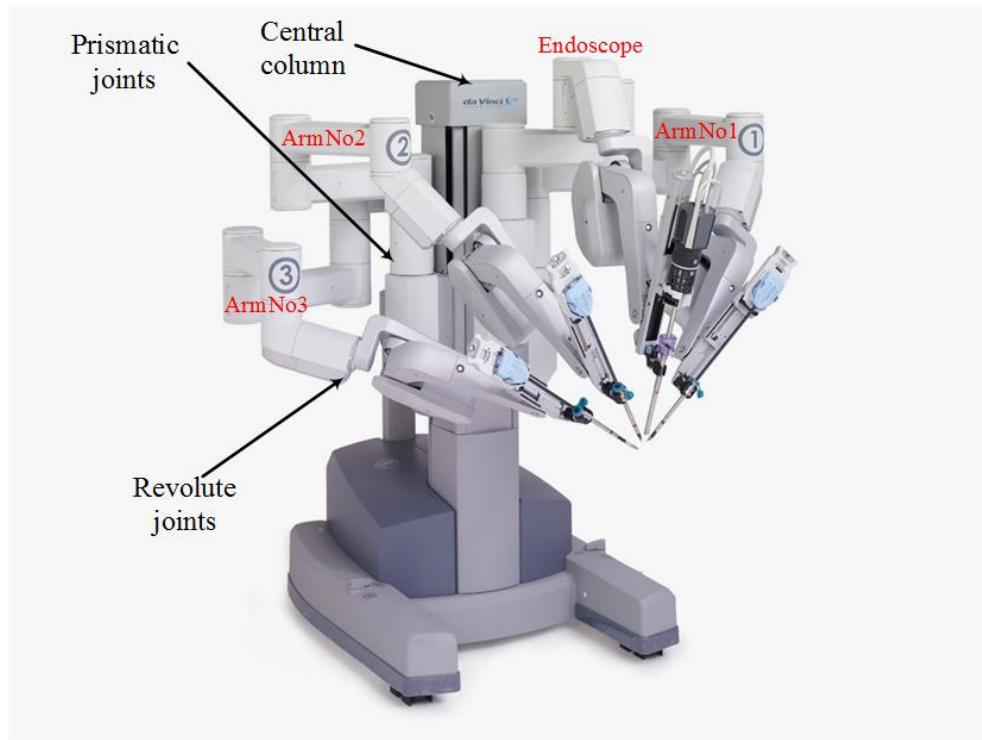
Figure 3.19 *da Vinci Si* robot [2]

The *Xi* model is the new model of the *da Vinci* surgical robotic system and features an improved design of the *Si* model's manipulators. Unlike the *Si* model, the arms in the *Xi* model are not directly attached to the central column. Instead, the arms are connected to an overhead instrument (boom) as illustrated in Figure 3.20. The overhead instrument (boom) allows the arms to rotate as a group, and provides the manipulators with more flexibility to move around in the patient, regardless of the robot's base position

before docking. Besides, in the *Xi* model, the arms are of identical articulated design, consequently the endoscope can be attached to any of the arms to provide different perspectives of the surgical site.
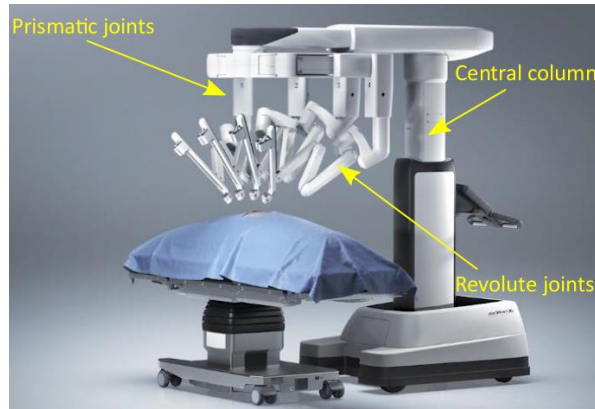
Figure 3.20 *da Vinci Xi* robot [2]
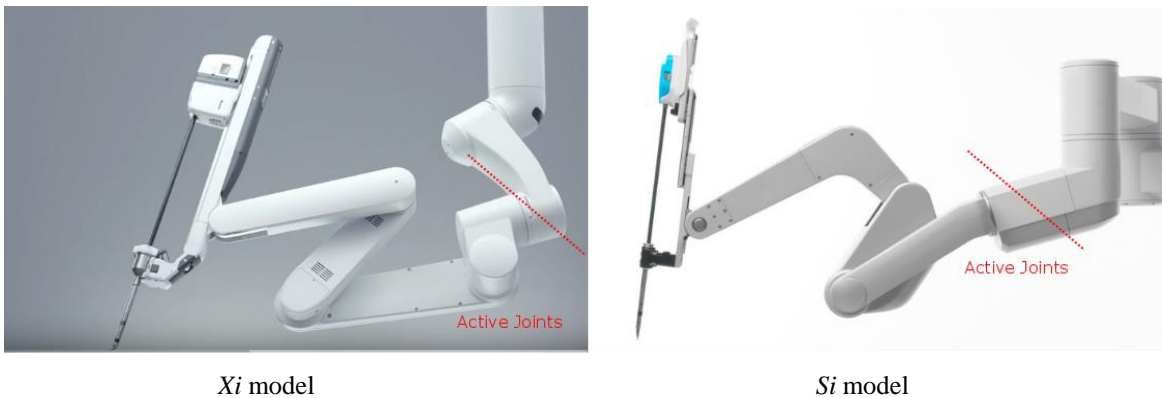
Figure 3.21 Actuated (active) joints in da Vinci robot

Each of the manipulators (arms) in both the *Si* and *Xi* models consists of a combination of actuated (active) and non-actuated (passive) joints and links. The actuated joints are powered and controlled by the surgeon through the console in the operating room. Both actuated and non-actuated joints can be manually adjusted by releasing their associated brakes (clutch button for each of the arms) when the robot is docking to the patient. The actuated joints of the *Xi* and *Si* manipulators are shown in Figure 3.21.

Once the robot is docked to the patient, the robot's manipulators' performance is only influenced by the movement of the actuated (controlled) joints during surgery [8]. Robotic literature contains various performance indices (measures) for assessing the robot manipulators' performance in MIS procedures, such as manipulability, condition number, and isotropy [9]. These performance indices are calculated from the kinematic structure of the robot manipulators. The kinematic structure of the robot is a mathematical

43

representation of the manipulators' joints and links that specifies the degrees of mobility at the entry ports on the patient model [73]. The kinematic design of the da Vinci (*Si* model) manipulators is detailed in next section.

3.2.2 Kinematic Design of da Vinci Manipulators

The da Vinci manipulators (arms) consist of a sequence of joints and links. The number of joints and the links' length differ for each of the manipulators in the *Si* model, except for ArmNo1 and Arm No2 that are of the same kinematic design. The number of joints in the endoscope, ArmNo1, and ArmNo.2 is eight (four actuated joints) and in the ArmNo3 is nine. However, the kinematic structure of the actuated joints is the same for all manipulators (endoscope, ArmNo1, ArmNo2, and ArmNo3).
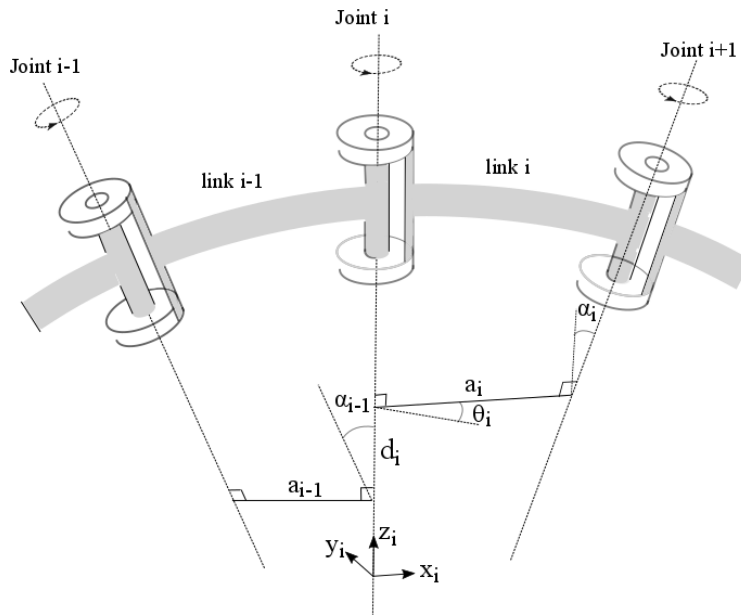
Figure 3.22 D-H parameters of a revolute joint (i) (terminology and joints shape adopted from [11])

In this dissertation we used the Denavit-Hartenberh (D-H) convention to model the Da Vinci *Si* manipulators [74]. Based on this convention, the manipulators' links and joints (including prismatic or revolute joints) are numbered from the robot base. The robot base itself is called link 0, and the next is link 1 that is connected to link 0 by joint 1. Other links and joints are named in similar way as shown in Figure 3.22. For joint i, the joint axis "i" is defined as a line that is perpendicular to the direction of rotation in the case of a revolute joint (e.g. $\theta_2 \sim \theta_8$ in Figure 3.23) or as a line parallel to the direction of translation in the case of a prismatic joint (e.g. P_1 in Figure 3.23). The shape of each link (i) is described with two variables: the length of the common line (a line that is perpendicular to the axes of joints i and i+1), $\mathbf{a_i}$, and the angle

between the projections of the i and i+1 joints axes into a plane perpendicular to the common plane, α_i. a_i and α_i are called the "**i**" th "link length" and "twist angle" respectively.

The relative position between two consequent links (e.g. "i" and "i+1" in Figure 3.22) is determined by another D-H parameter called link offset, "d_i". "d_i" is the distance between the feet of common normal on the joint axis "i" as depicted in Figure 3.22.

We used the Da Vinci *Si* for our simulation in this study. Based on the D-H convention, a simplified kinematic representation of the endoscope and the *da Vinci Si* manipulators (ArmNo1(2), and ArmNo3) are shown in Figure 3.23, 3.24, and 3.25 respectively.
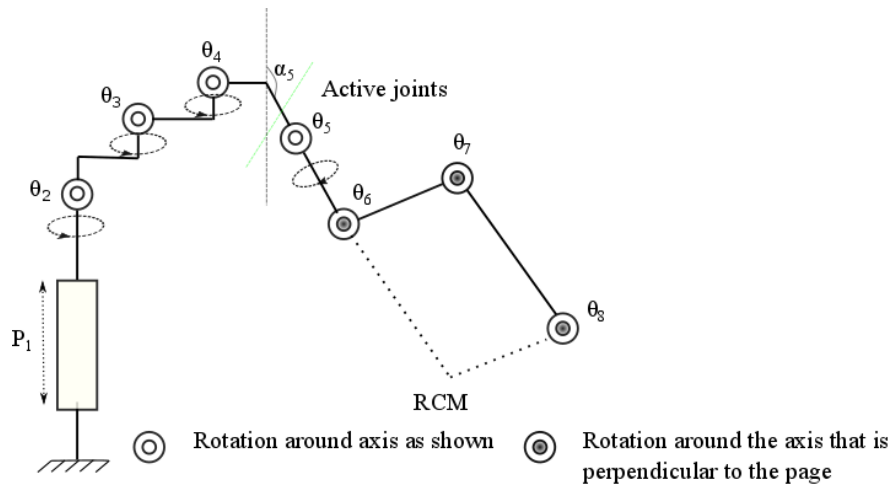
Figure 3.23 *Si* model Endoscope
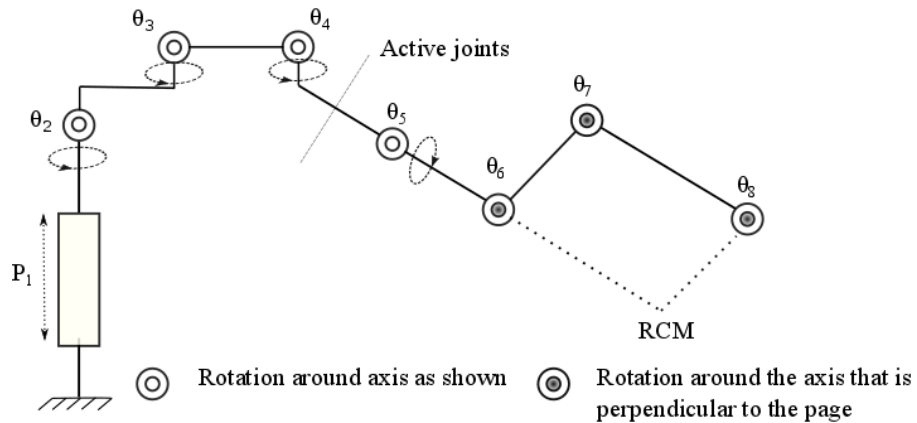
Figure 3.24 *Si* model Arm No.1 & No.2
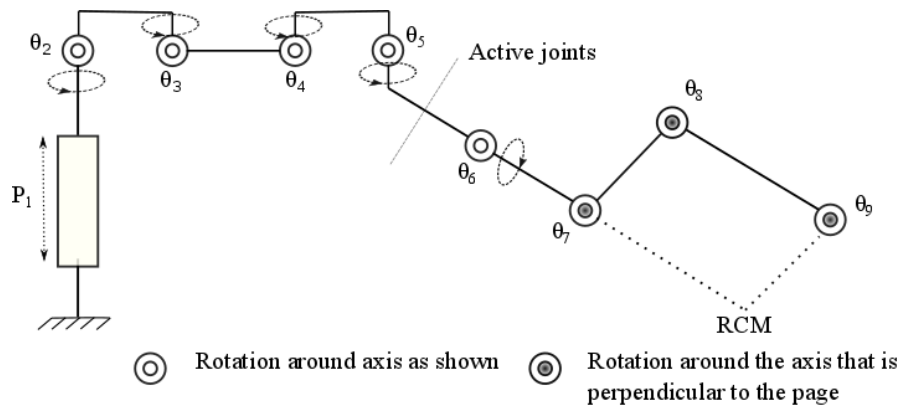
Figure 3.25 *Si* model Arm No.3

Table 3.1 D-H parameters of Da Vinci *Si* manipulator (Endoscope) [75]

Link	Joint	θ	α	d (cm)	a (cm)
Robot base					
1	P_1	0	0	d_1	a_1
2	θ_2	θ_2	0	47.76	0
3	θ_3	θ_3	0	29.10	33.02
4	θ_4	θ_4	0	11.95	33.02
5	θ_5	θ_5	$8\pi/9$	d_5	a_5
Active (actuated) joints					
6	θ_6	θ_6	0	31	0
7	θ_7	θ_7	0	25	0
8	θ_8	θ_8	0	36	-

Table 3.2 D-H parameters of Da Vinci *Si* manipulator (Arm No.1 & No.2) [75]

Link	Joint	θ	α	d (cm)	a (cm)
Robot base					
1	P_1	0	0	d_1	a_1
2	θ_2	θ_2	0	42.79	0
3	θ_3	θ_3	0	35.81	45.72
4	θ_4	θ_4	0	2.25	45.72
5	θ_5	θ_5	$\pi/4$	d_5	a_5
Active (actuated) joints					
6	θ_6	θ_6	0	31	0
7	θ_7	θ_7	0	25	0
8	θ_8	θ_8	0	36	-

Table 3.3 D-H parameters of Da Vinci *Si* manipulator (Arm No.3) [75]

Link	Joint	θ	α	d (cm)	a (cm)
Robot base					
1	P_1	0	0	d_1	a_1
2	θ_2	θ_2	0	42.79	0
3	θ_3	θ_3	0	35.81	45.72
4	θ_4	θ_4	0	2.25	45.72
5	θ_5	θ_5	0	d_5	a_5
6	θ_5	θ_5	$7\pi/12$	d_5	a_5
Active (actuated) joints					
6	θ_6	θ_6	0	31	0
7	θ_7	θ_7	0	25	0
8	θ_8	θ_8	0	36	-

The D-H parameters of the endoscope and ArmNo1, ArmNo2, and ArmNo3 are shown in Table 3.1, 3.2 and 3.3 respectively. Since Arm1 and Arm 2 in the *Si* model have same articulated design, they have the same D-H parameters in Table 3.1. It should be noted that the actual dimension of the links (in Table 3.1, 3.2, and 3.3) has not been officially released by the manufacturer, and the links' parameters were measured physically in the operating room.

3.2.3 The Inverse Kinematics problem in laparoscopic surgery

A schematic of the last three actuated joints of the *Si* manipulators ($\theta_6 \sim \theta_8$ in Figure 3.23 and 3.24, and $\theta_7 \sim \theta_9$ in Figure 3.25) is shown in Figure 3.26. The endpoint (end-effector) of the manipulators (called Remote Center of Motion: RCM) and the actuated joints ($\theta_6 \sim \theta_8$) are on same plane. Therefore, the rotation axes of the actuated joints are parallel, and the manipulators' endpoint (RCM) and the actuated joints ($\theta_6 \sim \theta_8$) form a parallelogram that rotates about the X_5 axis, called planar manipulator. The relation between the planar manipulator's joint angles ($\theta_6 \sim \theta_8$) and the coordinates of the end-effector (RCM) is described with the following equation, called forward kinematic equation:

$$\mathbf{r} = f(\boldsymbol{\theta}) \tag{3.10}$$

in which **r** is a vector that represents the coordinates of the manipulator's end-effector (RCM in Figure 3.26), **θ** is a vector showing the joint angles (e.g. $\theta_2 \sim \theta_8$ in Figure 3.26), and "f" is a function that relates the

end-effector coordinates to the manipulator configuration (the joint angles).
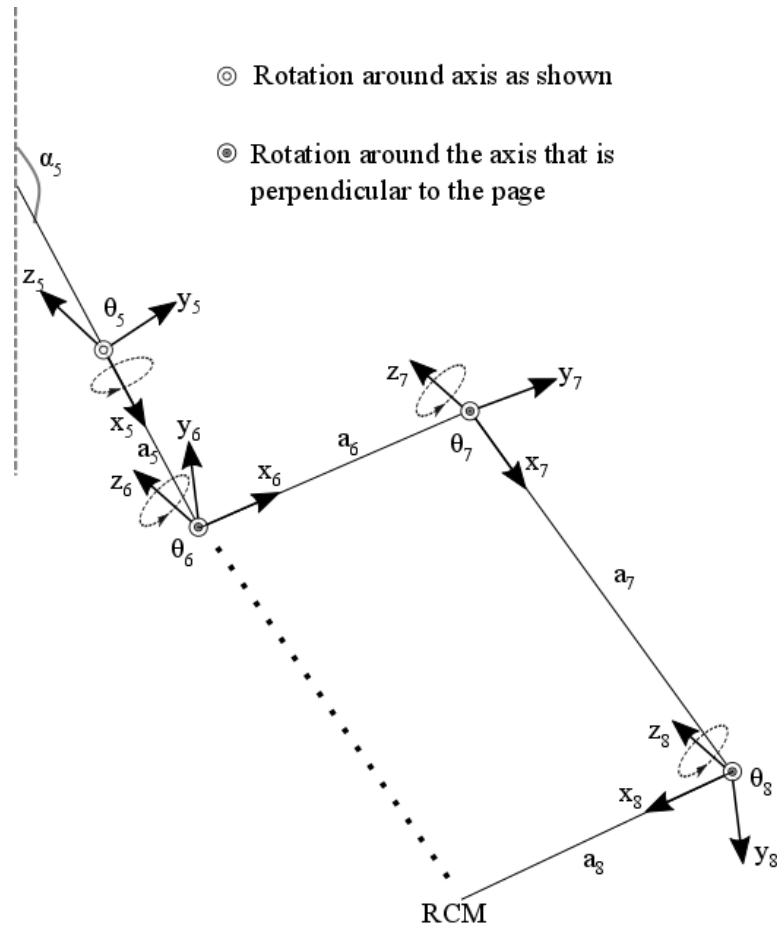
Figure 3.26 Actuated joints frames in *da Vinci Si*

To find the "f" function in equation (3.10), we need to determine the coordinates of the end-effector ("**r**") in a stationary coordinate system (frame), called the reference frame. Typically, the reference frame is put on the robot base. However, the active joints are the only ones that move the end-effector during surgery, and so are the only ones that directly influence the performance of the manipulator [8]. Therefore, we put the reference frame on the first joint of the actuated part of the da Vinci manipulator (θ_5 in the endoscope, arm No1 & No.2, and θ_6 in arm No.3). Following the D-H convention, we assign a rotating frame to each of the joints, labeled as (xi,yi,zi) for "i" th joint of the manipulator (Figure 3.26). The "z" axis of the frame (xi,yi,zi), along with the axis of rotation of the joint "i", and "x" axis of the frame (xi,yi,zi), is in direction of the links that connect the "i" and "i+1" joints. The number of joints in a planar manipulator is represented by "n", and the end-effector degrees of motion (the position and rotation of the end-effector) is represented by "m". So, for the *Si* planar manipulator m is 2 and n is 3.

Considering a transformation matrix that relates the coordinates of the entry point in the frame (x_8,y_8,z_8) to the reference frame (x_5,y_5,z_5), we can rewrite equation (3.10) as:

$$^5T_{RCM}= T_T(x_5,a_5).T_T(x_6,a_6).T_R(z_6,\theta_6).T_T(x_7,a_7).T_R(z_7,\theta_7).\,^8T_{RCM} \tag{3.11}$$

in which $T_R(z_i,\theta_i)$ and $T_R(x_i,\theta_i)$ are rotation matrices around z_i and x_i respectively, and the amount of rotation is θ_i. Similarly, $T_T(x_i,a_i)$ is the translation matrix along x_i with the amount of a_i. $^5T_{RCM}$ is the coordinates of RCM point in frame (x_5,y_5,z_5), and $^8T_{RCM}$ is the coordinates of RCM point in frame (x_8,y_8,z_8). Substituting transformation matrices on the right-hand side of equation (3.11), we have:

$$^8T_{RCM}=\begin{bmatrix} a_8C_8 \\ a_8S_8 \\ 0 \\ 1 \end{bmatrix} \tag{3.12}$$

$$T_T(x_7,a_7).T_R(z_7,\theta_7)=\begin{bmatrix} 1 & 0 & 0 & a_7C_7 \\ 0 & 1 & 0 & a_7S_7 \\ 0 & 0 & 1 & 0 \\ 0 & 0 & 0 & 1 \end{bmatrix}.\begin{bmatrix} C_7 & -S_7 & 0 & 0 \\ S_7 & C_7 & 0 & 0 \\ 0 & 0 & 1 & 0 \\ 0 & 0 & 0 & 1 \end{bmatrix}=\begin{bmatrix} C_7 & -S_7 & 0 & a_7C_7 \\ S_7 & C_7 & 0 & a_7S_7 \\ 0 & 0 & 1 & 0 \\ 0 & 0 & 0 & 1 \end{bmatrix} \tag{3.13}$$

$$T_T(x_6,a_6).T_R(z_6,\theta_6)=\begin{bmatrix} 1 & 0 & 0 & a_6C_6 \\ 0 & 1 & 0 & a_6S_6 \\ 0 & 0 & 1 & 0 \\ 0 & 0 & 0 & 1 \end{bmatrix}.\begin{bmatrix} C_6 & -S_6 & 0 & 0 \\ S_6 & C_6 & 0 & 0 \\ 0 & 0 & 1 & 0 \\ 0 & 0 & 0 & 1 \end{bmatrix}=\begin{bmatrix} C_6 & -S_6 & 0 & a_6C_6 \\ S_6 & C_6 & 0 & a_6S_6 \\ 0 & 0 & 1 & 0 \\ 0 & 0 & 0 & 1 \end{bmatrix} \tag{3.14}$$

$$T_T(x_5,a_5)=\begin{bmatrix} 1 & 0 & 0 & a_5C_{\alpha5} \\ 0 & 1 & 0 & a_5S_{\alpha5} \\ 0 & 0 & 1 & 0 \\ 0 & 0 & 0 & 1 \end{bmatrix} \tag{3.15}$$

in which "C_i" and "S_i" represent $\cos(\theta_i)$ and $\sin(\theta_i)$ respectively. Multiplying the right-hand sides of the equations (3.14), (3.13) and (3.14) we will get:

$$\begin{bmatrix} C_6 & -S_6 & 0 & a_6C_6 \\ S_6 & C_6 & 0 & a_6S_6 \\ 0 & 0 & 1 & 0 \\ 0 & 0 & 0 & 1 \end{bmatrix}\begin{bmatrix} C_7 & -S_7 & 0 & a_7C_7 \\ S_7 & C_7 & 0 & a_7S_7 \\ 0 & 0 & 1 & 0 \\ 0 & 0 & 0 & 1 \end{bmatrix}\begin{bmatrix} a_8C_8 \\ a_8S_8 \\ 0 \\ 1 \end{bmatrix}=\begin{bmatrix} a_8C_{6,7,8} + a_7C_{6,7} + a_6C_6 \\ a_8S_{6,7,8} + a_7S_{6,7} + a_6S_6 \\ 0 \\ 1 \end{bmatrix} \tag{3.16}$$

$C_{6,7,8}$ and $C_{6,7}$ are $\cos(\theta_5+\theta_6+\theta_7)$ and $\cos(\theta_6+\theta_7)$ respectively. Similarly, $S_{6,7,8}$ and $S_{6,7}$ are $\sin(\theta_5+$

$\theta_6 + \theta_7$) and $\sin(\theta_6 + \theta_7)$ respectively. Finally, multiplying the right-hand sides of the equations (3.15) by (3.16) gives us:

$$^{5}T_{RCM} = \begin{bmatrix} 1 & 0 & 0 & a_5 C_{\alpha 5} \\ 0 & 1 & 0 & a_5 S_{\alpha 5} \\ 0 & 0 & 1 & 0 \\ 0 & 0 & 0 & 1 \end{bmatrix} \cdot \begin{bmatrix} a_8 C_{6,7,8} + a_7 C_{6,7} + a_6 C_6 \\ a_8 S_{6,7,8} + a_7 S_{6,7} + a_6 S_6 \\ 0 \\ 1 \end{bmatrix} = \begin{bmatrix} a_8 C_{6,7,8} + a_7 C_{6,7} + a_6 C_6 + a_5 C_{\alpha 5} \\ a_8 S_{6,7,8} + a_7 S_{6,7} + a_6 S_6 + a_5 S_{\alpha 5} \\ 0 \\ 1 \end{bmatrix} \quad (3.17)$$

θ_5, θ_6 and θ_7 in the right-hand side of the above equation are known variables in a forward kinematic problem, and the left-hand side of the equation is an unknown position of the end-effector. In other words, for a given range of joint angles, the working space of the manipulator can be calculated from forward kinematic analysis in equation (3.17). The working space consists of the points that the end-effector of the planar manipulator can reach.

In the port placement problem, we have an inverse kinematic problem in which the coordinates of the end-effector, $^{5}T_{RCM}$ in equation (3.17), are known from the patient model, and the manipulator angles (θ_5, θ_6 and θ_7) are unknown variables. Thus, taking the derivative of equation (3.10) with respect to time, we can obtain $\boldsymbol{\theta}$ from the following equation:

$$\frac{d\mathbf{r}}{dt} = \frac{d}{dt} f(\boldsymbol{\theta}) = \frac{\partial}{\partial \theta} f(\boldsymbol{\theta}) \cdot \frac{\partial \theta}{\partial t} = J(\boldsymbol{\theta}) \cdot \boldsymbol{\theta}^{\cdot} \xrightarrow{\text{yields}} \mathbf{r}^{\cdot} = J(\boldsymbol{\theta}) \cdot \boldsymbol{\theta}^{\cdot} \quad (3.18)$$

where $\boldsymbol{\theta}^{\cdot}$ is the velocity vector of the manipulator joint angles, $\mathbf{r}^{\cdot}$ represents the speed of the end-effector, and $\mathbf{J}$ is the Jacobian matrix. Unlike the forward kinematics equations, $\boldsymbol{\theta}^{\cdot}$ in equation (3.18) is an unknown variable, and the equation must be solved for the given end-effector 3D position, $\mathbf{r}$. For a manipulator with same number of joints (n) and degrees of motion (m) J is a square matrix and the equation (3.18) can be written as:

$$\boldsymbol{\theta}^{\cdot} = J^{-1}(\mathbf{r}^{\cdot}) \quad (3.19)$$

For the *da Vinci* planar manipulator (Figure 3.26) J is not a square matrix (2×3) and θ is calculated from the following equation [73]:

$$\boldsymbol{\theta}^{\cdot} = J^{+}(\mathbf{r}^{\cdot}) \quad (3.20)$$

where J^{+} is the pseudo-inverse of the Jacobian matrix, $\mathbf{J}$, in the equation (3.18). If the Jacobian matrix

in equation (3.18) is a square matrix (m=n), then $\mathbf{J}^+=\mathbf{J}^{-1}$ ($\mathbf{J}^{-1}$ is the inverse of $\mathbf{J}$).

Equation (3.18) illustrates the relation between the manipulator's joints and the end-effector velocities. So, we can calculate the first derivative of equation (3.17) (with respect to time) to obtain the Jacobian matrix:

$$^5T_{RCM}= \begin{bmatrix} x' \\ y' \\ z' \\ 0 \end{bmatrix} = d/dt \begin{bmatrix} a_8C_{6,7,8} + a_7C_{6,7} + a_6C_6 + a_5C_{\alpha5} \\ a_8S_{6,7,8} + a_7S_{6,7} + a_6S_6 + a_5S_{\alpha5} \\ 0 \\ 1 \end{bmatrix} \tag{3.21}$$

or,

$$\begin{bmatrix} x' \\ y' \\ z' \\ 0 \end{bmatrix} = d/dt \begin{bmatrix} a_8C_{6,7,8} + a_7C_{6,7} + a_6C_6 + a_5C_{\alpha5} \\ a_8S_{6,7,8} + a_7S_{6,7} + a_6S_6 + a_5S_{\alpha5} \\ 0 \\ 1 \end{bmatrix} = \begin{bmatrix} -a_8S_{6,7,8}(\theta_6'+\theta_7'+\theta_8')-a_7S_{6,7}(\theta_6'+\theta_7')-a_6S_6\theta_6' \\ a_8C_{6,7,8}(\theta_6'+\theta_7'+\theta_8')+a_7C_{6,7}(\theta_6'+\theta_7')+a_6C_6\theta_6' \\ 0 \\ 0 \end{bmatrix}$$

$$=$$

$$\begin{bmatrix} \theta_6'(-a_8S_{6,7,8}-a_7S_{6,7}-a_6)+\theta_7'(-a_8S_{6,7,8}-a_7S_{6,7})-a_8S_{6,7,8}\theta_8' \\ \theta_6'(a_8C_{6,7,8}+a_7C_{6,7}+a_6)+\theta_7'(a_8C_{6,7,8}+a_7C_{6,7})+a_8C_{6,7,8}\theta_8' \\ 0 \\ 0 \end{bmatrix} = \tag{3.22}$$

$$\begin{bmatrix} -(a_8S_{6,7,8}+a_7S_{6,7}+a_6) & -(a_8S_{6,7,8}+a_7S_{6,7}) & -a_8S_{6,7,8} \\ (a_8C_{6,7,8}+a_7C_{6,7}+a_6) & (a_8C_{6,7,8}+a_7C_{6,7}) & a_8C_{6,7,8} \\ 0 & 0 & 0 \\ 0 & 0 & 0 \end{bmatrix} \cdot \begin{bmatrix} \theta_6' \\ \theta_7' \\ \theta_8' \\ 0 \end{bmatrix}$$

Then we can rewrite equation (3.22) as:

$$\begin{bmatrix} x' \\ y' \end{bmatrix} = \begin{bmatrix} -(a_8S_{6,7,8}+a_7S_{6,7}+a_6) & -(a_8S_{6,7,8}+a_7S_{6,7}) & -a_8S_{6,7,8} \\ (a_8C_{6,7,8}+a_7C_{6,7}+a_6) & (a_8C_{6,7,8}+a_7C_{6,7}) & a_8C_{6,7,8} \end{bmatrix} \cdot \begin{bmatrix} \theta_6' \\ \theta_7' \\ \theta_8' \end{bmatrix} \tag{3.23}$$

in which the first matrix on the right-hand side of the above equation is the *Jacobian* matrix:

$$J = \begin{bmatrix} -(a_8S_{6,7,8}+a_7S_{6,7}+a_6) & -(a_8S_{6,7,8}+a_7S_{6,7}) & -a_8S_{6,7,8} \\ (a_8C_{6,7,8}+a_7C_{6,7}+a_6) & (a_8C_{6,7,8}+a_7C_{6,7}) & a_8C_{6,7,8} \end{bmatrix} \tag{3.24}$$

It should be noted that the end-effector motion in the equation (3.22) is in x-y plane (m=2) and considering the number of joints (n=3), the Jacobian matrix size is 2×3.

Given an arbitrary point on the patient's body $\mathbf{r}(x, y)$, the equation (3.23) is solvable and the solutions are not unique (we may have more than one solution). However, a necessary condition for solving equation (3.23) is that the determinant of the Jacobean matrix is a non-zero value. Otherwise, if the determinant is zero, the problem has no solution for θ_6, θ_7, and θ_8. In other words, an arbitrary point on the abdominal surface is only accessible for the robot's manipulator if the determinant of the Jacobean matrix is not singular (non-zero).
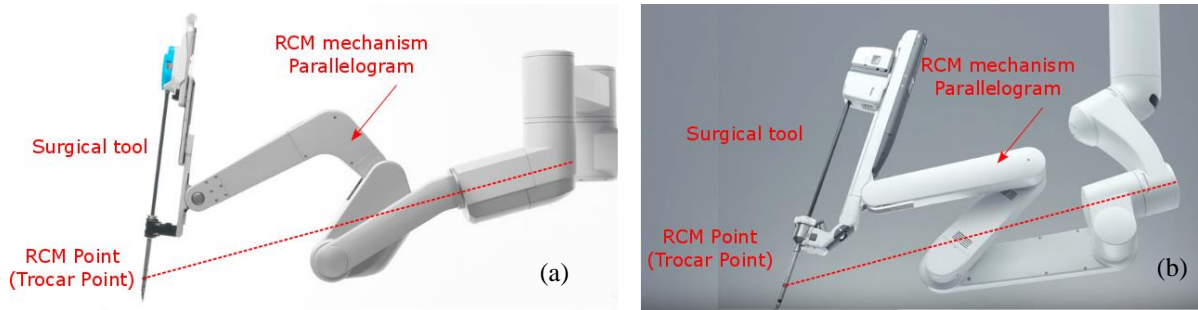
Figure 3.27 (a) Parallelogram design of the *Si* manipulator

(b) Parallelogram design of the *Xi* manipulator
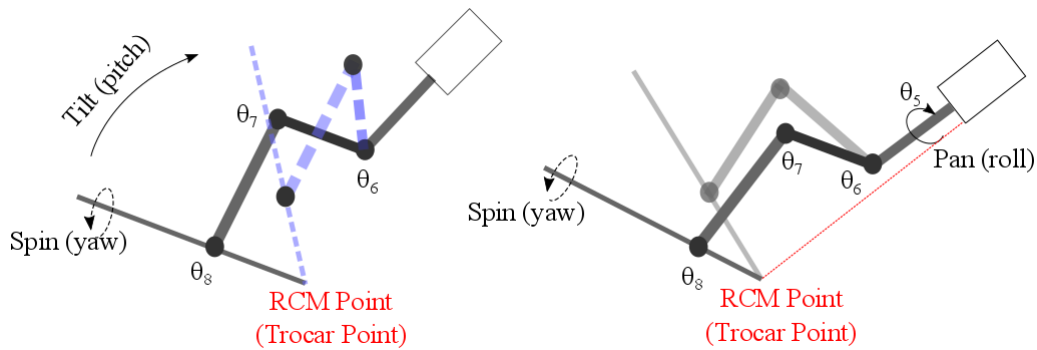
Figure 3.28 4-DOF pivoting motion at RCM point (tilt (pitch), spin (yaw), and pan (roll) rotations)

The other requirement to solve equation (19) is to define the constraints on the surgical tools' motion in the end-effector position. Since joints θ_5, θ_6, and θ_7 have parallel axes of rotation, the end-effector motion will be on the same plane as the actuated joints (z component is zero in the equation (18)). Moreover, a parallelogram mechanism (that was considered in the actuated joints' structure) keeps the end-effector as a pivoting point on the patient's body surface as shown in Figure 3.27 for the *Si* and *Xi* manipulators.

In fact, the entry point (RCM) serves as a fulcrum and provides a pivoting 4-DOF (degrees of freedom)

motion for the manipulators during surgery [32]. The 4-DOF pivoting motion consists of three rotations, and a translation at the entry point. The rotations are tilt (pitch) and pan (roll) angles about the entry point, and a spin angle about the tool axis as illustrated in Figure 3.28. The translation movement at the entry port is described by the insertion and retraction length along the surgical tool axis.

3.3 Port Placement: Problem definition

Port placement is the problem of finding the optimal locations for the entrance ports on the patient's abdominal surface. The most effective input parameters for this are the external shape of the patient's body and the surgical field (operation) area after insufflation. Thus, the entry ports on the abdominal surface must be planned in such a way that provides sufficient vision and access to the operation area (within the target organ) for the manipulators during surgery. This means that with optimal port placement the surgeon can visualize the surgical field and perform the surgical task by pivoting the endoscope and the surgical tools at the entry ports.
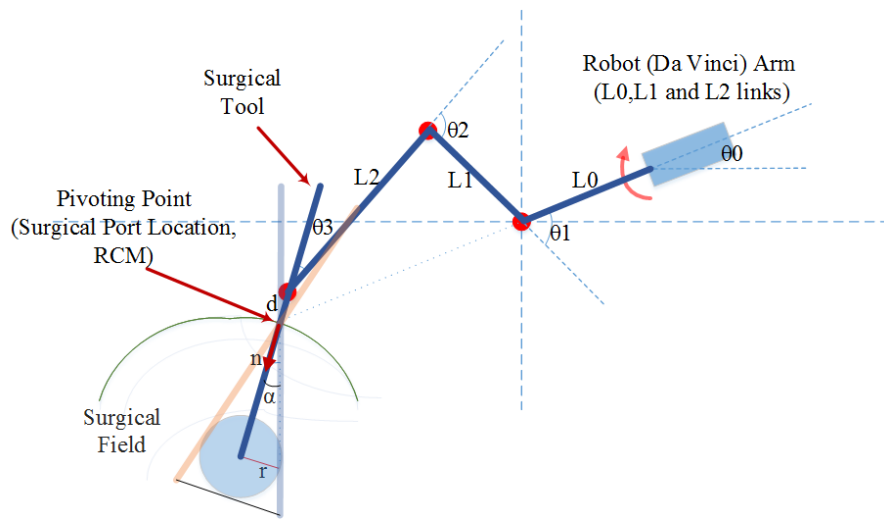
Figure 3.29 Schematic of the robot manipulator (active joints) to perform the operation

A schematic of the abdomen after insufflation, including the operation area and one of the robot manipulators, is shown in Figure 3.29. Tilting and panning motions of the surgical tools at the entry ports (by hand or by robot manipulator) create a conical volume inside the patient, the apex of which is located at the entry port and contains the operation area. The operation area (surgical site) is assumed to be a sphere that surrounds the whole target organ (the uterus in the hysterectomy procedure).

The relationship between the cone angle (α in Figure 3.29) and the radius of the sphere of the operation (r) is described by $\tan(\alpha) = r/D$, in which D is the distance between the cone apex to the centroid of the

sphere (see section 3.5.1 for more details). The robot manipulator must allow the surgical tool to pivot at the entry port such that the tooltip can reach all sides of the surgical site (the sphere of operation) during surgery. Thus, the surgical tool tip must be directed toward the sphere of the operation. To ensure that the surgical tool sweeps the whole sphere of operation, we chose an initial direction that the surgical tool is supposed to rotate around during surgery: a line that connects the remote center of motion (RCM, at entry port) to the center of the surgical field (the center of the sphere of operation), called the central direction. If the central direction (at each entry port on the abdominal surface) is accessible for the robot manipulator, the surgical tool can be tilted or panned to reach all parts of the sphere of operation.

If we represent the surgical tool axis by a normal vector, $\mathbf{n}$ (n_x,n_y), then $\mathbf{n}$ must be line the central direction as shown in Figure 3.29. Therefore, to check the accessibility of the entry ports on the abdominal surface we need to solve the inverse kinematics equation (equation (3.23)) with an additional constraint on the tools' direction:

$$x=L_0.\cos(\theta_0)+L_1.\cos(\theta_1)+L_2.\cos(\theta_1+\theta_2)+d.\cos(\theta_1+\theta_2+\theta_3) \tag{3.25}$$

$$y=L_0.\sin(\theta_0)+L_1.\sin(\theta_1)+L_2.\sin(\theta_1+\theta_2)+d.\sin(\theta_1+\theta_2+\theta_3) \tag{3.26}$$

$$n_x=\cos(\theta_1+\theta_2+\theta_3) \text{ or } n_y=\sin(\theta_1+\theta_2+\theta_3) \tag{3.27}$$

The unknown parameters in the above system of equations (20-22) are θ_1, θ_2, and θ_3. L_0, L_1, and L_2 are the robot (*da Vinci Si*) links' length (see Table 1-3). "*d*" is the trocar length that is the distance between the entry point and the robot end-effector (entry point). In the third equation (3.27) an additional constraint on the entry point was considered that keeps the surgical axis along the central direction that connects the entry point to the centroid of the target organ. Knowing the end-effector (entry point) coordinates on the abdominal surface (x,y), the centroid of the target organ will be accessible via the selected port on the abdominal surface if we can find at least one solution for the system of the equations (3.25, 3.26, and 3.27).

Now we can define the port placement problem with the input parameters more accurately: Given the patient model (with the operation area (target organ) embedded) and the robot manipulators' position, we are trying to locate the optimal placement of the ports on the patient model.

Based on type of the laparoscopic procedure in robotic surgery, the robot's manipulators can be in different positions related to the patient [76]. The guidelines from the robot manufacturer (*da Vinci*) recommends using different docking positions in various MIS procedures. For example, in hysterectomy procedures the robot is recommended to be docked between the patient's legs, called "between legs" docking, and next to the patient, called "side" docking as shown in Figure 3.30.
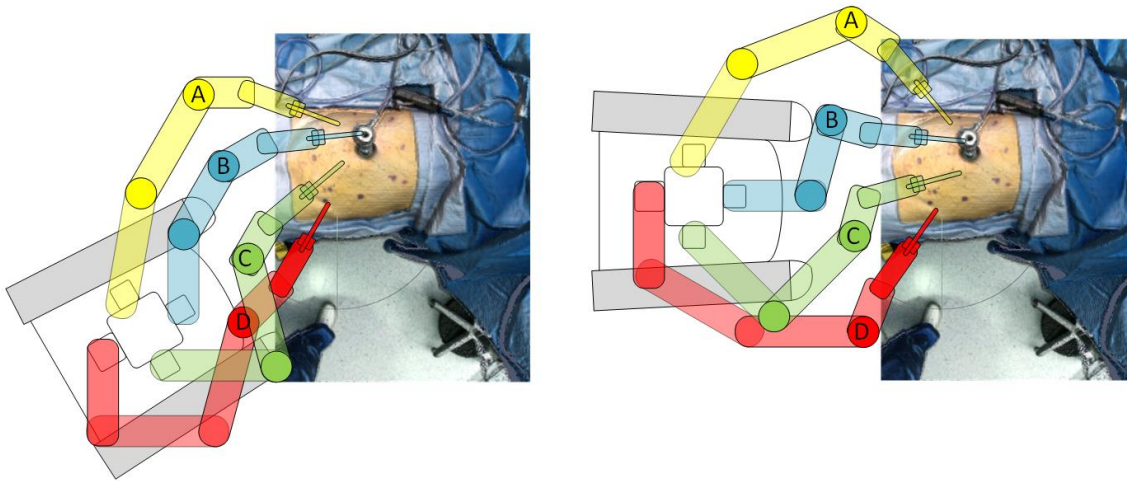
Figure 3.30 "Side" and "between legs" docking in a hysterectomy procedure

The surgeons usually mark four entry ports (for inserting the surgical tools and the endoscope) on the abdominal surface before docking the robot to the patient. Then, for each of the manipulators, the surgeon can adjust the non-actuated joints to bring the manipulators' end-effectors to the desired ports on the abdominal surface.

Using same procedure, we consider all points on the patient model as potential entry ports for the manipulators. These points are filtered in two steps: first it is checked whether the points are accessible for the manipulators (e.g. endoscope), second, the ease of manipulation of the surgical tools is measured by a performance index at the entry ports.

The performance index of the robot manipulator at each entry port is only dependent on the position and configuration of the actuated joints, so we put the reference frames in the position of the first actuated joint of the manipulators—"A" for ArmNo1, "B" for the endoscope, "C" for ArmNo2, and "D" for ArmNo3, as shown in Figure 3.30. For any specific position of the first actuated joints related to the patient's body (A, B, C, and D positions), the accessibility of the 3D points on the patient-specific model (as the manipulators' end-effectors) are checked by the determinant of the Jacobian matrix (equation (3.24)). As a result, we can find and mark the accessible points on the patient model by solving the IK Inverse kinematics) system of equations in 3.25, 3.26, and 3.27. A sample of the accessible points (on the patient model) for the endoscope arm is shown in Figure 3.31.
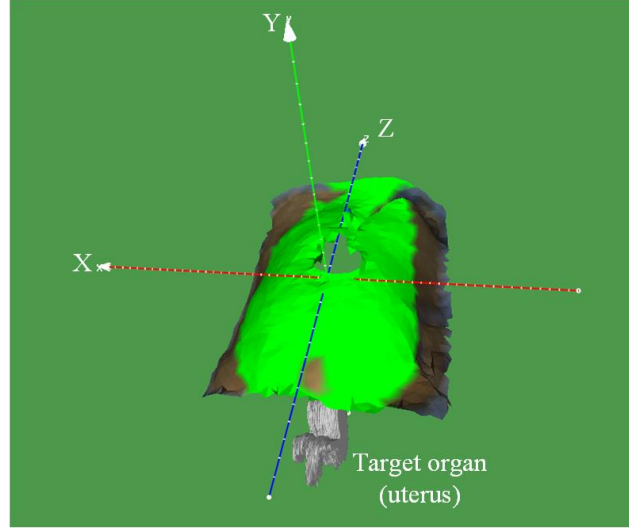
Figure 3.31 Accessible points (in green) for the endoscope, positioned at (X=0.0, Y=0.7 m, Z= 0.0)

The second step in filtering the points on the patient model is to calculate the performance of the manipulators at the entry ports. The performance of the manipulators can be measured by various performance indices defined in robotic literature, such as manipulability, condition number, and isotropy [8]. One of the most commonly used performance indices is the manipulability index. The concept of manipulability is developed based on the relationship between the velocity of the end-effector and the manipulator joints' velocity in equation (3.23), and it is defined as:

$$\begin{cases} w=\sqrt{\det JJ^T} & \text{for m}\neq\text{n (redundant manipulator)} \\ w=\det J & \text{for m=n} \end{cases} \tag{3.28}$$

where w is the manipulability index, and J is the Jacobean matrix. In fact, the determinant of the Jacobian matrix in the above equation is a measure to determine if the manipulator configuration (θ) cannot move in a certain direction [11]. For example, for a given coordinates of a point on the abdominal surface, if the manipulability index is very small (close to zero), the manipulator can't move to reach that point easily. For the rest of this dissertation we will use the manipulability index for assessing the manipulators' performance in manipulating the surgical tools at the entry ports.

Now we can calculate the performance index for the points on the patient model. The points can then be sorted according to their manipulability index. Selecting a threshold value, we can pick the points with the highest value on the manipulability index for each of the manipulators, called preliminary points for port placement. For example, the points with a manipulability index greater than the average of the manipulability of all points are highlighted in blue and shown in Figure 3.32.
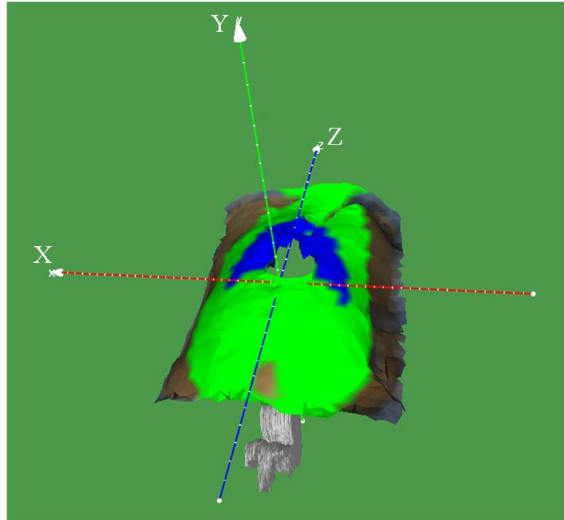
Figure 3.32 Points with a manipulability greater than the mean value (in blue) for the endoscope, positioned at (X=0.0, Y=0.7 m, Z= 0.0)

The selected preliminary points (for each of the manipulators) are given to an optimization algorithm to find the optimal locations of the entry ports on the patient's abdominal surface. More details about the optimization algorithm are discussed in section 3.5.

3.4 Target Organ Estimation

Even though the patient-specific model—the result of the alignment of the internal and external model —represents the abdominal wall after insufflation, the target organ's shape and position would not be same as it was in the internal model before insufflation. Thus, we still need to update the location and the shape of the target organ in the patent-specific model after insufflation. The aim of this section is to measure the shape and the motion of abdominal organs in the patient model caused by insufflation. We measured the volume of different abdominal organs (liver, stomach, kidneys, and spleen) in three pigs, before and after insufflation. Comparing the volume of the organs before and after insufflation, we can assess the effects of morphological changes on the size of the surgical fields (around the target organ) due to IAP. Moreover, the abdominal organs' motion (organ displacement) was calculated after insufflation. Finally, we simulated docking the robot on the pigs, and the effect of the organs' motion on the location of the ports is shown on the pigs' abdominal surface.

3.4.1 Animal Subjects

Three small white sows with the average weight of 34 kg were used in the study. The insufflation was

performed according to the animal MIS protocol, approved by the Regional Ethical and Animal Welfare Committee of the Pays de la Loire, and by the French Ministry for Research (Apafis authorization No.6176). CO_2 gas was used for the insufflation with the pressure of 14 mmHg that remained constant while scanning the abdomen (the trocar was connected to a CO_2 pipe to balance the abdominal pressure to 14 mmHg during scanning).

Figure 3.33 The experimental set-up of the pigs scanning in the MRI room

Table 3.4 Information on the pigs

Pig Label	Sex	Age (months)	Weight (Kg)	Head-Body size (m)	Number of Slices (before Insufflation)	Acquisition Matrix (before Insufflation)	Number of Slices (after Insufflation)	Acquisition Matrix (after Insufflation)	Voxel Spacing(mm) (x,y,z)
Pig 1	F	5	35	1.6	93	448×252	99	448×252	0.89×0.89×3
Pig 2	F	5	32	1.3	93	448×224	93	448×266	0.89×0.89×3
Pig 3	F	5	35	1.5	93	448×224	93	448×266	1.05×1.05 ×3

The pigs were scanned in a supine position with a MRI scanner (Siemens model, 1.5 Tesla) in the veterinary school of Nantes in France as illustrated in Figure 3.33. High-definition T2 images were captured before and after insufflation. The distance between the 2D slices and the acquisition matrices' size before and after insufflation are shown in Table 3.4. The orientation of the images was ASL (Anterior to posterior, Superior to inferior, and Left to right) for all the pigs. For the rest of this section, the X axis is along the posterior to anterior direction, Y represents the inferior to superior direction, and the Z axis is from left to right on the pigs' bodies.

3.4.2 Creating Patient 3D model

The 3D shape of the pigs' bodies (the internal model) before and after insufflation was created by the procedure described in section 3.1.2. According to the internal model workflow (Figure 3.8), the boundaries of the pigs' bodies were extracted from the 2D slices by the thresholding method. Using voxel spacing in Table 3.4, the resulted binary images (segmented parts in 2D slices) were converted to 3D points.
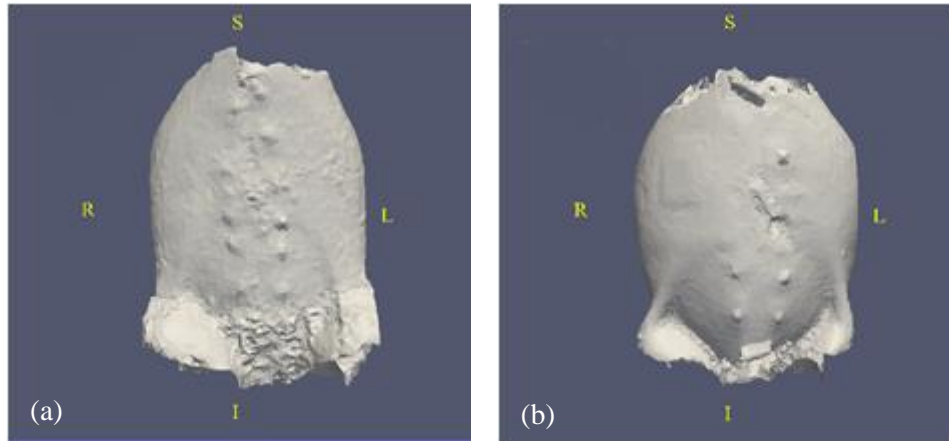
Figure 3.34 3D model of the abdomen: (a) pre-insufflation (b) after insufflation.

S: Superior I: Inferior R: Right L: Left

Finally, the generated 3D points were given to the alpha shape surface reconstruction algorithm (see section 3.1.2.3) to create a uniform mesh as shown in Figure 3.34.

3.4.3 Volume and Target Region Measurements

The 3D shape (mesh) of the pigs' liver, spleen, stomach, and kidneys (right and left) were constructed from the MRI slices before and after insufflation (except for pig2 where parts of the liver and stomach images were damaged by artifacts).
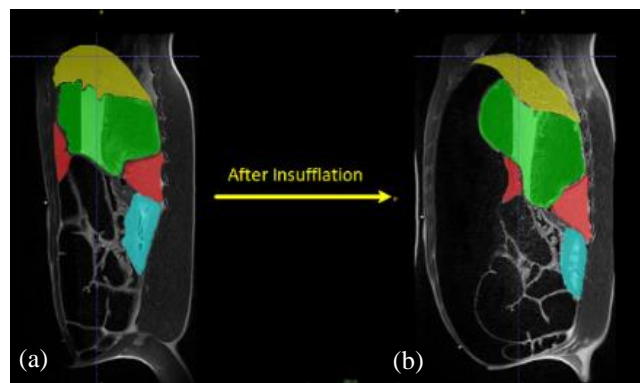
Figure 3.35 (a) Manual segmentation on a pre-insufflation slice, sagittal view

(b) Manual segmentation on a post-insufflation slice, sagittal view

(*green: stomach, red: spleen, yellow: liver, blue: kidney*)

The boundaries of the organs (liver, stomach, spleen, and kidneys) were extracted manually from T2 slices as shown in Figure 3.35, and the segmented parts (a set of contours that represent the shape of the organ in each slice) were combined (based on the algorithm in Figure 3.8) to form the 3D shapes (mesh) of the organs in the abdominal cavity. For example, the constructed 3D shape of the spleen, before and after insufflation, is shown in Figure 3.36.

(a)   (b)
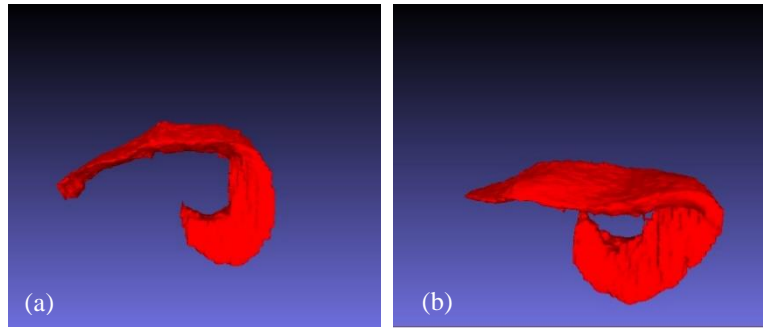
Figure 3.36 (a) The spleen in pig 2 before insufflation.

(b) The deformed spleen in pig 2 after insufflation.

It should be noted that an animal radiologist was asked to use ITK-Snap software to manually mark the boundaries of the target organ in each slice with ITK-Snap software [59]. The process of image segmentation was repeated, and the measured values (volume, displacement) were observed by the same person three times.

Table 3.5 The abdominal organs' volume measurements before and after insufflation.

The mean values are shown as mean± standard deviation

* Significant differences at P value less than 0.05

	Pig 1			Pig 2			Pig 3		
Organ	Mean Volume Before Insufflation (cm^3)	Mean Volume After Insufflation (cm^3)	P value	Mean Volume Before Insufflation (cm^3)	Mean Volume After Insufflation (cm3)	P value	Mean Volume Before Insufflation (cm3)	Mean Volume After Insufflation (cm3)	P value
Stomach	607.07±26.29	671.51±15.61	0.022*	-	-	-	436.70±11.70	509.35±13.70	0.002*
Liver	842.18±30.14	769.93±28.18	0.038*	-	-	-	965.24±23.19	856.16±20.64	0.005*
Right Kidney	106.80±3.40	66.43±1.27	<0.00005*	81.82±5.22	76.07±5.41	0.256	83.06±1.50	81.00±1.35	0.153
Left Kidney	114.80±4.74	80.88±1.26	<0.00005*	79.44±7.34	79.15±7.91	0.965	87.33±0.66	85.15±1.52	0.084
Spleen	281.28±9.23	285.48±18.92	0.7471	282.60±9.09	300.355±5.16	0.042*	240.08±7.18	247.91±5.46	0.207

The morphological changes in the liver, stomach, spleen, and right and left kidneys were observed for each pig three times after insufflation (the segmentation process was performed three times). The average volume of the organs, before and after insufflation, is presented in Table 3.5. The mean volume of the stomach increased significantly after insufflation for pig 1 and pig 3 (*P value< 0.05*). Also, the mean volume of the liver significantly decreased for pig 1 and pig 3.

The mean volume of the right and left kidneys decreased after insufflation for all the pigs. However, the mean volume differences (pre- and after insufflation kidneys) are only significant for pig 1 (*P value* <0.0005). The volume difference for the spleen is only significant for pig 2.

The volume increment after insufflation causes the radius of the enclosed sphere in Figure 3.29 to increase. Therefore, the tilt or pan angles (Figure 3.28) become larger. This means that the surgical tool at the pivot point (entry point on the abdominal surface) sweeps a larger area to have enough access to the target organ after insufflation. This might impose an additional constraint on the robot manipulators' motion within the abdominal cavity. However, for the larger organs (e.g. stomach and liver), the region of operation (surgical field) needs to be defined before surgery. This assures the surgeon that the surgical field will be accessible to the surgical tools after robot docking to the patient in the operating room.

To date, researchers have conducted different experiments to show the effects of intra-abdominal pressure (IAP) on different abdominal organs' function [77, 78, 79]. Carbon dioxide, which is the most frequently used gas for insufflation, is readily absorbed by the peritoneum in the abdominal cavity. This extra amount of CO_2 has a direct effect on the cardiovascular system, and consequently on the blood vessels' flow in the abdominal organs. For example, studies have shown the contribution of the CO_2 to increase gastric blood flow [80], and to decrease liver blood flow during laparoscopic surgery [81]. We think that the increased blood flow in the gastrointestinal tract could be the reason that the volume of the stomach of pig 2 and pig 3 increased significantly after insufflation. Similarly, the decreased volume of the liver (in pig1 and pig3), could be explained by a reduction of the blood flow in the liver due to the insufflation. However, other researchers found a significant increment in the volume of the liver after insufflation, which is in contradiction to our observations in this study [13]. Therefore, we are unable to confirm the relation between the blood flow and the volume of the visceral organs based on our observations.

3.4.4   Organ shift (Displacement) Measurements

The other purpose of our experiments was to assess the displacements of the organs due to the insufflation. For the sake of calculating the organs' displacement, the position of the surgical field (the area around the target organ) is determined by the organs' centroid coordinates. The centroid coordinates of each

of the organs are then calculated in a reference coordinate system (frame), attached to the MRI scanner:

$$x_{cm} = \frac{\sum_{i=1}^{N} x_i}{N}, \ y_{cm} = \frac{\sum_{i=1}^{N} y_i}{N}, \ z_{cm} = \frac{\sum_{i=1}^{N} z_i}{N} \tag{3.29}$$

in which x_{cm}, y_{cm}, and z_{cm} are the centroid's coordinates, and "N" is the number of 3D points existing in each organ's 3D mesh (e.g. spleen in Figure 3.36). The organ's centroid shift (displacement) is defined as the Euclidean distance between the centroid of the organ before and after insufflation:

$$D = |\mathbf{r_{cm}} - \mathbf{r_{cm0}}| \tag{3.30}$$

$\mathbf{r_{cm0}}$ (x_{cm0}, y_{cm0}, z_{cm0}), and $\mathbf{r_{cm}}$ (x_{cm}, y_{cm}, z_{cm}) in the above equation are the coordinates of the organ before and after insufflation respectively. To calculate the organs' displacement from the above equation, the pigs' bodies must be fixed during insufflation. But in practice the pigs cannot remain in the same position after insufflation, particularly when they are moved to another room (other than MRI room) for the insufflation procedure. Therefore, the pigs' 3D meshes pre- and post-insufflation (Figure 3.34) need to be registered (aligned) before calculating the displacements in equation (3.30). We used five corresponding points on the vertebras, as shown in Figure 3.37, and a least-square method (described in section 3.1.3) to align the two 3D models. The corresponding points (in the two 3D models) were assumed to be fixed during insufflation. Typically, vertebras and hard tissue (e.g. bones) are not deformed by IAP, and their locations are assumed to be static during insufflation.
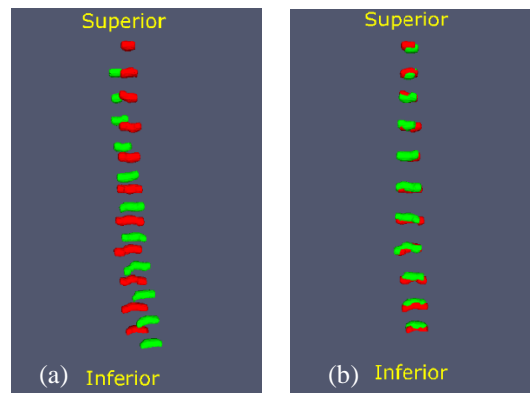
Figure 3.37 pig 2 vertebras

(a) Pre-insufflation (b) Post-insufflation

Red: pre-insufflation, Green: post-insufflation

The result of the alignment (using pre- and post-insufflation vertebras as corresponding points) is

shown in Figure 3.38.
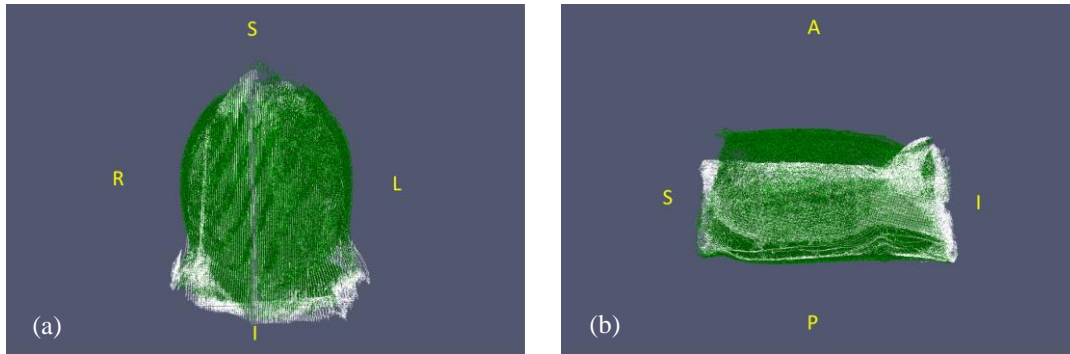
Figure 3.38 Pig 2: the result of registration.

(a) Coronal view (b) Sagittal view

Pre-insufflation: points in white, Post-insufflation: points in green.

The displacement of the organs after insufflation is measured by equation (3.30). The average of the abdominal organs' 3D motion (after three measurements) due to the insufflation are shown in Table 3.6. The maximum stomach motion for pig 1 and pig 3 is along the X axis (anterior to posterior). The maximum liver motion is along the Z axis (left to right) for pig 1, and along the X axis for pig 3. The maximum motion of the right and left kidneys is in the X-Y plane for all pigs. The spleen motion for pig 1 and pig 3 is mainly in the X direction, and for the pig 2 in the Y direction.

Table 3.6 The organs' displacements in three dimensions

Organ	Pig 1				Pig 2				Pig 3			
	Z(cm)	X(cm)	Y(cm)	D(cm)	Z(cm)	X(cm)	Y(cm)	D (cm)	Z(cm)	X(cm)	Y(cm)	D(cm)
Stomach	-1.71±0.65	-3.39±0.21	-1.78±0.13	4.21±0.45	-	-	-	-	-1.43±0.06	-0.23±0.06	0.09±0.03	1.45±0.05
Liver	-1.35±0.38	-0.21±0.32	-0.74±0.44	1.64±0.22	-	-	-	-	0.41±0.08	-1.40±0.12	0.14±0.11	1.47±0.09
Right Kidney	-0.08±0.03	1.48±0.02	-1.81±0.13	2.35±0.10	-0.16±0.18	1.38±0.12	-2.53±0.16	2.88±0.20	-0.12±0.05	-0.70±0.04	0.72±0.02	1.02±0.01
Left Kidney	1.67±0.04	-2.3±0.01	-2.17±0.12	3.58±0.09	**0.02±0.05**	**-1.33±0.06**	**-2.38±0.21**	2.73±0.17	0.04±0.03	0.65±0.02	-0.47±0.09	0.81±0.03
Spleen	-0.62±0.30	-5.18±0.17	-3.13±0.14	6.09±0.24	-3.49±0.12	-2.38±0.03	-4.76±0.19	6.37±0.10	-0.96±0.04	1.01±0.03	0.71±0.09	1.57±0.02

The mean values are shown as mean± standard deviation

(X: anterior-posterior, Y: superior-inferior, Z: left-right)

Abdominal organ motion (respiratory-related and position-related motions) was investigated in several studies [82, 83]. For example, liver and kidneys' (superior-inferior) motion due to the patient's deep breathing was measured by ultrasound in the supine position. It was reported to be about 30-80 mm for the

liver, and 20-70 mm for the kidneys [84]. Researchers also used CT scans to measure the motion of the kidneys and the liver under deep and normal breathing conditions [85]. To our knowledge, the effects of IAP (intra-abdominal pressure) on the motion of the abdominal organs (e.g. kidneys, liver…) have not been investigated yet. The results in Table (3.6) show that stomach and liver centroid motion is negative along the X axis (posterior-anterior direction). This means that the stomach and liver move downward under IAP as we expected from Figure 3.35. However, the motion of the left and right kidneys and the spleen can be positive or negative in X direction in three pigs.

To measure the effects of the organs' planar motion (X-Y plane) on the ports' location (on the abdominal surface) in robotic surgery, we assumed that the *da Vinci* (*Si* model) robot is docked between the pigs' legs as illustrated in Figure 3.39.
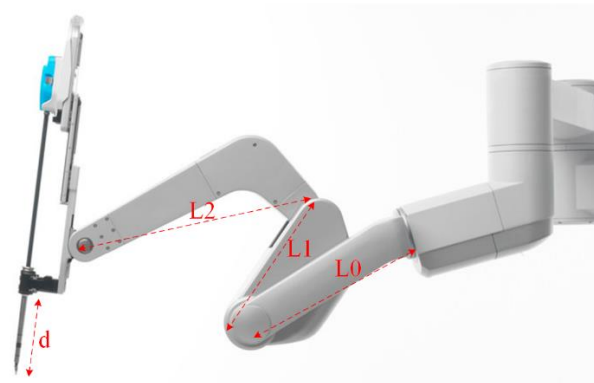
(a)
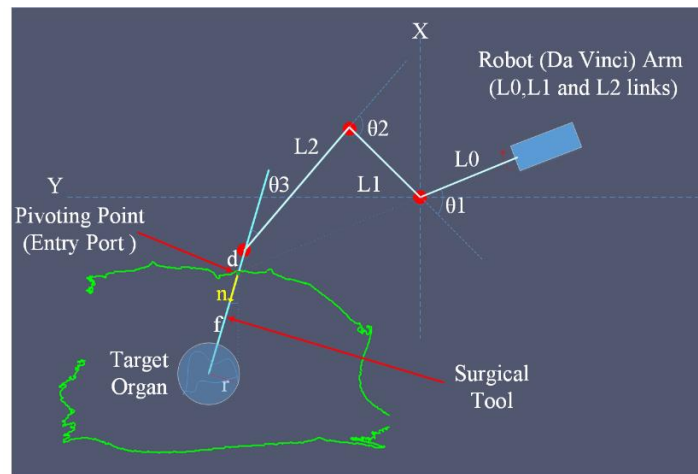
(b)

Figure 3.39 (a) *da Vinci* (*Si*) robot manipulator's three actuated joints (L_0, L_1, and L_2)

(b) Kinematic schematic of the robot manipulator, docked on the abdomen of pig 2.

Now the inverse Kinematics (IK) system of equations can be solved for the arrangement in Figure 3.39

(b). The unknown parameters in the (IK) system of equations— (3.25) and (3.26)—are θ_1, θ_2, and θ_3. L_0, L_1, and L_2 are the robot links' length. "d" is the trocar length that is the distance between the entry point and the robot end-effector (at the entry port). As mentioned earlier, an additional constraint on the entry port was considered in the third equation (3.27). The additional constraint keeps the surgical axis along a line that connects the entry port (on the pig's body surface) to the centroid of the target organ. The surgical tool axis is represented by a normal vector, $\mathbf{n}$ (n_x,n_y), in the robot coordination system as depicted in Figure 3.39. Knowing end-effector (entry point) coordinates on the abdominal surface (x,y), the accessibility of the target organ area (blue circle in Figure 3.39) in the pig's body is verified by calculating the determinant of the Jacobian matrix in equation (3.24). The target organ in Figure 3.39 (b) is in the blue circle, and the pig's abdominal surface is shown in green.

We assumed that the robot links and the target organ are on the same plane (sagittal plane in the MR coordinate system). The kidneys are selected as the target organ in our simulation (according to Table 3.6, the kidneys' motion is approximately in the X-Y plane). From Table 3.6, the minimum displacement of the kidneys—along Z axis—is about 0.02 cm that belongs to the left kidney in pig 2. Thus, we chose the left kidney in pig 2 as the target organ to investigate the effect of the kidney's planar motion on the port location on the pig's body surface as shown in Figure 3.40. The left kidney's centroid is located at (z=-4.36, x=-8.10, y=3.38), pre-insufflation, and it moves to the new position (z=-4.34, x=-9.43, y=1.00), after insufflation. The pre-insufflation and post-insufflation positions of the centroid are highlighted in red and yellow respectively, as shown in Figure 3.40. The points in green represent the pig's abdominal surface in z=-4.34 in Figure 3.40. These points were picked from the post-insufflation 3D model in Figure 3.34, and they are in slice No.32 (from left to right) that corresponds to z=-4.34.
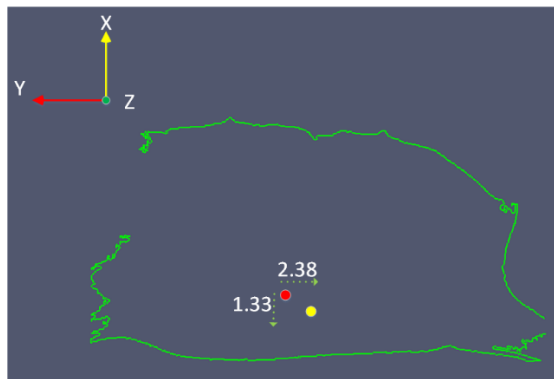
Figure 3.40 Planar motion of the left kidney's centroid due to intra-abdominal pressure (insufflation)

Red Point: The position of the left kidney before insufflation in pig 2

Yellow Point: The position of the left kidney after insufflation in pig 2

The normal vector, (n_x, n_y), is calculated for all the points on the pig's abdominal surface before and after insufflation. Substituting the pre-insufflation normal vector (n_x, n_y), and the coordinates of each entry point in the system of equations (3.25), (3.26), and (3.27), the accessible points on the insufflated abdomen were calculated and represented in red (on the pig's abdominal surface), as shown in Figure 3.41 (a).
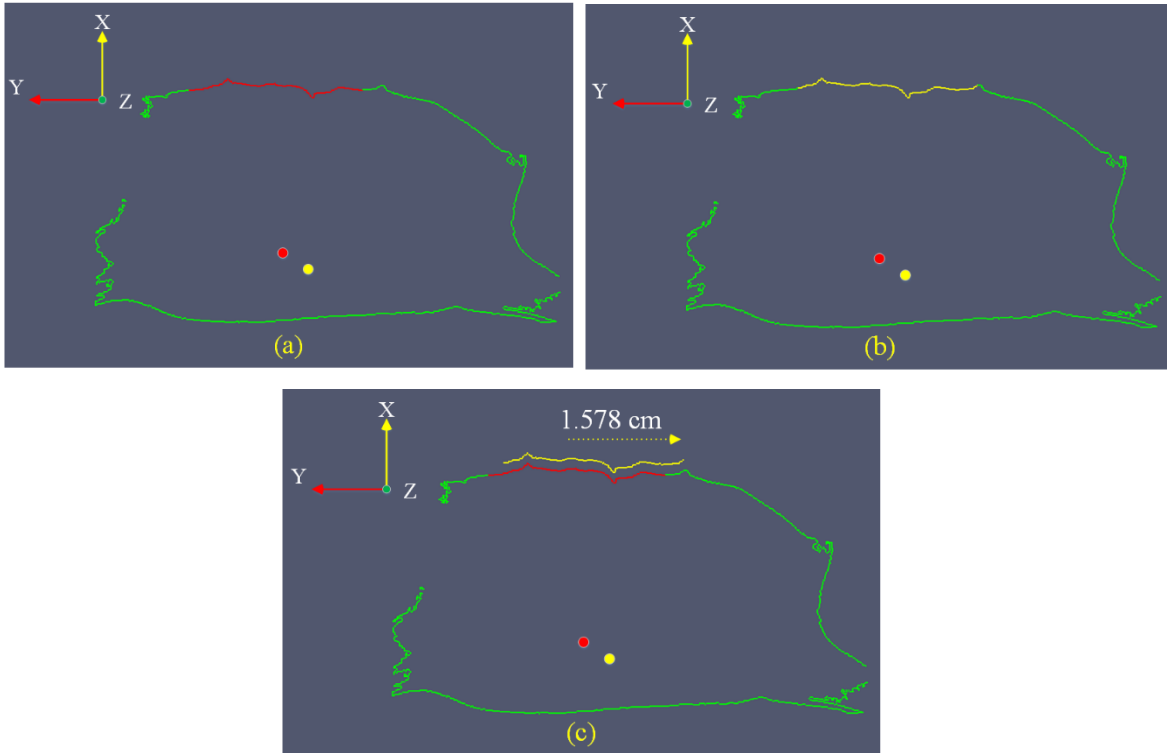
Figure 3.41 Pig 2's accessible points (on the insufflated abdominal surface) for the robot manipulator

    (a)   accessible points when the target is located in the pre-insufflation position, red point

    (b)   accessible points when the target is located in the post-insufflation position, yellow point

    (c)   comparison of the accessible points (with two different target positions)

Similarly, substituting the post-insufflation normal vector (n_x, n_y), and coordinates of each entry point in the system of equation (3.25), (3.26), and (3.27), the accessible points on the insufflated abdomen were obtained and highlighted in yellow, as shown in Figure 3.41 (b).

From Figure 3.41(c), if the target organ (left kidney) moves from pre-insufflation position to the post-insufflation position (red and yellow points in Figure 3.40), the accessible points shift to the right (1.58 cm for the left kidney in pig 2). However, the number of accessible points on the insufflated abdominal surface (length of the red and yellow points on the abdominal surface in Figure 3.41 (c)) is almost the same: the total length of the red points on the abdominal surface is 16.07 cm, and 16.25 cm for the yellow points in Figure 3.41 (c).

To summarize the results in this section, we should mention that the planar motion of the target organ (centroid of the left kidney in the x-y plane) will shift the accessible points on the abdominal surface. Also, the target point motion within the abdominal cavity (due to insufflation) could change the number of accessible entry ports on the abdominal surface. Therefore, we can conclude that the morphological alterations of the abdominal surface and the target organ's motion due to insufflation need to be involved in our solutions for the port placement problem in robotic surgery.

From the results of the three pigs in Table 3.6 it is hard to say which direction the right and left kidneys move after insufflation. However, the average of the right and left kidneys' motion in three pigs is approximately 0.23 cm in Z direction, -0.13 cm in X direction, and -1.14 cm in Y direction. Since the pigs were very young, so we were not able to detect and segment the uterus from the MRI images. We assumed that kidneys in the pigs' body are similar to the uterus in the human body, so we will use the measured kidneys' shift in the pigs' bodies for estimating the uterus' motion in the human body for hysterectomy procedures.

3.5 Optimization

Definition of the problem (Input parameters and the goal of optimization)

The goal in optimizing the port placement problem is to find the optimal locations of the ports on the abdominal surface. Optimal locations are the 3D points on the abdominal surface that provide maximum accessibility (or visibility for the endoscope) to the operation area for the surgical tools. Besides, the optimal positions of the entry ports must prevent internal and external collisions between the robot manipulators during surgery.

To achieve this goal, researchers have defined various performance indices to assess the goodness (suitability) of the entry ports (the manipulators' end-effectors) in robotic surgery. Most performance indices were defined in relation to the robot manipulators' configuration (and the end-effectors' position) regardless of patient model (visibility and accessibility to the target organ) [8]. To include the patient model in the optimization problem, other researchers suggested to use another performance index, called the efficiency index, to evaluate the reachability and visibility of the operation area [9].

Using the efficiency index and the performance of the manipulators (and the endoscope arm) at the entry points (manipulability index), we can divide the optimization process into the following steps:

1. Check accessibility

The accessible positions for the robot manipulators on the patient model are determined regarding the manipulators' configuration and the volume of the operation inside the patient (see Figure 3.29). The

volume of the operation is defined based on the target organ's location and the area that surrounds the target organ in the 3D patient model (the sphere of operation in Figure 3.29).

2. Calculate performance index

The manipulators' performance index is calculated at every accessible position (point) on the abdominal surface (patient model). This means that for each of the manipulators, we can assign the calculated performance indices to each of the accessible points on the abdominal surface. In our project we used the manipulability index (see section 3.3) as the manipulators' performance index. However, depending on the robot's capability to perform different tasks, other performance indices (such as condition number, isotropy…) that have been defined in robotic literature can be used as performance index in the port placement problem [9].

3. Pick the preliminary points

Taking the average (Mean) and the standard deviation (STD) of the manipulability of the accessible points, we define a manipulability threshold as T=Mean+STD for each of the manipulators (and the endoscope arm) separately. The accessible points whose manipulability is greater than the threshold, T, are selected as preliminary points for the entry port of the manipulators (and the endoscope arm). We label the preliminary points (preliminary port locations) on the patient model as $M(t_1)$, $M(t_2)$, $M(t_3)$, and $M(t_e)$. The $M(t_i)$ represents the highest manipulability region for the manipulator number **i** in *da Vinci Si* model, and $M(t_e)$ indicates a region with the highest manipulability for the endoscope arm. A sample of the points with manipulability greater than the selected threshold is shown in Figure 3.42—the endoscope is positioned at (0.0, 0.75, 0.05) m, ArmNo1 is positioned at (0.25, 0.60, -0.05) m, ArmNo2 is positioned at (-0.25, 0.60, -0.05) m, and ArmNo3 is positioned at (0.50, 0.20, -0.10) m.
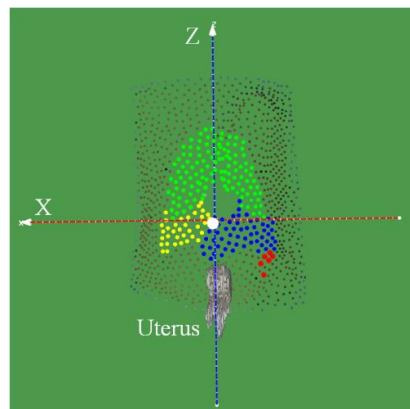
Figure 3.42 $M(t_1)$, M(t_2), M(t_3), and M(t_e) regions on the patient's abdominal surface in a hysterectomy procedure
$M(t_1)$ is the points in yellow, $M(t_2)$ is the points in blue, $M(t_3)$ is the points in red, and $M(t_e)$ is the points in green

4. *Determine the working space of the surgical tools and the endoscope (working volume).*

The working volume of the surgical tools (robot manipulators) and field of view of the endoscope are determined inside the patient model. The working volume is a cone-shaped area with its apex located at the entry port; its base must include the target region (see section 3.5.1).

Calculate the efficiency of the preliminary ports (efficiency index)

A set of four points is picked from M_{t1}, M_{t2}, M_{t3}, and M_{te} to serve as the entry ports' location for the surgical tools and the endoscope respectively. The suitability (goodness) of this set is evaluated by defining an efficiency index as [9]:

$$E(t_1, t_2, t_3, t_e) = \frac{\max \ (W_e \cup W_{t1} \cup W_{t2} \cup W_{t3})}{\max W_e} \qquad (3.31)$$

in which W_e is the working volume of the endoscope. W_{t1}, W_{t2}, and W_{t3} are the working volume of the three surgical tools (manipulators) in da Vinci Si model (see Figure 3.29). The efficiency index in equation (3.34), E, is the ratio of the degree of manipulation to the field of view by the endoscope arm, and it ranges from 0 to 1. Ideally we are seeking for the optimal set of four preliminary points (belong to $M(t_1)$ …) to maximize the E value as one of the goals of the optimization problem.

5. *Collision prediction*

It is an algorithm for calculating the overlap between the working volumes of the selected port in step 3. The measured overlaps between each pair of working volumes (see section 2.5.1) inside the patient is called the internal collision index for each set of three entry ports of the manipulators:

$$C_{12} = W_{t1} \cup W_{t2} \qquad (3.32)$$

$$C_{13} = W_{t1} \cup W_{t3} \qquad (3.33)$$

$$C_{23} = W_{t2} \cup W_{t3} \qquad (3.34)$$

in which C_{ij} , called the collision index, is the intersection volume between the surgical tools pertaining to the robot number i and j in the Da Vinci *Si* model.

6. *Select the optimal port placement*

This is the final step of the optimization process where we can define the problem with the input parameters (M_{t1}, M_{t2}, M_{t3}, M_{te}) and the goals of optimization. We already calculated the efficiency, $E(t_1, t_2, t_3, t_e)$, and the collision indices (C_{ij}) for each set of four preliminary points on the abdominal surface. The goal of the optimization is to select one or more sets of four points (obtained in step 3) that maximize the efficiency index E while minimizing the collision indices (C_{ij}). In other words, the optimal port placement is a multi-objective optimization problem that is summarized as:

$$G(M_{ti}) = G(E(t_1, t_2, t_3, t_e), C_{12}, C_{13}, C_{23})\ 1 \leq i \leq 4 \qquad (3.35)$$

where the G is a function that maximizes E and minimizes C_{12}, C_{13}, C_{23}. More details about solving the above equation by the Pareto method of optimization are discussed in section 3.5.3. In the following subsections (3.5.1 and 3.5.2) we will describe some mathematical methods to compute the collision and efficiency indices in the optimization process.

3.5.1 Collision and efficiency Index (Intersection of the cones)

Pan (roll) and tilt (pitch) motions of the surgical tool at the entry port on the patient's abdomen create a circular cone-shaped space inside the patient, called the working volume (space) of the robot arm (surgical tool), as shown in Figure 3.43. In fact, each entry port on the abdominal surface acts as a pivot (fulcrum) point, and the working volume of the surgical tools is considered as a circular cone with its apex located at the entry port, and containing the area of operation (the surgical field) as shown in Figure 3.43.
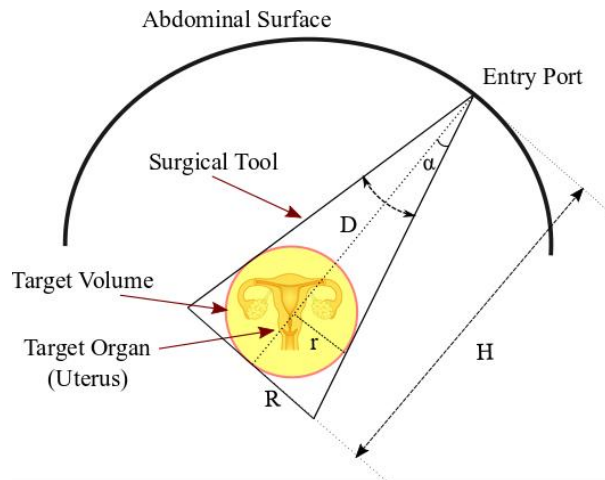
Figure 3.43 The working volume around the target organ (uterus) in a hysterectomy procedure
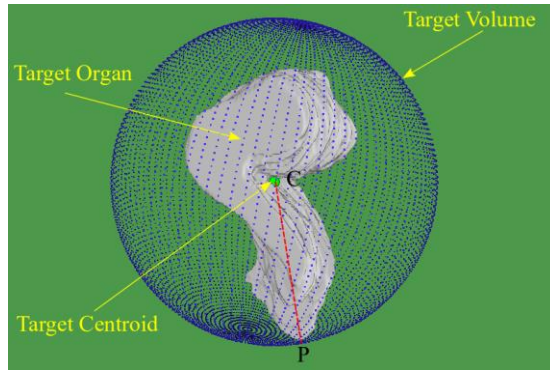
Figure 3.44 The target volume (sphere) around the target organ (uterus) in a hysterectomy procedure

The area of operation is represented by a sphere that is centered at the centroid of the target organ. This sphere is called the target volume or the sphere of operation. Using 3D points of the target organ (generated by ITK-Snap software), the central mass of the target organ is obtained from equation (3.29) as depicted in Figure 3.44. Also, the radius of the target volume is determined by calculating the Euclidean distance between the farthest point of the target organ ("P" in Figure 3.44) to the centroid of the target organ ("C" in Figure 3.44). It should be noted that, depending on the type of surgical procedure and organ size, the target volume can be either the whole organ or only the diseased regions of the organ. In our project, we assumed that the entire area of the target organ (uterus) needs to be accessible for the surgical tools, as in most hysterectomy procedures.
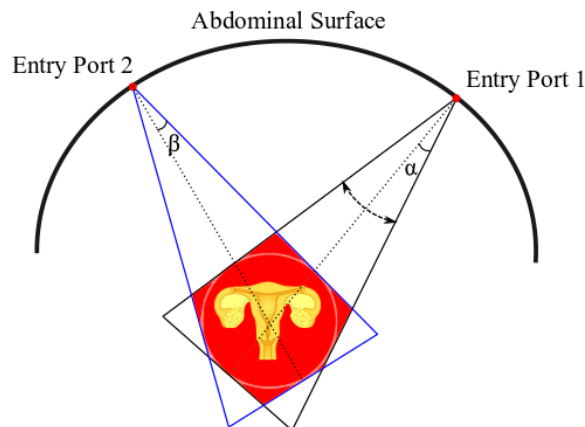
Figure 3.45 The overlap between the working volumes of two surgical tools in a hysterectomy procedure

After calculating the radius of the target volume, $\mathbf{r}$, the cone's height is calculated by $\mathbf{H}=\mathbf{D}+\mathbf{r}$, in which D is the distance between the entry port (the cone's apex) to the centroid of the target organ (Figure 3.43). The radius of the cone's base, R, is obtained by the following equation:

$$\frac{r}{R} = \frac{D}{H} \tag{3.36}$$

Considering two entry points on the abdominal surface, the collision risk between surgical tools is determined by measuring the overlap between the working volumes of the surgical tools as shown in Figure 3.45.

There are two ways to calculate the volume of the intersection between two working volumes: geometrical and computational methods. The geometrical method is an exact way to measure the intersection between two cones as shown in Figure 3.46. For example, Beyer et al. used a complex geometrical method to obtain a formula to calculate the intersection volume of two circular cones [86]:

$$V_{cones} = \frac{4}{3} \times \frac{d^3 a^2}{1-a^2 b^2}\left[\frac{a(1+b^2)\sqrt{(b^2-a^2)}}{b^2(1+a^2)^2} + \frac{1}{\sqrt{1-b^2 a^2}}\tan^{-1}\left[\frac{a(1+b^2)}{\sqrt{(b^2-a^2)(1-b^2 a^2)}}\right]\right], a = \tan\alpha, b = \tan\beta \tag{3.37}$$

in which V_{cones} is the intersection between the two cones in Figure 3.46. For each cone, α is the angle between the cone's surface and the cone's axis. β is the angle between each of the cone's axes and the line joining the two apexes.
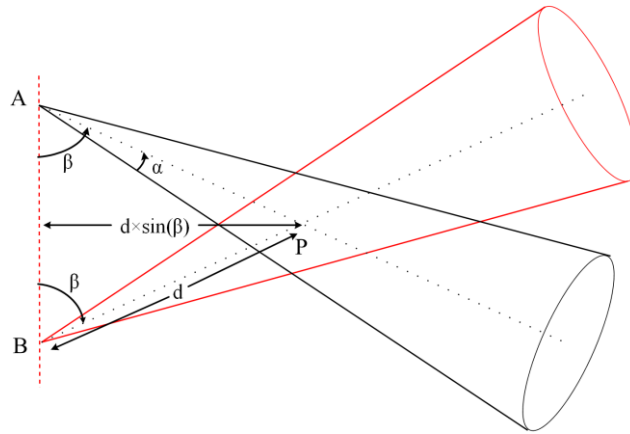
Figure 3.46 The overlap between the working volume of two surgical tools (the cone shapes adopted from [86])

The cones' axes cross at a common point, P, with the apexes of the cones in an equal distance from P.

The essential assumption of Beyer's formula is that the two cones must be congruent. This means that before using the formula we must ensure that the cones' heights and cross sections are identical. Therefore, when the working volumes of the surgical tools (cones in Figure 3.45) are not identical (different heights or cross sections) the formula does not work properly for computing the overlap volume.

As an alternative to the geometrical solution, we can use a computational method to calculate the

intersection of the working volumes. The first step in our computational method is to fill the working volumes of the cones with small 3D points (dots). This process is called discretization. A sample of a discretization process is shown in Figure 3.47. The next step is to find and count the points that belong to both cones. These points are called common points and represent the volume of the overlap between the two working volumes. An algorithm for checking if a point is inside a cone is shown in Figure 3.48. Figure 3.49 shows a sample of the overlap volume found by the discretization method.

The accuracy of the computational method is dependent on the density of the points that are distributed over the cones. For more accurate results we distributed 334,300 points over a cone with H=1 cm, and R=0.25 cm.
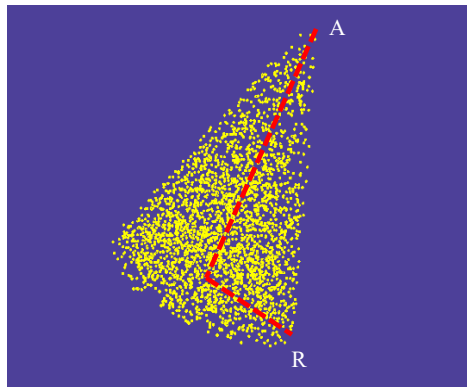
Figure 3.47 A 3D-dimensional cone filled with 3D points.

A: cone's apex **R:** cone's bottom radius

1. Calcualte normal (unit) vector, n
2. Calculate AP vector
3. Calculate r, h, and r_P
4. Check if the point is inside the cone:
$H \geq h$ & $AP.n \geq 0$ & $r_P < r$
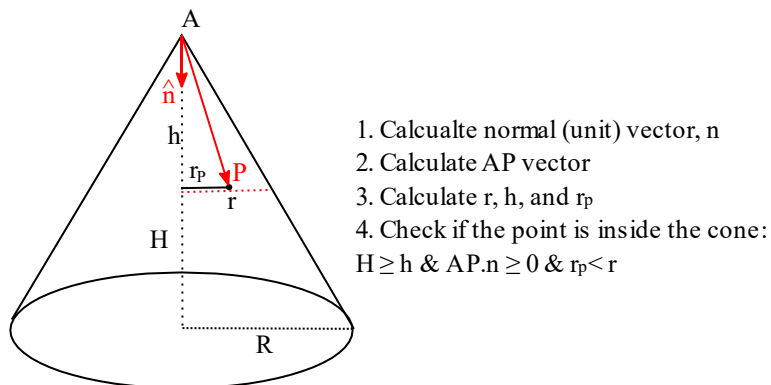
Figure 3.48 An algorithm for checking if a point, P, is inside a cone

(**H** is the cone's height, and **R** is the radius of the cone's bottom)
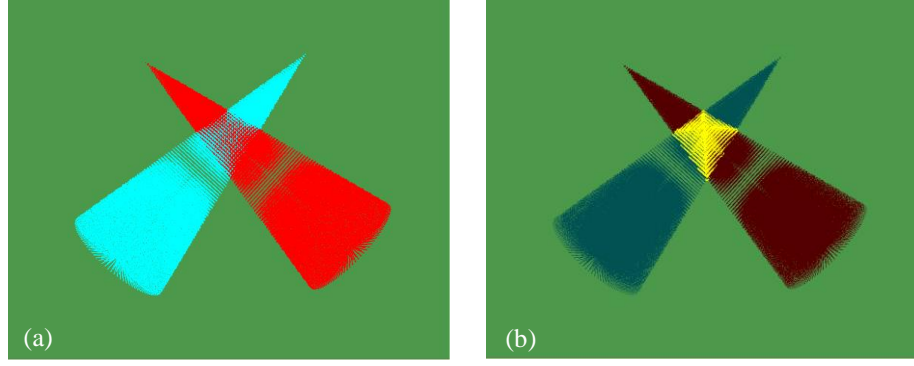
Figure 3.49 The result of the discretization method to find the intersection volume of two working volumes

(a) Two intersecting cones (working volumes) (b) The cones' intersection (overlap) is highlighted in yellow

Now we can calculate the collision indices between each of the two surgical tools (C_{12}, C_{13}, C_{23} in equation (3.35)). For computing $E(t_1, t_2, t_3, t_e)$ in equation (3.35), we count the common points that belong to the working volumes of the tools and the endoscope simultaneously. We should note that the working volume of the endoscope is defined based on the field of view of the camera at the entry point. The endoscope camera used in *da Vinci* system has 60 degrees field of view in horizontal and 70 degrees in vertical planes.

3.5.2 Multi-Objective Optimization: Pareto-Optimal Solution

We already defined the goals and the inputs of the optimization problem in equation (3.35). The goals are to minimize the collisions between the tools (C_{12}, C_{13}, C_{23}), and maximize the efficiency index, $E(t_1, t_2, t_3, t_e)$ in the equation (3.35). Thus, we can restate the optimization problem as follows:

$$S = \text{Min } \mathbf{G}(X) = \text{Max } E(X) \text{ \& Min}(C_{12}(X), C_{13}(X), C_{23}(X)) \tag{3.38}$$

in which X is a set of four points p_1, p_2, p_3, p_e that belong to M_{t1}, M_{t2}, M_{t3}, M_{te} respectively (M_{t1}, M_{t2}, M_{t3}, M_{te} are preliminary points for the manipulators and the endoscope respectively). *S* in the equation (3.38) is an optimal solution that maximizes the efficiency index and minimizes the collision indices at the same time.

There are various techniques to solve multi-objective problems such as scalarization, the ε-constraints method, and multi-level programming. In this dissertation, we used optimal Pareto (Pareto front) for finding the optimal solutions for our multi-objective optimization problem in equation (3.38) [12]. Based on the Pareto front definition, if X* belongs to the Pareto solution of equation (3.38) then we must have:

$$\text{If } X^* \in S \rightarrow E(X) < E(X^*) \text{ and } C_{ij}(X) > C_{ij}(X^*) \tag{3.39}$$

This means that X^* is an optimal Pareto if all other vectors X have at least a higher value $C_{ij}(X)$ for the collision index or have a lower value $E(X)$ for the efficiency index. We used the "rPref" package of R software to find the optimal solution [87, 88]. To make sense of the Pareto front in the port placement optimization, we reduced the objectives to maximizing $E(X)$ and minimizing $C_{12}(X)$ (see equation 3.38). The results of the Pareto front with these two objectives are shown in Figure 3.50.
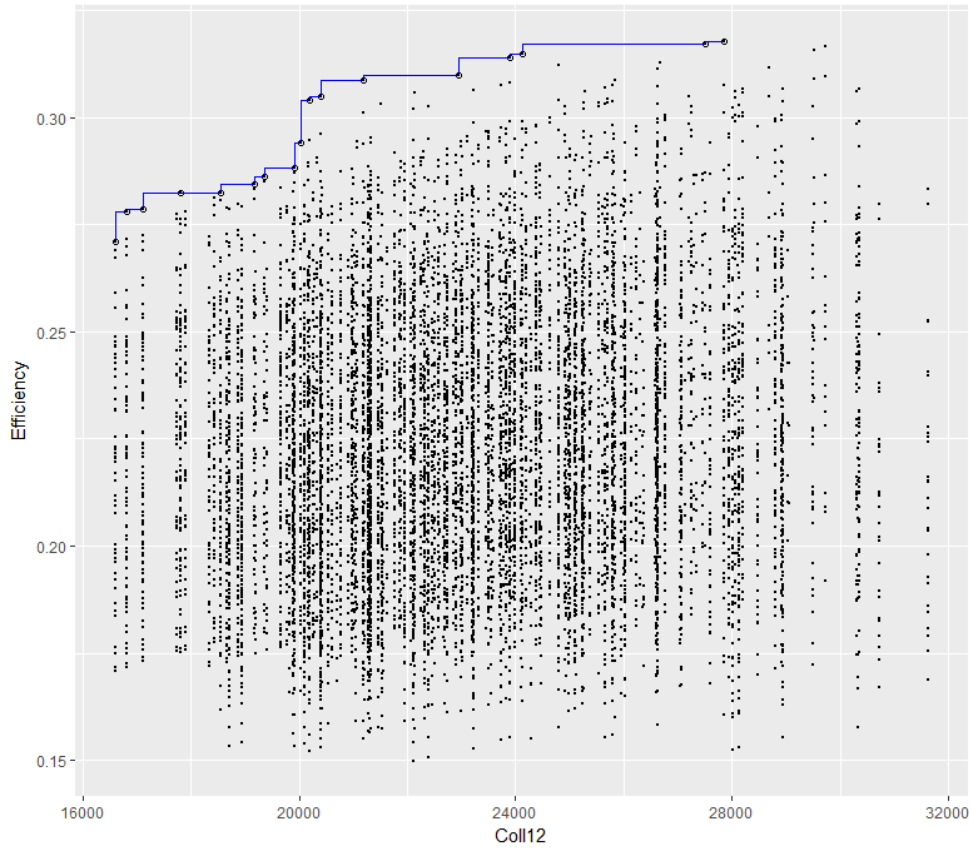
Figure 3.50 A sample of Pareto front (in blue) in the port placement problem

The black points in Figure 3.50 are the X vector; that is the vector of the ports' location on the abdominal surface. The goal was identified as maximizing the efficiency index and minimizing the collision between ArmNo1 and ArmNo2 (Coll12).

3.6 Chapter Summary

In this chapter we described our comprehensive solution to the port placement problem in robotic

laparoscopic procedures. We focused on the hysterectomy procedure where the target organs are the uterus and the ovaries inside the patient's body. We presented a novel methodology for making a patient-specific 3D model, using a 3D scanner (Kinect) for imaging the external shape of the abdomen from the inflated abdomen in the operating room. The target organ's shape and location inside the patient-specific model was determined by superimposing the patient-specific model on an internal model (constructed from pre-operative CT scans of the patient). Also, the target organ's shifts in the internal model (due to insufflation) were measured by an animal study (four sows).

We simulated docking the robot on the patient model by using a robot (da Vinci Si) model. Then we solved the inverse kinematics (IK) equations for finding the robot manipulators' accessible points on the patient-specific model. Finally, we selected preliminary points on the patient model that were accessible and with a manipulability index greeter than a set threshold. We optimized the ports' location by minimizing the collision between the surgical tools and maximizing an efficiency index. The efficiency index was defined as the ratio of the volume of manipulation to the field of view of the endoscope arm.

Chapter 4

Measurements and Results

4.1 Subjects and Experimental Set-up

In this chapter we use our comprehensive solution that is presented in Chapter 3 to find the optimal locations of the ports on the patients who underwent robotic hysterectomy procedures (*da Vinci Si* was used for the simulation). The patients were scanned with a CT scanner (in a supine position) before the operation. The distance between the 2D slices and the acquisition matrices' sizes is shown in Table 4.1. The orientation of the images for all patients was RAI (the letters RAI stands for Right to left, Anterior to posterior, and Inferior to superior respectively). For the rest of this chapter, the Y axis is along the posterior to anterior direction, the Z axis represents the inferior to superior direction, and the X axis is from the left to the right of the patients' body.

To create the external model of the patients, a Kinect camera was mounted above the patients as shown in Figure 3.2. CO_2 gas was used for the insufflation with a pressure of 14 mmHg that remained constant during the scanning of the abdomen by the Kinect camera in the operating room (the trocar was connected to a CO_2 tube to balance the abdominal pressure at 14 mmHg during scanning).

The internal model for each of the patients in Table 4.1 is constructed by using the procedure described in section 3.1.2.

Table 4.1 Patient image information

Patient Label	Sex	Age	Weight (Kg)	Head-Body size (m)	Number of Slices	Acquisition Matrix	Voxel Spacing(mm) (x,y,z)
Patient 1	F	59	58	1.65	562	512×512	0.68×0.68×1
Patient 2	F	48	55	1.63	319	512×512	0.61×0.61×1.25
Patient 3	F	63	70	1.71	426	512×512	0.97×0.97×2
Patient 4	F	70	63	1.68	249	512×512	0.62×0.62×2.5
Patient 5	F	45	53	1.67	209	512×512	0.68×0.68×3
Patient 6	F	63	62	1.54	73	512×512	1.71×1.71×5
Patient 7	F	73	72	1.60	281	512×512	0.91×0.91×1.5

Finally, the patient-specific models of the subjects in Table 4.1 were formed after aligning the external and the internal models (see section 3.1.3). We chose the first four patients for finding the optimal location of the ports since the quality of the generated meshes (the patient model) was better in compare to he other patients.

The robot models were constructed based on the D-H convention, and docking the robot manipulators on the patients' models was simulated in different distances relative to the patients' models. To calculate the accessible points on the patients' models, we defined a reference frame that is attached to the patients' body (model), as shown in Figure 4.1.
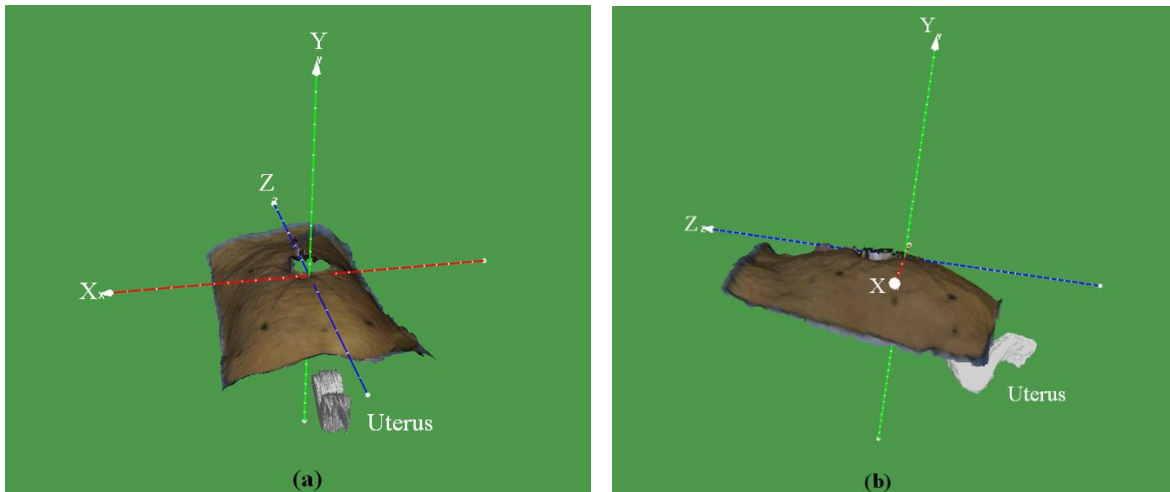
Figure 4.1 The reference frame (attached to the patient's body, and centered at the umbilicus)

Z axis: from legs to the head, X: from left to the right, Y: from back to front

(a): front view (b) side view

The same direction of the axes in the reference frame were selected as in the internal model: Z is along the direction from the patients' legs to the head, and X axis is from the patients left to the right. The center of the coordinate system is located on the umbilicus for all patients.

4.2   Robot Positioning and Port Placement

To find the optimal locations of the ports, we simulated docking the robot (*da Vinci Si*) on the patients, and found the position of the actuated (active) joints in the reference frame. This procedure starts with determining the positions of the first active joints of the manipulators ("A", "B", "C", and "D" positions in Figure 3.30) in the reference frame (when we use "the position of the manipulator" in the rest of this chapter, we mean the position of the first active joint in the manipulators).

For a given position of the manipulators, the accessible points on the patient model are found through the inverse kinematics equation (equation (3.19)). We used MATLAB to solve the inverse kinematic (IK) problem for each of the manipulators. The number of the IK equations for each of the manipulator depends on the number of 3D points on the patients' model. The number of the points in the patient models of the subjects (in Table 4.1) are shown in Table 4.2. For example, for Patient6 we need to solve 69380 IK equations for each of the manipulators.

Table 4.2 Patient information

Patient Label	Number of 3D Points	Number of 3D Points (after simplification)
Patient 1	80871	1008
Patient 2	69226	851
Patient 3	13432	947
Patient 4	12901	922
Patient 5	11322	930
Patient 6	69380	873
Patient 7	147930	893

A huge number of the 3D points in a patient model increases the cost of computation in the machine's processor for solving the IK equations. For example, MATLAB takes about 1.81 seconds to compute the manipulators angles for a given position of the end-effector on the patient model (microprocessor: intel Core-i5). Thus, the computation time for each of the manipulators in Patient6 3D model is about $69380 \times 1.81 = 125577.8$ seconds, or 34.88 hours. As a result, the process time for all four manipulators (endoscope, arm1, arm2, and arm3) equals $34.88 \times 4 = 139.52$ hours.

4.2.1   Mesh Simplification

For solving the IK problem, we can reduce the process time by simplifying the generated patient models (meshes) in Table 4.2. The average distance between the adjacent points in the patient models is about 2.3 mm. Since the diameter of trocars (the most commonly used in robotic surgery) is in the range between 5mm-15mm (size), we can simplify the meshes to eliminate the points that are very close in the meshes.

We used MeshLab software to simplify the patient models by using the clustering decimation method [89]. The clustering decimation algorithm collapses the number of vertices by creating a 3D grid, enveloping the mesh (patient model), and discretizing the vertices based on the cells of the grid. A sample of the simplified vertices in a patient 3D model (Patient3) is shown in Figure 4.2.

(a)   (b)
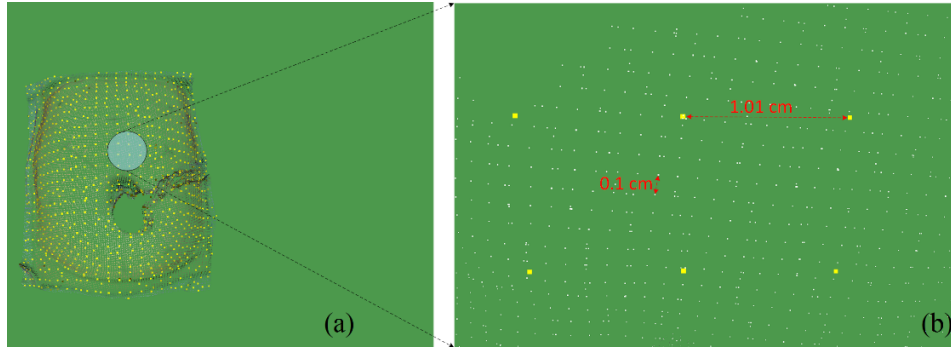
Figure 4.2 (a) A patient model (Patient3), simplified by the clustering decimation method
(b) magnified view of the simplified patient model (Patient3)

The original mesh in Figure 4.2 (b) is shown as the small dots in white, and the simplified mesh is shown as the bold points in yellow. The distance between adjacent points in the original mesh is about 1 mm, and is about 1 cm (10 mm) in the simplified mesh.

4.2.2   Robot Positioning

To find the optimal position of the robot arms relative to the patients, we need to assess and compare the performance of the robot manipulators in different positions in the reference frame.
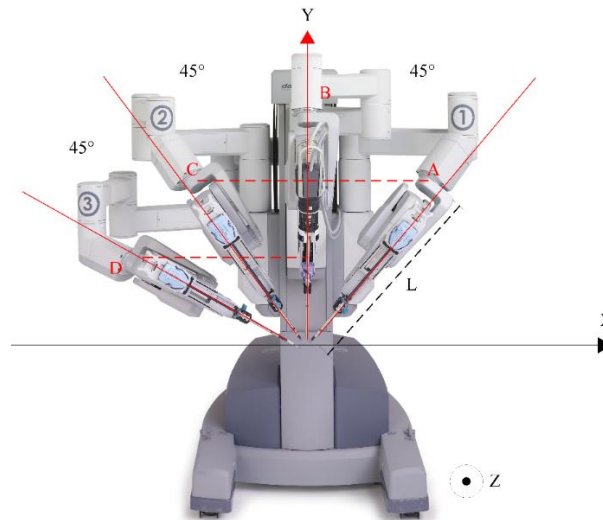
Figure 4.3 The angles between the robot arms for avoiding collision in da *Vinci Si model*, recommended by the manufacturer (Intuitive) [2]

To avoid external collision (outside the patients) between the robot manipulators we used the manufacturer's recommendations to determine the horizontal distance between the robot manipulators as shown in Figure 4.3. The angle between the endoscope (B position) and ArmNo1 (A position) must be at least 45°. Also, the angle between the endoscope and ArmNo2 should be 45°, and the angle between ArmNo2 (position C) and arm No3 (position D) must be 45° to prevent collision between the arms.

We can approximate the minimum horizontal distance between the arms (along the "X" axis in the reference frame) for preventing external collisions by using the recommended angles in the X-Y plane:

$$X_A = L \times \sin(45), \quad X_C = L \times \sin(45), \quad X_D = L \times \sin(90) \tag{4.40}$$

in which X_A, X_C, and X_D are the "X" coordinate of the first active joints in ArmNo1, ArmNo2, and ArmNo3 respectively. "L" is the length of the actuated joints that is same for all robot arms. In the above equation we assumed that the endoscope arm is positioned in the Y-Z plane along the mid line of the patients' body (it is the recommended position of the endoscope in hysterectomy procedures). We measured "L" in the operating room manually, L=0.65 m when the joint angles are zero. As a result, we will obtain X_A=0.4596 m, X_C= 0.4596 m, and X_D= 0.65 m from equation (4.1). Now, we can find the optimal position of the manipulators and the endoscope arm in "Y" and "Z" directions for the first four patients in Table 4.1:

Patient1:

The patient model and the reference frame (coordinate system) are shown in Figure 4.4. The number of accessible points and the average of the manipulability index for Patient1 are shown in Table 4.3.
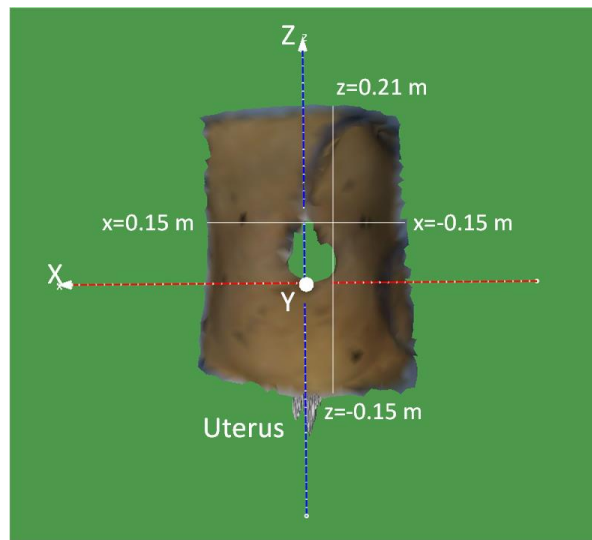
Figure 4.4 Patient1: -0.15 < z < 0.21 and -0.15 < x < 0.15

Table 4.3 Patient1, number of accessible points for the endoscope arm in different positions:
x= 0.0, 0.1 < y < 0.90, z=0.0

Endoscope Position			Number of accessible points	Average of the manipulability index
X (m)	Y (m)	Z (m)		
0.00	0.3	0.00	119	0.080504
0.00	0.35	0.00	222	0.071999
0.00	0.4	0.00	413	0.069685
0.00	0.45	0.00	525	0.082927
0.00	0.5	0.00	525	0.111749
0.00	0.55	0.00	525	0.14122
0.00	0.6	0.00	525	0.166539
0.00	0.65	0.00	525	0.185884
0.00	0.7	0.00	525	0.197547
0.00	0.75	0.00	525	0.197922
0.00	0.8	0.00	524	0.183885
0.00	0.85	0.00	499	0.154402
0.00	0.9	0.00	261	0.124962
0.00	0.95	0.00	6	0.0926

From the above table, we can see that there is no accessible point for the "Y" position of the endoscope arm less than 30 cm or greater than 95 cm.
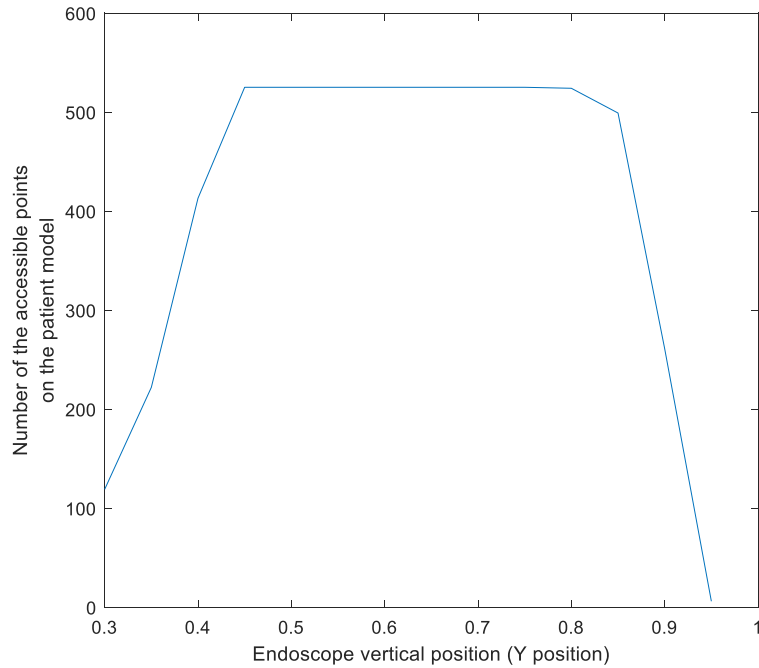
Figure 4.5 Relationship between the endoscope position in Y direction and the number of accessible points on the patient model (Patient1).
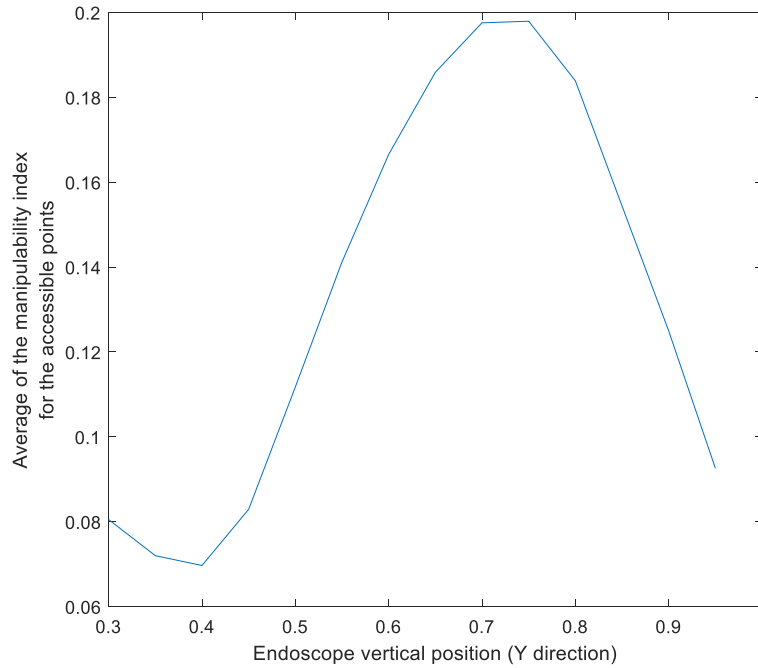
Figure 4.6 Relationship between the endoscope position in Y direction and the average of the manipulability index on the patient model (Patient1).

In Table 4.2 the maximum number of accessible points is 525; this belongs to the position of the endoscope at (X=0.0, $0.45 \leq Y \leq 0.75$, and Z=0.0). We calculated the average of the manipulability index for the accessible points in each position of the endoscope arm (see equation (3.28)). The maximum value of the manipulability index is 0.197922 (highlighted in Table 4.2) when the endoscope arm is positioned at ((X=0.0, Y=0.75, and Z=0.0). The number of accessible points in different positions of the endoscope in the Y direction is shown in Figure 4.5, whereas Figure 4.6 shows the average of the manipulability index for each position of the endoscope in the Y direction.

We can decide about the optimal location of the endoscope arm in the Y direction either based on the number of available points in the patient model or based on the average of the manipulability index. However, if we want to take both into account, we can use Pareto front optimization (see section 2.3.2) with these two objectives for finding the optimal height of the endoscope arm. The Pareto front of these two objectives—the "Number of accessible points" and "Average of manipulability index" in Table 4.2—is just a point (X=0.0, Y = 0.75, and Z=0.0) that is demonstrated in blue in Figure 4.7.
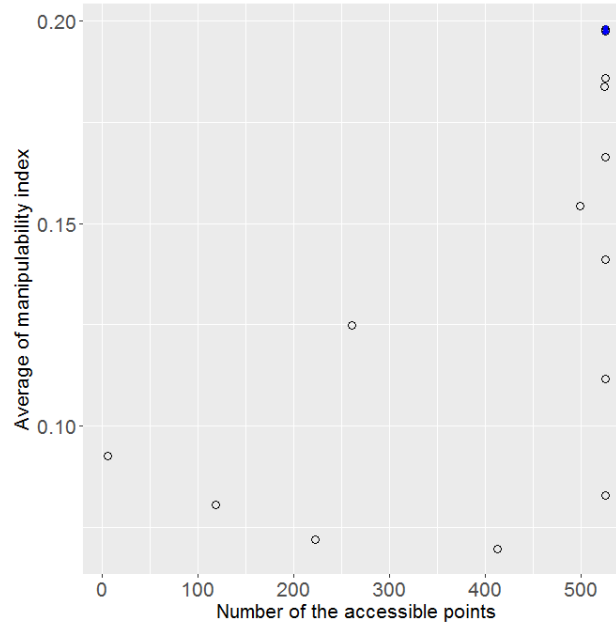
Figure 4.7 Patient1-Pareto front of the endoscope arm, positioned at x= 0.0, 0.1 < y < 0.95, z=0.0.

This means that the optimal position of the endoscope (along the Y axis) is located at 0.75m above the patient's umbilicus. We selected y=0.75 m as the optimal location of the endoscope in the Y direction (we highlighted the optimal position in Table 4.3). For finding the optimal position of the endoscope in the Z direction, we positioned the endoscope in the range of $-0.30 \leq z \leq 0.20$. The results of the accessible points with y=0.75 m and of $-0.30 \leq z \leq 0.20$ are shown in Table 4.4. The maximum number of accessible points is 525, which belongs to $-0.25 \leq z \leq 0.0$. The maximum of the average of the manipulability index is 0.204673, which belongs to z=-0.15. Similar to the Y direction, if we use the Pareto front optimization with two goals (number of accessible points and average of the manipulability index), we will find the optimal positions of the endoscope in the Z direction as z=-0.15m. The result of the Pareto front in the Z direction is shown in Figure 4.8.

Table 4.4 Patient1, Number of accessible points for the endoscope arm in different positions in Z direction: x= 0.0, y=0.75, -0.30 < z < 0.20

Endoscope Position			Number of accessible points	Average of the manipulability index
X (m)	Y (m)	Z (m)		
0.00	0.75	-0.30	499	0.198359
0.00	0.75	-0.25	525	0.199308
0.00	0.75	-0.20	525	0.204729
0.00	0.75	-0.15	525	0.204673
0.00	0.75	-0.10	525	0.202175
0.00	0.75	-0.05	525	0.197922
0.00	0.75	0.00	525	0.191561
0.00	0.75	0.05	523	0.182515
0.00	0.75	0.10	509	0.172761
0.00	0.75	0.15	477	0.162807
0.00	0.75	0.20	425	0.154455
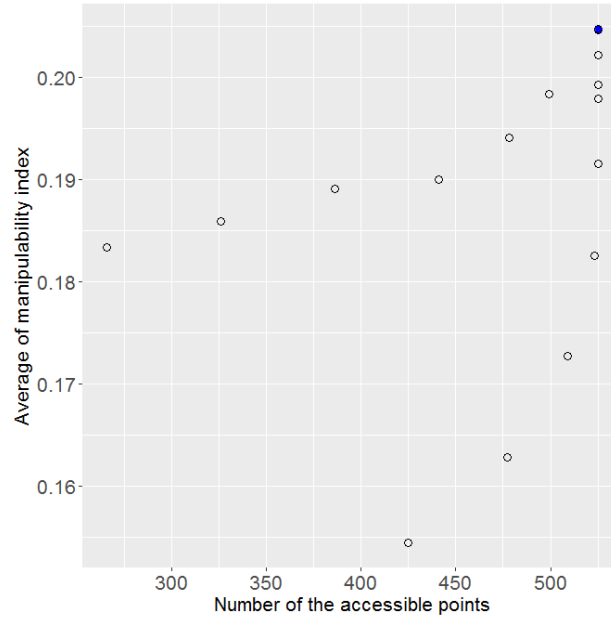
Figure 4.8 Patient1-Pareto front of the endoscope arm, positioned at x= 0.0, y=0.75, -0.3 < z < 0.20.
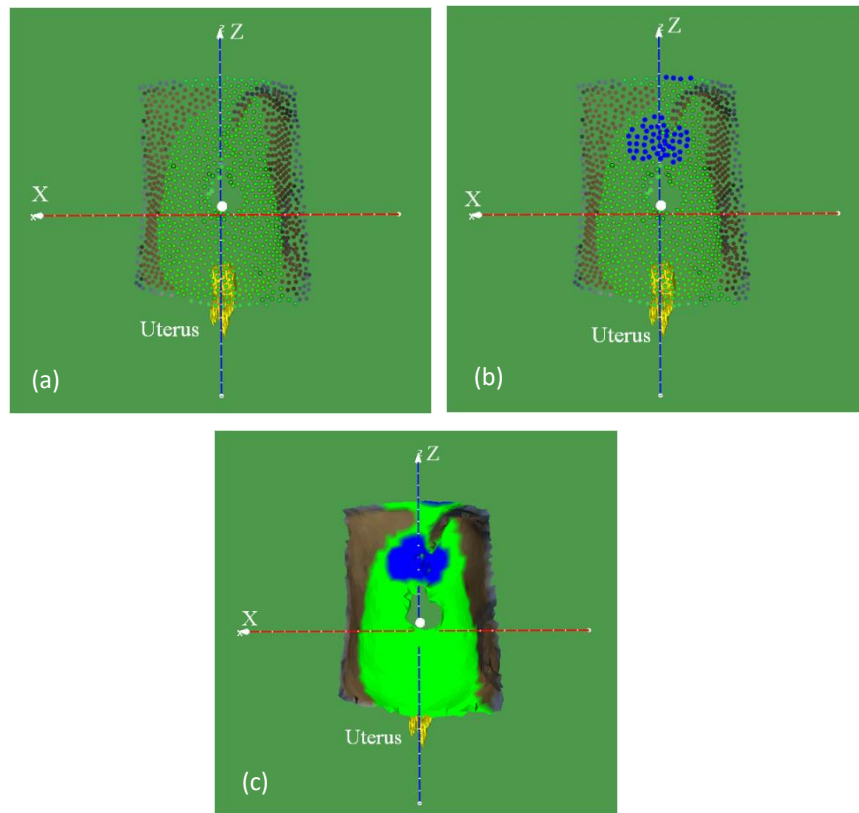
Figure 4.9 (a) accessible points (in green) on the patient model for the endoscope arm, positioned at (0.0, 0.75, -0.15) (b) accessible points with manipulability index > 0.2 (in blue) for the endoscope (c) patient model, accessible points are in green, and the accessible points with manipulability index > 0.2 are in blue

Form the Pareto fronts in Figure 4.7 and Figure 4.8, the optimal position of the endoscope for Patient1 is (x=0.0, y=0.75, z=-0.15). The accessible points on the patient model for the endoscope, positioned at (x=0.0, y=0.75, z=-0.15), are highlighted in green and shown in Figure 4.9.

The total number of accessible points in Figure 4.9 is 525 (see Table 4.3). The accessible points with a manipulability index greater than the threshold (0.204 for the endoscope position x=0.0, y=0.75, z=-0.15) are shown in blue in Figure 4.9.

We used a similar procedure for finding the optimal position of ArmNo1, ArmNo2, and ArmNo3. Tables 4.5, 4.6, and 4.7 show the total number of the accessible points in different Y-positions of ArmNo1, ArmNo2, and ArmNo3 respectively.

Table 4.5 Patient1, number of accessible points for ArmNo1 in different positions:
x= 0.46, 0.10 ≤ y ≤ 0.85, z=0.0

ArmNo1 Position			Number of accessible points	Average of the manipulability index
X (m)	Y (m)	Z (m)		
0.46	0.15	0.00	50	0.134924
0.46	0.20	0.00	249	0.138026
0.46	0.25	0.00	364	0.150586
0.46	0.30	0.00	471	0.158046
0.46	0.35	0.00	505	0.163559
0.46	0.40	0.00	492	0.16743
0.46	0.45	0.00	472	0.168515
0.46	0.50	0.00	444	0.16582
0.46	0.55	0.00	403	0.158617
0.46	0.60	0.00	332	0.150633
0.46	0.65	0.00	232	0.139372
0.46	0.70	0.00	58	0.122845

Table 4.6 Patient1, Number of accessible points for ArmNo2 in different positions:
x= -0.46, 0.10 ≤ y ≤ 0.85, z=0.0

ArmNo2 Position			Number of accessible points	Average of the manipulability index
X (m)	Y (m)	Z (m)		
-0.46	0.15	0.00	40	0.125478
-0.46	0.20	0.00	239	0.136398
-0.46	0.25	0.00	367	0.14896
-0.46	0.30	0.00	485	0.155952
-0.46	0.35	0.00	515	0.162001
-0.46	0.40	0.00	499	0.166389
-0.46	0.45	0.00	479	0.168409
-0.46	0.50	0.00	452	0.16622
-0.46	0.55	0.00	410	0.161712
-0.46	0.60	0.00	351	0.151626
-0.46	0.65	0.00	239	0.13764
-0.46	0.70	0.00	57	0.122562

Table 4.7 Patient1, Number of accessible points for ArmNo3 in different positions:
$x = -0.65, 0.00 \le y \le 0.85, z=0.0$

ArmNo3 Position			Number of accessible points	Average of the manipulability index
X (m)	Y (m)	Z (m)		
-0.65	0.00	0.00	530	0.148852
-0.65	0.05	0.00	533	0.151069
-0.65	0.10	0.00	528	0.153136
-0.65	0.15	0.00	517	0.154335
-0.65	0.20	0.00	501	0.153912
-0.65	0.25	0.00	461	0.153388
-0.65	0.30	0.00	410	0.149613
-0.65	0.35	0.00	311	0.139683
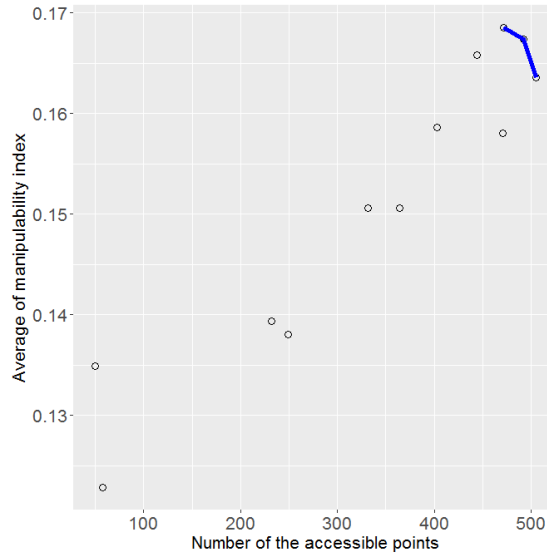
Figure 4.10 Patient1-Pareto front of ArmNo1, positioned at $x = 0.46, 0.15 < y < 0.70, z=0.0.$
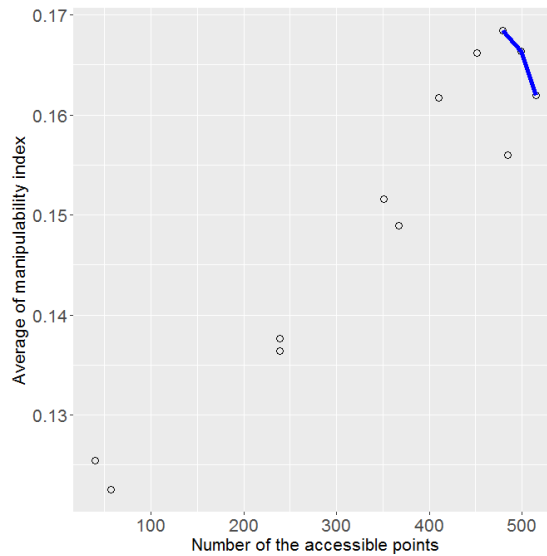
Figure 4.11 Patient1-Pareto front of ArmNo2, positioned at $x = -0.46, 0.15 < y < 0.70, z=0.0.$

87
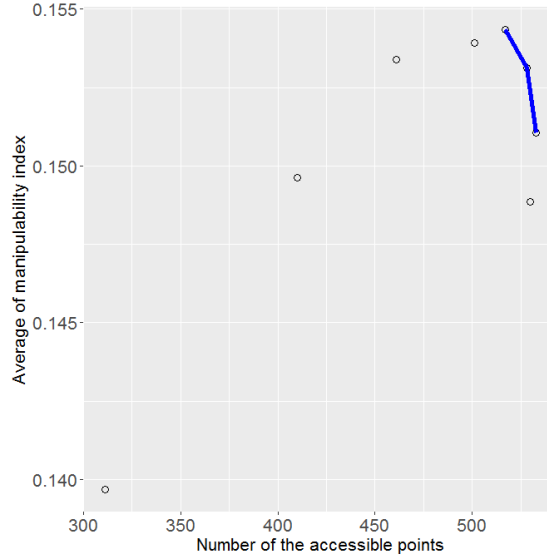
Figure 4.12 Patient1-Pareto front of ArmNo3, positioned at x= -0.65, 0.0 < y < 0.40, z=0.0.

In Table 4.4 and 4.5, when y is greater than 0.7 m or when y is less than 0.15 m, there is no accessible points on the patient model for ArmNo1 and ArmNo2. Similarly, in Table 4.6 we can see that there are no accessible points when y>0.35 for ArmNo3.

The Pareto front solutions (for maximizing the numbers of accessible points and the average of the manipulability indices) are shown in Figure 4.10, Figure 4.11, and 4.12 for ArmNo1, ArmNo2 and ArmNo3 respectively. Also, the results of the Pareto optimization (optimal positions) for ArmNo1, ArmNo2 and ArmNo3 are marked in yellow in Table 4.4, 4.5, and 4.6 respectively. Therefore, the optimal position of ArmNo1 in Y direction is $0.35 \leq y \leq 0.45$ m. Similarly, the optimal location of ArmNo2 in the "Y" direction is in the range of $0.35 \leq y \leq 0.45$, and the optimal position of ArmNo3 is in the range $0.05 \leq y \leq 0.15$ m.

Since we have more than one point on the Pareto front of ArmNo1, ArmNo2, and ArmNo3 (highlighted rows in Tables 4.5, 4.6, and 4.7), we can decide about the optimal location of ArmNo2 either based on the "number of accessible points" or the "average of the manipulability index". In this dissertation, we chose the latter as the optimal location of the robot arms, so the optimal positions of ArmNo1, ArmNo2, and ArmNo3 are 0.45 m, 0.45, and 0.15 m respectively.

Having the optimal positions of the robot arms in the Y direction, we can calculate the number of accessible points and the average of the manipulability index in different positions of the arms in the Z direction. Table 4.8, 4.9, and 4.10 demonstrate the results (accessibility and manipulability in different Z positions) for Arm1, Arm2, and Arm3 respectively. In Table 4.8, 4.9, and 4.10, the Pareto front results are highlighted in yellow, so the optimal position of ArmNo1 in the Z direction is in the range of $-0.25 \leq z \leq -0.10$, and the optimal position of ArmNo2 in the Z direction is $-0.20 \leq z \leq 0.0$. Similarly, for ArmNo3 the optimal position in the Z direction is in the range of $-0.25 \leq z \leq -0.15$. The maximum average of the

manipulability for the optimal range of ArmNo1 is 0.1686, which belongs to z=-0.10, so we select this position as the optimal location of ArmNo1 in the Z direction. For same reason we select z=0.0 and z=-0.15 as the optimal position of ArmNo2 and ArmNo3, respectively, in the Z direction.

Table 4.8 Patient1, Number of accessible points for ArmNo1 in different Z positions:
x= 0.46, y=0.45, -0.30 < z < 0.20

ArmNo1 Position			Number of accessible points	Average of the manipulability index
X (m)	Y (m)	Z (m)		
0.46	0.45	-0.30	516	0.162313
0.46	0.45	-0.25	522	0.165669
0.46	0.45	-0.20	521	0.167302
0.46	0.45	-0.15	515	0.167914
0.46	0.45	-0.10	504	0.168693
0.46	0.45	-0.05	491	0.168371
0.46	0.45	0.00	472	0.168515
0.46	0.45	0.05	447	0.16817
0.46	0.45	0.10	416	0.166089
0.46	0.45	0.15	375	0.162007
0.46	0.45	0.20	320	0.157183

Table 4.9 Patient1, Number of accessible points for ArmNo2 in different Z positions:
x= -0.46, y=0.45, -0.30 < z < 0.20

ArmNo2 Position			Number of accessible points	Average of the manipulability index
X (m)	Y (m)	Z (m)		
-0.46	0.45	-0.30	522	0.163824
-0.46	0.45	-0.25	525	0.165963
-0.46	0.45	-0.20	525	0.167786
-0.46	0.45	-0.15	523	0.167889
-0.46	0.45	-0.10	513	0.167976
-0.46	0.45	-0.05	498	0.16824
-0.46	0.45	0.00	479	0.168409
-0.46	0.45	0.05	455	0.167565
-0.46	0.45	0.10	424	0.1654
-0.46	0.45	0.15	379	0.160971
-0.46	0.45	0.20	318	0.156435

Table 4.10 Patient1, Number of accessible points for ArmNo3 in different Z positions:
x= -0.65, y=0.15, -0.30 < z < 0.20

ArmNo3 Position			Number of accessible points	Average of the manipulability index
X (m)	Y (m)	Z (m)		
-0.65	0.15	-0.35	621	0.186278
-0.65	0.15	-0.30	639	0.186953
-0.65	0.15	-0.25	640	0.187662
-0.65	0.15	-0.20	638	0.18897
-0.65	0.15	-0.15	625	0.189485
-0.65	0.15	-0.10	601	0.189408
-0.65	0.15	-0.05	567	0.189391
-0.65	0.15	0.00	533	0.189403
-0.65	0.15	0.05	494	0.189356
-0.65	0.15	0.10	431	0.189005
-0.65	0.15	0.15	363	0.18699
-0.65	0.15	0.20	282	0.184586
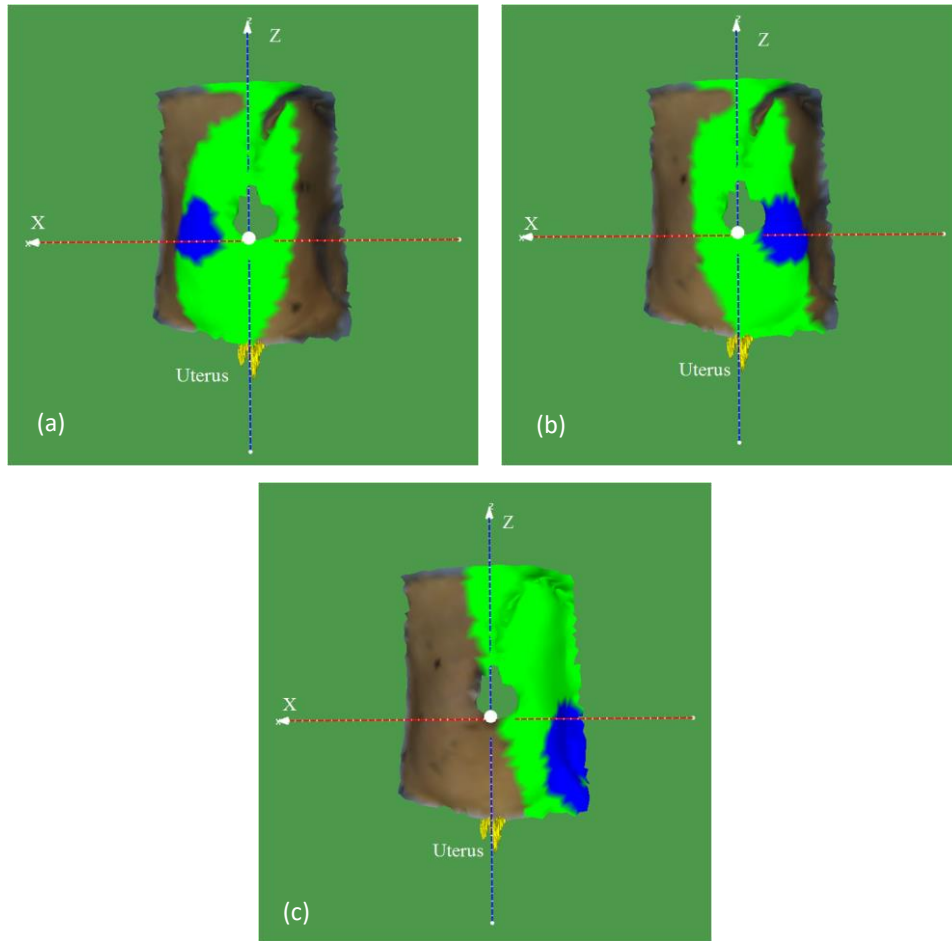
Figure 4.13 (a) accessible points (in green) on the patient model for ArmNo1, positioned at (0.46, 0.45, -0.10). The accessible points with manipulability index > 0.1687 are shown in blue

(b) accessible points (in green) on the patient model for ArmNo2, positioned at (-0.46, 0.45, 0.0). The accessible points with manipulability index > 0.1684 are shown in blue

(c) accessible points (in green) on the patient model for ArmNo3, positioned at (-0.65, 0.15, -0.15). The accessible points with manipulability index > 0.1894 are shown in blue

To sum up, the optimal positions of ArmNo1, ArmNo2, and ArmNo3 are (0.46, 0.45, -0.10), (-0.46, 0.45, 0.00), and (-0.65, 0.15, -0.15) respectively. The accessible points on the patient model for the optimal position of ArmNo1, ArmNo2, and ArmNo3 are shown in Figure 4.13. Also, the preliminary points—the points with a manipulability index greater than the threshold (average + standard deviation of the manipulability indices)—for each of the arms are shown in blue as depicted in Figure 4.13.

Patient2:

The number of accessible points and the average of the manipulability index for the endoscope are shown in Table 4.11.

Table 4.11 Patient2, number of accessible points for the endoscope arm in different positions:
x= 0.0, 0.1 < y < 0.95, z=0.0

Endoscope Position			Number of accessible points	Average of the manipulability index
X (m)	Y (m)	Z (m)		
0.00	0.3	0.00	82	0.098281427
0.00	0.35	0.00	186	0.086308527
0.00	0.4	0.00	353	0.089070113
0.00	0.45	0.00	490	0.102362931
0.00	0.5	0.00	490	0.129779539
0.00	0.55	0.00	490	0.156221602
0.00	0.6	0.00	490	0.178101967
0.00	0.65	0.00	490	0.194195692
0.00	0.7	0.00	490	0.203719178
0.00	0.75	0.00	490	0.205354288
0.00	0.8	0.00	490	0.196640931
0.00	0.85	0.00	474	0.17405047
0.00	0.9	0.00	266	0.149823173
0.00	0.95	0.00	21	0.109846048

From the above table, we can see that there is no accessible point for the Y-position of the endoscope arm that is less than 30 cm or greater than 90 cm. The result of the Pareto front is highlighted in Table 4.10, so the optimal position of the endoscope in the Y direction is y=0.75 m. Considering the endoscope's optimal position in the Y direction, the results of the number of accessible points and the average of the manipulability index in different positions of the endoscope in the Z direction are represented in Table 4.12.

Table 4.12 Patient2, Number of accessible points for the endoscope arm in different positions in the Z direction:
x= 0.0, y=0.75, -0.30 < z < 0.20

Endoscope Position			Number of accessible points	Average of the manipulability index
X (m)	Y (m)	Z (m)		
0.00	0.75	-0.30	453	0.213611408
0.00	0.75	-0.25	487	0.213427809
0.00	0.75	-0.20	490	0.214715771
0.00	0.75	-0.15	490	0.213842992
0.00	0.75	-0.10	490	0.211657459
0.00	0.75	-0.05	490	0.208767465
0.00	0.75	0.00	490	0.205354288
0.00	0.75	0.05	490	0.201229418
0.00	0.75	0.10	488	0.196077316
0.00	0.75	0.15	483	0.189202892
0.00	0.75	0.20	453	0.183489247

From Table 4.12, the optimal position of the endoscope in Z direction is z=-0.20 m, so the optimal position of the endoscope is (0.0, 0.75, -0.20).

Similar to the endoscope, the results of the number of accessible points and the average of the manipulability index (in Y direction) for ArmNo1, ArmNo2, and ArmNo3 are shown in Table 4.13, 4.14, and 4.15 respectively.

Table 4.13 Patient2, number of accessible points for ArmNo1 in different positions in the Y direction: x= 0.46, 0.10 ≤ y ≤ 0.85, z=0.0

ArmNo1 Position			Number of accessible points	Average of the manipulability index
X (m)	Y (m)	Z (m)		
0.46	0.20	0.00	151	0.145892066
0.46	0.25	0.00	325	0.160385065
0.46	0.35	0.00	454	0.170026899
0.46	0.35	0.00	479	0.175432246
0.46	0.40	0.00	467	0.178901792
0.46	0.45	0.00	443	0.180805804
0.46	0.50	0.00	404	0.181185297
0.46	0.55	0.00	361	0.177713753
0.46	0.60	0.00	302	0.169702189
0.46	0.65	0.00	215	0.159408135
0.46	0.70	0.00	98	0.140199561

Table 4.14 Patient2, Number of accessible points for ArmNo2 in different positions: x= -0.46, 0.10 ≤ y ≤ 0.85, z=0.0

ArmNo2 Position			Number of accessible points	Average of the manipulability index
X (m)	Y (m)	Z (m)		
-0.46	0.20	0.00	111	0.139493658
-0.46	0.25	0.00	321	0.154693997
-0.46	0.30	0.00	465	0.166841875
-0.46	0.35	0.00	488	0.172975836
-0.46	0.40	0.00	475	0.177750512
-0.46	0.45	0.00	455	0.180702367
-0.46	0.50	0.00	425	0.181472471
-0.46	0.55	0.00	379	0.179918604
-0.46	0.60	0.00	328	0.173295796
-0.46	0.65	0.00	247	0.162151765
-0.46	0.70	0.00	128	0.1436465

Table 4.15 Patient2, Number of accessible points for ArmNo3 in different positions: x= -0.65, 0.00 ≤ y ≤ 0.85, z=0.0

ArmNo3 Position			Number of accessible points	Average of the manipulability index
X (m)	Y (m)	Z (m)		
-0.65	0.00	0.00	390	0.16649651
-0.65	0.05	0.00	394	0.168685365
-0.65	0.10	0.00	393	0.170625511
-0.65	0.15	0.00	383	0.172383131
-0.65	0.20	0.00	370	0.172549843
-0.65	0.25	0.00	349	0.170995808
-0.65	0.30	0.00	315	0.167082368
-0.65	0.35	0.00	265	0.159178721

From Tables 4.13 and Table 4.14, there are no accessible points on the patient model for ArmNo1 and ArmNo2 when y<0.2 m or y>0.70 m. Also, from Table 4.15, there is no accessible point for ArmNo3 when

y>0.35. The optimal position of ArmNo1 and ArmNo2 is in the range between 0.35 m< y < 0.50 m. Similarly, the optimal position of ArmNo3 is in the range 0.05 m< y < 0.20. If we choose the points with the highest manipulability index in Tables 4.12, 4.13, and 4.14, the optimal positions of ArmNo1 and ArmNo2 is 0.50 m, and the optimal position of ArmNo3 is 0.20 cm.

Considering the optimal positions of the robot arms in the Y direction, we can calculate the number of accessible points and the average of the manipulability index in different positions of the arms in the Z direction. Tables 4.16, 4.17, and 4.18 demonstrate the results (accessibility and manipulability in different Z positions) for Arm1, Arm2, and Arm3 respectively. In Tables 4.16, 4.17, and 4.18, the Pareto front results are highlighted in yellow, so the optimal position of ArmNo1 and ArmNo2 in Z direction is in the range of $-0.30 \leq z \leq -0.20$. Similarly, for ArmNo3 the optimal range of position in Z direction is $-0.25 \leq z \leq -0.05$. The maximum average manipulability index for the optimal range of ArmNo1 is 0.187, which belongs to z=-0.30, so we select this position as the optimal location of ArmNo1 in the Z direction. For the same reason we select z=-0.30 as the optimal position of ArmNo2, and z=-0.05 ArmNo3 in the Z direction.

Table 4.16 Patient2, Number of accessible points for ArmNo1 in different Z positions:
x= 0.46, y=0.50, -0.30 < z < 0.20

ArmNo1 Position			Number of accessible points	Average of the manipulability index
X (m)	Y (m)	Z (m)		
0.46	0.50	-0.30	433	0.187052672
0.46	0.50	-0.25	443	0.186669573
0.46	0.50	-0.20	453	0.185057177
0.46	0.50	-0.15	447	0.184666347
0.46	0.50	-0.10	444	0.183037032
0.46	0.50	-0.05	429	0.182049019
0.46	0.50	0.00	404	0.181185297
0.46	0.50	0.05	378	0.178898921
0.46	0.50	0.10	343	0.175764799
0.46	0.50	0.15	291	0.173550357
0.46	0.50	0.20	237	0.169665139

Table 4.17 Patient2, Number of accessible points for ArmNo2 in different Z positions:
x= -0.46, y=0.50, -0.30 < z < 0.20

ArmNo2 Position			Number of accessible points	Average of the manipulability index
X (m)	Y (m)	Z (m)		
-0.46	0.50	-0.30	452	0.188036929
-0.46	0.50	-0.25	466	0.18665582
-0.46	0.50	-0.20	475	0.185010552
-0.46	0.50	-0.15	472	0.1841681
-0.46	0.50	-0.10	463	0.18334641
-0.46	0.50	-0.05	443	0.18292895
-0.46	0.50	0.00	425	0.181472471
-0.46	0.50	0.05	396	0.180063616
-0.46	0.50	0.10	365	0.177242671
-0.46	0.50	0.15	314	0.175206694
-0.46	0.50	0.20	263	0.17164984

Table 4.18 Patient2, Number of accessible points for ArmNo3 in different Z positions:
x= -0.65, y=0.20, -0.30 < z < 0.20

ArmNo3 Position			Number of accessible points	Average of the manipulability index
X (m)	Y (m)	Z (m)		
-0.65	0.20	-0.30	460	0.167682802
-0.65	0.20	-0.25	462	0.168383171
-0.65	0.20	-0.20	459	0.169169161
-0.65	0.20	-0.15	440	0.171001761
-0.65	0.20	-0.10	424	0.171935903
-0.65	0.20	-0.05	399	0.172884218
-0.65	0.20	0.00	370	0.172549843
-0.65	0.20	0.05	328	0.171500979
-0.65	0.20	0.10	280	0.168872836
-0.65	0.20	0.15	222	0.165419486
-0.65	0.20	0.20	153	0.162418458
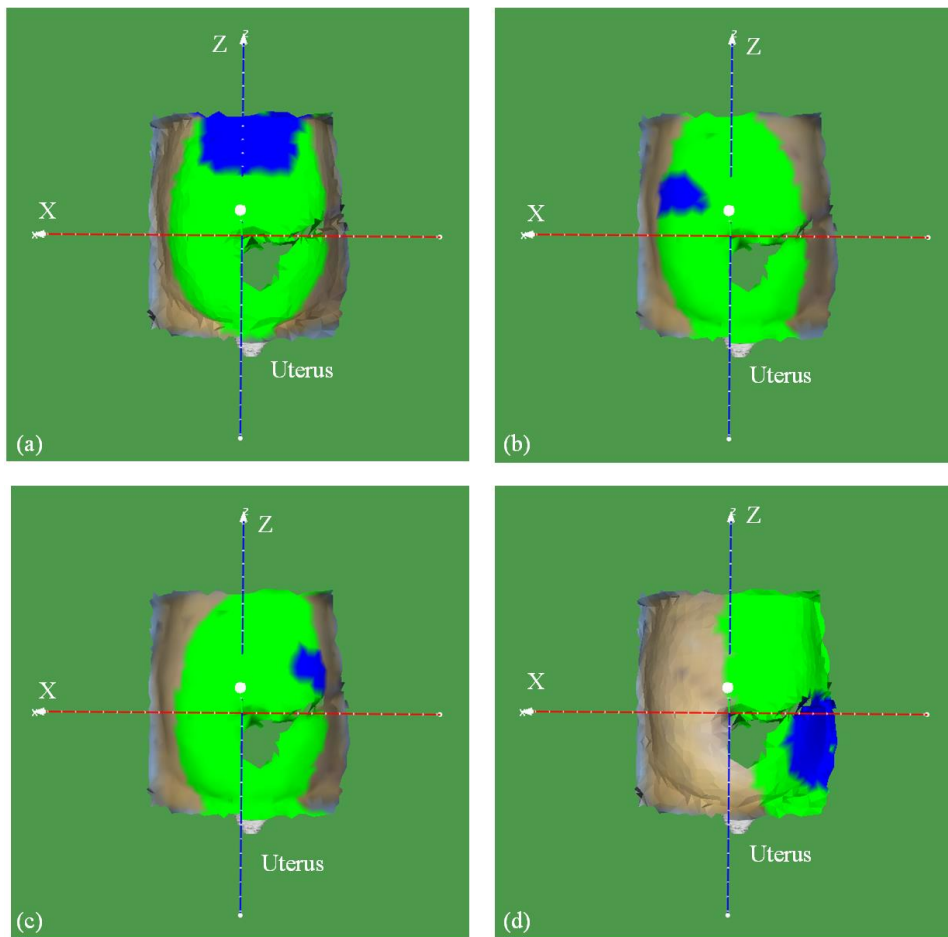
Figure 4.14 Accessible and preliminary points (in green and blue) on the Patient2 model
(a) The endoscope positioned at (0.0, 0.75, -0.20) (b) ArmNo1 positioned at (0.46, 0.50, -0.30) (c) ArmNo2
positioned at (-0.46, 0.50 -0.30) (d) ArmNo3 positioned at (-0.65, 0.20, -0.05)

To sum up, the optimal positions of ArmNo1, ArmNo2, and ArmNo3 are (0.46, 0.50, -0.30), (-0.46, 0.50, -0.30), and (-0.65, 0.20, -0.05) respectively. The accessible points on the patient model for the optimal

position of the endoscope, ArmNo1, ArmNo2, and ArmNo3 are shown in Figure 4.14. Also, the preliminary points—the points with a manipulability index greater than the threshold (average +standard deviation of the manipulability indices)—for each of the arms are shown in blue as depicted in Figure 4.14.

Patient3:

The endoscope accessible points and the average of the manipulability index in Y direction are shown in Table 4.19.

Table 4.19 Patient3, number of accessible points for the endoscope arm in different positions:
x= 0.0, 0.1 < y < 0.95, z=0.0

Endoscope Position			Number of accessible points	Average of the manipulability index
X (m)	Y (m)	Z (m)		
0.00	0.3	0.00	110	0.102855918
0.00	0.35	0.00	214	0.091211855
0.00	0.4	0.00	402	0.090672157
0.00	0.45	0.00	544	0.103490583
0.00	0.5	0.00	545	0.129871844
0.00	0.55	0.00	545	0.155738029
0.00	0.6	0.00	545	0.177265468
0.00	0.65	0.00	545	0.193112413
0.00	0.7	0.00	545	0.202373978
0.00	0.75	0.00	545	0.203720101
0.00	0.8	0.00	545	0.194559222
0.00	0.85	0.00	518	0.172515525
0.00	0.9	0.00	286	0.148993066
0.00	0.95	0.00	30	0.114882133

From Table 4.19, for y>0.95 and y<0.3 no accessible point can be found for the endoscope arm. The only optimal position (obtained by the Pareto front) is highlighted in yellow, and so the optimal position of the endoscope is y=0.75 m. We placed the endoscope in the optimal position (y=0.75 m) and calculated the accessible points and the related average of the manipulability index in Z direction as shown in Table 4.20.

Table 4.20 Patient3, Number of accessible points for the endoscope arm in different positions in the Z direction:
x= 0.0, y=0.75, -0.30 < z < 0.20

Endoscope Position			Number of accessible points	Average of the manipulability index
X (m)	Y (m)	Z (m)		
0.00	0.75	-0.30	529	0.213136248
0.00	0.75	-0.25	545	0.214723969
0.00	0.75	-0.20	545	0.214839472
0.00	0.75	-0.15	545	0.213162714
0.00	0.75	-0.10	545	0.210561314
0.00	0.75	-0.05	545	0.207379363
0.00	0.75	0.00	545	0.203720101
0.00	0.75	0.05	545	0.199219033
0.00	0.75	0.10	543	0.193268061
0.00	0.75	0.15	521	0.187754405
0.00	0.75	0.20	483	0.182027752

In Table 4.20, we highlighted the Pareto-optimal solution in the Z direction as z=-0.20. Therefore, the optimal position of the endoscope is (0.0, 0.75, -0.20).

We performed same procedure for finding the optimal position of ArmNo1, ArmNo2, and ArmNo3. The number of accessible points and the average of the manipulability index for these three arms are shown in Table 4.21, 4.22, and 4.23.

Table 4.21 Patient3, number of accessible points for ArmNo1 in different positions in the Y direction: x= 0.46, 0.10 ≤ y ≤ 0.85, z=0.0

ArmNo1 Position			Number of accessible points	Average of the manipulability index
X (m)	Y (m)	Z (m)		
0.46	0.2	0.00	132	0.139925068
0.46	0.25	0.00	325	0.15569676
0.46	0.3	0.00	497	0.167187429
0.46	0.35	0.00	533	0.173073734
0.46	0.4	0.00	516	0.177092554
0.46	0.45	0.00	481	0.180658048
0.46	0.5	0.00	452	0.180496352
0.46	0.55	0.00	402	0.177932095
0.46	0.6	0.00	335	0.171797325
0.46	0.65	0.00	248	0.160219742
0.46	0.7	0.00	111	0.142568315

Table 4.22 Patient3, Number of accessible points for ArmNo2 in different positions: x= -0.46, 0.10 ≤ y ≤ 0.85, z=0.0

ArmNo2 Position			Number of accessible points	Average of the manipulability index
X (m)	Y (m)	Z (m)		
-0.46	0.20	0.00	162	0.144563204
-0.46	0.25	0.00	336	0.15888092
-0.46	0.30	0.00	492	0.16943524
-0.46	0.35	0.00	530	0.174926319
-0.46	0.40	0.00	513	0.178784435
-0.46	0.45	0.00	489	0.180860945
-0.46	0.50	0.00	453	0.180708627
-0.46	0.55	0.00	402	0.17749901
-0.46	0.60	0.00	334	0.17112132
-0.46	0.65	0.00	250	0.158420336
-0.46	0.70	0.00	120	0.1404269

Table 4.23 Patient3, Number of accessible points for ArmNo3 in different positions: x= -0.65, 0.00 ≤ y ≤ 0.85, z=0.0

ArmNo3 Position			Number of accessible points	Average of the manipulability index
X (m)	Y (m)	Z (m)		
-0.65	0.00	0.00	484	0.17219719
-0.65	0.05	0.00	493	0.173314929
-0.65	0.10	0.00	492	0.174277325
-0.65	0.15	0.00	481	0.174683497
-0.65	0.20	0.00	463	0.173640747
-0.65	0.25	0.00	430	0.170684342
-0.65	0.30	0.00	388	0.16464734
-0.65	0.35	0.00	288	0.156726757
-0.65	0.40	0.00	72	0.150329333

In Table 4.21, 4.22, and 4.23, the Pareto front solutions are highlighted in yellow. Therefore, the optimal position of ArmNo1 and ArmNo2 is in the range $0.35 \le y \le 0.45$. Also, the optimal position of ArmNo3 is in the range $0.05 \le y \le 0.15$. We chose the position with the highest average of manipulability in the optimal ranges, and so the optimal position of ArmNo1 and ArmNo2 is y=0.45. Also, the optimal position of ArmNo3 is y=0.15.

Using the optimal position of ArmNo1, ArmNo2, and ArmNo3, we calculated the number of the accessible points and the average of the manipulability index in the Z direction, as shown in Table 4.24, 4.25, and 4.26.

Table 4.24 Patient3, Number of accessible points for ArmNo1 in different Z positions:
x= 0.46, y=0.45, -0.30 < z < 0.20

ArmNo1 Position			Number of accessible points	Average of the manipulability index
X (m)	Y (m)	Z (m)		
0.46	0.45	-0.30	540	0.186039159
0.46	0.45	-0.25	544	0.184633893
0.46	0.45	-0.20	544	0.183119583
0.46	0.45	-0.15	544	0.181364621
0.46	0.45	-0.10	533	0.180456411
0.46	0.45	-0.05	515	0.180012806
0.46	0.45	0.00	481	0.180658048
0.46	0.45	0.05	453	0.179776185
0.46	0.45	0.10	412	0.178541022
0.46	0.45	0.15	363	0.176728405
0.46	0.45	0.20	301	0.174964678

Table 4.25 Patient3, Number of accessible points for ArmNo2 in different Z positions:
x= -0.46, y=0.45, -0.30 < z < 0.20

ArmNo2 Position			Number of accessible points	Average of the manipulability index
X (m)	Y (m)	Z (m)		
-0.46	0.45	-0.30	540	0.185937385
-0.46	0.45	-0.25	545	0.184839589
-0.46	0.45	-0.20	545	0.183532572
-0.46	0.45	-0.15	541	0.182289126
-0.46	0.45	-0.10	528	0.181772271
-0.46	0.45	-0.05	508	0.18159553
-0.46	0.45	0.00	489	0.180860945
-0.46	0.45	0.05	457	0.180128133
-0.46	0.45	0.10	414	0.17878256
-0.46	0.45	0.15	362	0.17691471
-0.46	0.45	0.20	311	0.1730219

Pareto front results in Table 4.24, 4.25, and 4.26 are highlighted in yellow. Therefore, the optimal positions of ArmNo1 and ArmNo2 in Z direction is in z=-0.30. Also, the optimal position of ArmNo3 in Z direction is z=0.0.

Table 4.26 Patient3, Number of accessible points for ArmNo3 in different Z positions:
x= -0.65, y=0.15, -0.30 < z < 0.20

ArmNo3 Position			Number of accessible points	Average of the manipulability index
X (m)	Y (m)	Z (m)		
-0.65	0.15	-0.30	604	0.170114041
-0.65	0.15	-0.25	606	0.170320807
-0.65	0.15	-0.20	597	0.171186358
-0.65	0.15	-0.15	581	0.172319363
-0.65	0.15	-0.10	553	0.174106315
-0.65	0.15	-0.05	524	0.17463895
-0.65	0.15	0.00	481	0.174683497
-0.65	0.15	0.05	428	0.17329943
-0.65	0.15	0.10	362	0.170931829
-0.65	0.15	0.15	291	0.166692113
-0.65	0.15	0.20	213	0.161590249
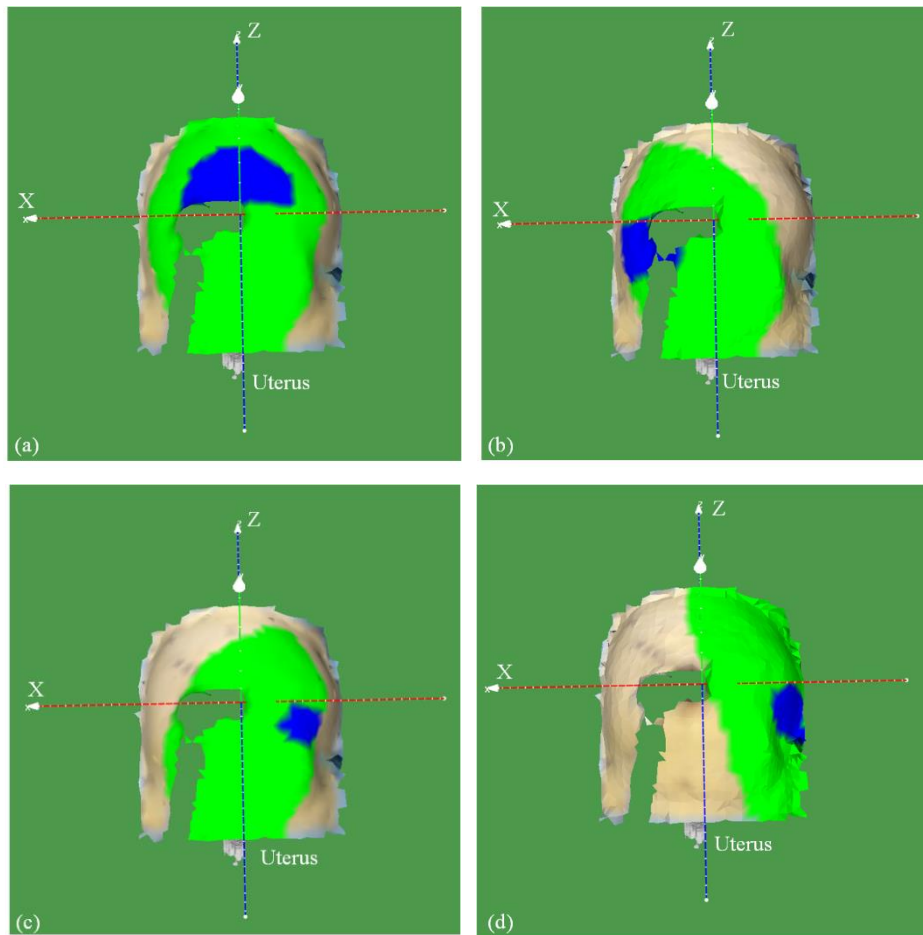
Figure 4.15 Accessible and preliminary points (in green and blue) on the Patient3 model
(a) The endoscope positioned at (0.0, 0.75, -0.20) (b) ArmNo1 positioned at (0.46, 0.45, -0.30) (c) ArmNo2
positioned at (-0.46, 0.45, -0.30) (d) ArmNo3 positioned at (-0.65, 0.15, 0.00)

To sum up, the optimal positions of the endoscope, ArmNo1, ArmNo2 and ArmNo3 are (0.0, 0.75, -0.20), (0.46, 0.45, -0.30), (-0.46, 0.45, -0.30), and (-0.65, 0.15, 0.0) respectively. The accessible and preliminary points for the endoscope and the manipulators are shown in Figure 4.15.

Patient4:

Table 4.27, 4.28, 4.29, and 4.30 show the number of accessible points and the manipulability index for the endoscope, ArmNo1, ArmNo2, and ArmNo3 respectively in the Y direction. The optimal Pareto front results are highlighted in yellow in each of the following tables.

Table 4.27 Patient4, number of accessible points for the endoscope arm in different Y positions: x= 0.0, 0.1 < y < 0.95, z=0.0

Endoscope Position			Number of accessible points	Average of the manipulability index
X (m)	Y (m)	Z (m)		
0.00	0.25	0.00	72	0.110200764
0.00	0.3	0.00	153	0.110865458
0.00	0.35	0.00	229	0.103018266
0.00	0.4	0.00	459	0.093997357
0.00	0.45	0.00	496	0.111403139
0.00	0.5	0.00	496	0.13585198
0.00	0.55	0.00	496	0.159299996
0.00	0.6	0.00	496	0.178861308
0.00	0.65	0.00	496	0.193152508
0.00	0.7	0.00	496	0.201046655
0.00	0.75	0.00	496	0.200975387
0.00	0.8	0.00	493	0.190373708
0.00	0.85	0.00	451	0.169224049
0.00	0.9	0.00	222	0.141126482

Table 4.282 Patient4, number of accessible points for ArmNo1 in different Y positions: x= 0.46, 0.10 ≤ y ≤ 0.85, z=0.0

ArmNo1 Position			Number of accessible points	Average of the manipulability index
X (m)	Y (m)	Z (m)		
0.46	0.15	0.00	1	0.151912
0.46	0.2	0.00	222	0.150161802
0.46	0.25	0.00	344	0.162865901
0.46	0.3	0.00	463	0.172032529
0.46	0.35	0.00	475	0.177031931
0.46	0.4	0.00	465	0.180189265
0.46	0.45	0.00	450	0.181165878
0.46	0.5	0.00	422	0.179561988
0.46	0.55	0.00	379	0.174600873
0.46	0.6	0.00	306	0.1668415
0.46	0.65	0.00	213	0.15200785
0.46	0.70	0.00	4	0.12682275

Table 4.29 Patients4, Number of accessible points for ArmNo2 in different Y positions:
x= -0.46, 0.10 ≤ y ≤ 0.85, z=0.0

ArmNo2 Position			Number of accessible points	Average of the manipulability index
X (m)	Y (m)	Z (m)		
-0.46	0.20	0.00	195	0.155053467
-0.46	0.25	0.00	340	0.166488326
-0.46	0.30	0.00	460	0.173260733
-0.46	0.35	0.00	468	0.177122053
-0.46	0.40	0.00	454	0.179056441
-0.46	0.45	0.00	432	0.178747884
-0.46	0.50	0.00	395	0.175724478
-0.46	0.55	0.00	337	0.169559715
-0.46	0.60	0.00	255	0.160023282
-0.46	0.65	0.00	136	0.144469934

Table 4.30 Patient4, Number of accessible points for ArmNo3 in different Y positions:
x= -0.65, 0.00 ≤ y ≤ 0.85, z=0.0

ArmNo3 Position			Number of accessible points	Average of the manipulability index
X (m)	Y (m)	Z (m)		
-0.65	0.00	0.00	373	0.168353
-0.65	0.05	0.00	374	0.169133
-0.65	0.10	0.00	371	0.169081
-0.65	0.15	0.00	360	0.167795
-0.65	0.20	0.00	335	0.16496
-0.65	0.25	0.00	296	0.159475
-0.65	0.30	0.00	191	0.152766
-0.65	0.35	0.00	46	0.144954

In Table 4.27, the only optimal position of the endoscope is in y=0.7 m. In Table 4.28, the optimal position of ArmNo1 is in the range $0.35 \leq y \leq 0.45$, so we chose y=0.45 m as the optimal location of ArmNo1 because the maximum manipulability index in this range is 0.1811. In Table 4.29, the optimal position of ArmNo2 is in $0.35 \leq y \leq 0.40$, so we chose y=0.4 m as the optimal position with the highest average of the manipulability index. Similar to the endoscope arm, the only optimal position of ArmNo3 is y=0.05 m in Table 4.30.

Having the optimal positions of the arms, we calculated the number of accessible points and the average of the manipulability index in the Z direction; the results are shown in Table 4.31, 4.32, 4.33, and 4.34 for the endoscope, ArmNo1, ArmNo2, and ArmNo3 respectively.

Table 4.31 Patient4, Number of accessible points for the endoscope arm in different positions in the Z direction:
x= 0.0, y=0.70, -0.30 < z < 0.20

Endoscope Position			Number of accessible points	Average of the manipulability index
X (m)	Y (m)	Z (m)		
0.00	0.70	-0.30	496	0.218306008
0.00	0.70	-0.25	496	0.216336548
0.00	0.70	-0.20	496	0.213132915
0.00	0.70	-0.15	496	0.209647794
0.00	0.70	-0.10	496	0.206418601
0.00	0.70	-0.05	496	0.203598907
0.00	0.70	0.00	496	0.201046655
0.00	0.70	0.05	496	0.198239565
0.00	0.70	0.10	496	0.194247
0.00	0.70	0.15	484	0.189362919
0.00	0.70	0.20	454	0.184533068

Table 4.32 Patient4, Number of accessible points for ArmNo1 in different Z positions:
x= 0.46, y=0.45, -0.30 < z < 0.20

ArmNo1 Position			Number of accessible points	Average of the manipulability index
X (m)	Y (m)	Z (m)		
0.46	0.45	-0.30	496	0.187130683
0.46	0.45	-0.25	496	0.185910308
0.46	0.45	-0.20	494	0.184686696
0.46	0.45	-0.15	492	0.183431169
0.46	0.45	-0.10	482	0.182818083
0.46	0.45	-0.05	470	0.182067011
0.46	0.45	0.00	450	0.181165878
0.46	0.45	0.05	421	0.179503665
0.46	0.45	0.10	377	0.177511347
0.46	0.45	0.15	330	0.173868606
0.46	0.45	0.20	274	0.16868258

Table 4.33 Patient4, Number of accessible points for ArmNo2 in different Z positions:
x= -0.46, y=0.40, -0.30 < z < 0.20

ArmNo2 Position				
X (m)	Y (m)	Z (m)	Number of accessible points	Average of the manipulability index
-0.46	0.40	-0.30	496	0.184246411
-0.46	0.40	-0.25	496	0.182877401
-0.46	0.40	-0.20	496	0.181514688
-0.46	0.40	-0.15	496	0.180253365
-0.46	0.40	-0.10	490	0.179529137
-0.46	0.40	-0.05	478	0.179108243
-0.46	0.40	0.00	454	0.179056441
-0.46	0.40	0.05	427	0.177586419
-0.46	0.40	0.10	374	0.17667588
-0.46	0.40	0.15	324	0.174058664
-0.46	0.40	0.20	264	0.170772928

Table 4.34 Patient4, Number of accessible points for ArmNo3 in different Z positions:
x= -0.65, y=0.05, -0.30 < z < 0.20

ArmNo3 Position			Number of accessible points	Average of the manipulability index
X (m)	Y (m)	Z (m)		
-0.65	0.05	-0.30	544	0.159857
-0.65	0.05	-0.25	531	0.161889
-0.65	0.05	-0.20	519	0.163372
-0.65	0.05	-0.15	495	0.165373
-0.65	0.05	-0.10	465	0.167283
-0.65	0.05	-0.05	427	0.168436
-0.65	0.05	0.00	374	0.169133
-0.65	0.05	0.05	313	0.168437
-0.65	0.05	0.10	247	0.16685
-0.65	0.05	0.15	182	0.164952
-0.65	0.05	0.20	114	0.164783
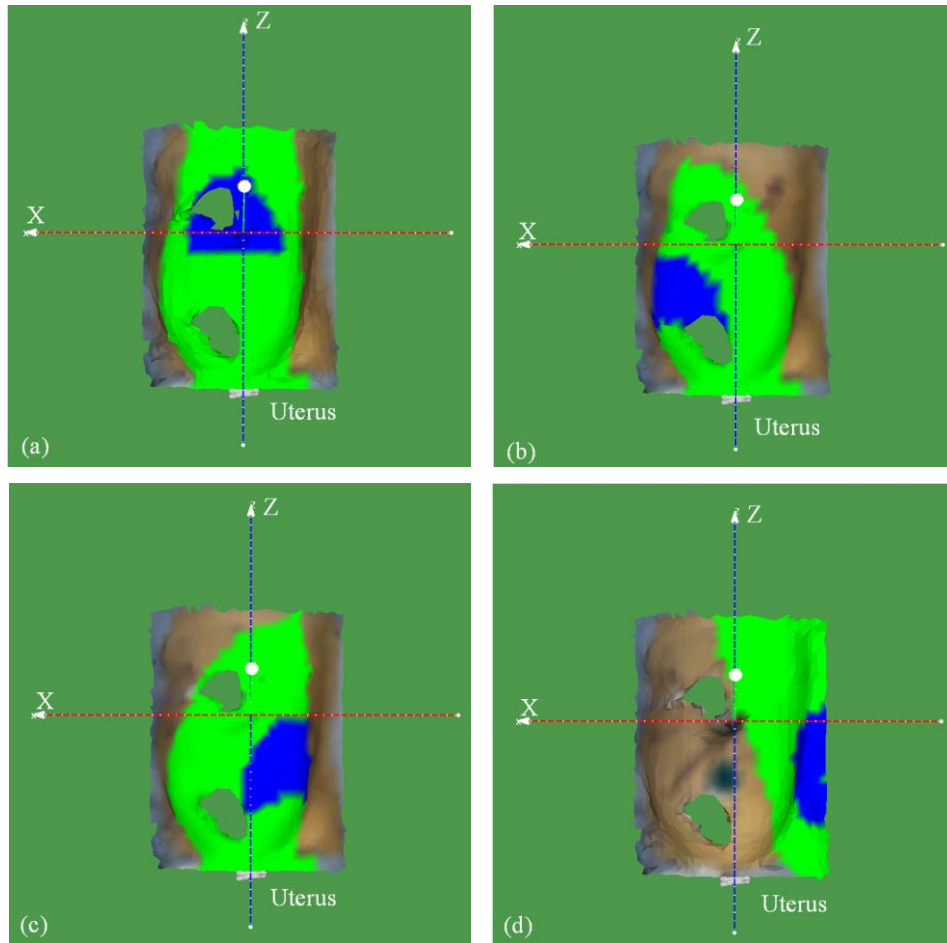
Figure 4.16 Accessible and preliminary points (in green and blue) on the Patient4 model
(a) The endoscope positioned at (0.0, 0.70, -0.30) (b) ArmNo1 positioned at (0.46, 0.45, -0.30) (c) ArmNo2
positioned at (-0.46, 0.40, -0.30) (d) ArmNo3 positioned at (-0.65, 0.05, 0.00)

To sum up, the optimal positions of the endoscope, ArmNo1, ArmNo2 and ArmNo3 are (0.0, 0.70, -0.30), (0.46, 0.45, -0.30), (-0.46, 0.40, -0.30), and (-0.65, 0.05, 0.0) respectively. The accessible and preliminary points for the endoscope and the manipulators are shown in Figure 4.16.

4.2.3 Port Placement

We calculated the optimal position of the manipulators in the previous section. The accessible points were determined for the endoscope and each of the manipulators separately. Then the accessible points were filtered by a threshold value that was a sum of the average and the standard deviation of the manipulability index of the accessible points. These points are called the preliminary points and are given to the optimization algorithm (see section 3.5) to determine the optimal position of the ports on the patients' models in section 4.2.2. The optimization algorithm minimizes the collision between the surgical tools inside the abdomen and maximizes the degree of manipulation (the efficiency index in section 3.5). In the following subsections, we calculate the optimal location of the entry ports and mark them on the patient models.

Patient1:

The preliminary points for the endoscope and the manipulators obtained in section 4.2.2 were represented on the patient model in Figure 4.17.
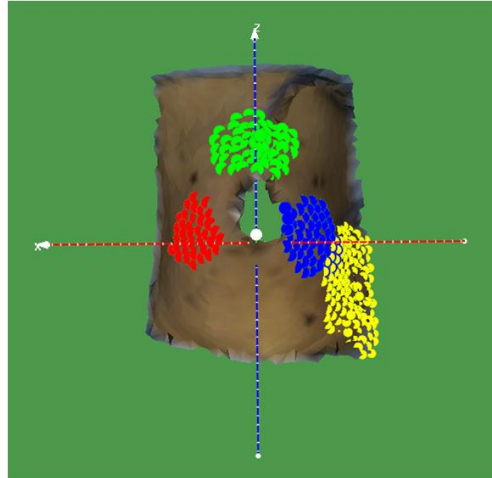
Figure 4.17 The preliminary points for the endoscope (in green), ArmNo1 (in red), ArmNo2 (in blue), and Arm3 (in yellow) on the Patient1 3D model.

In Figure 4.17, the points in red are $M(t_1)$, the points in green are $M(t_e)$, the points in blue are $M(t_2)$, and the points in yellow are $M(t_3)$. Solving equation (3.35), we obtain the Pareto optimization solution for

the optimal port location. In fact, the Pareto solution gives us four clusters of points that are the optimal positions of the endoscope, ArmNo1, ArmNo2, and ArmNo3, as depicted in Figure 4.18.

Figure 4.18 Patient1 optimal port location: the endoscope ports (in green), ArmNo1 ports (in red), ArmNo2 ports (in blue), and Arm3 ports (in yellow)

The total number of combinations of the optimal port positions for the endoscope, ArmNo1, ArmNo2, and ArmNo3 is 1490. Any subset of optimal ports' positions from these 1490 optimal arrangements (obtained from the optimization process) can be selected as entry ports on the patient's abdominal surface. For example, one of these combinations is shown in Figure 4.18, in which the ports' position for ArmNo1, the endoscope, ArmNo2, and ArmNo3 are demonstrated with "A", "B", "C", and "D" respectively.
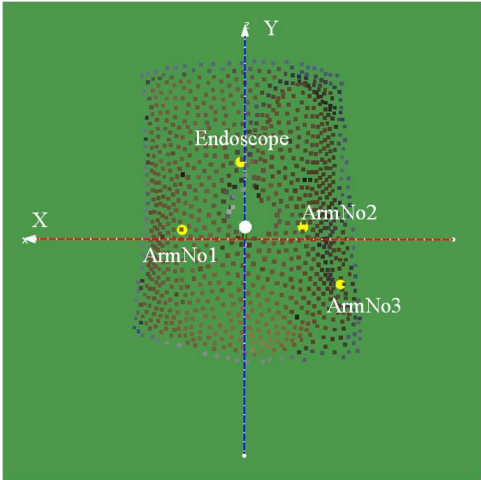
Figure 4.19 Patient1- the average of the optimal solutions for the entry ports (average of the points in each cluster)

104

The average of the points in each of the clusters (e.g. red points for ArmNo1 in Figure 4.18) can be selected as the entry ports of the related arms as shown in Figure 4.19. However, we can restrict the number of solutions (1490 combinations of the entry ports in Figure 4.18) by choosing the entry ports in order. First, the endoscope entry port is determined, and then, the locations of the ports for ArmNo1, ArmNo2, and ArmNo3 are determined respectively. We select four solutions (from 1490 combinations of the entry ports in Figure 4.18) with the highest efficiency index to determine the endoscope port. From these four combinations, the first three combinations with minimum values of the collision index between ArmNo1 and ArmNo2 are selected to determine the ArmN1 port location. Similarly, these three combinations are filtered by the first two values that minimizes the collision between ArmNo2 and ArmNo3 to determine the position of ArmNo2. Finally, from two left combinations of the entry ports, the minimum collision between ArmNo1 and ArmNo3 is selected (ArmNo1, ArmNo2, ArmNo3, and the endoscope) to determine the position of ArmNo3 as shown in Figure 4.20.
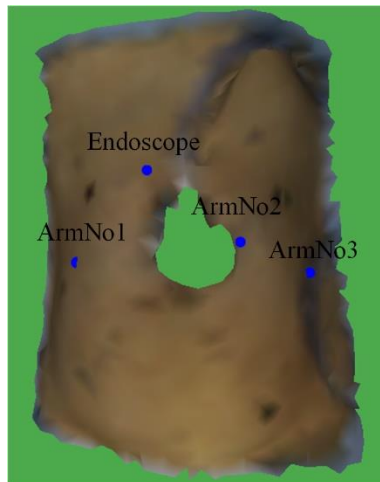
Figure 4.20 Patient1- optimal port location, obtained from selecting the ports in order

Patient2:

The optimal positions of the entry ports for the endoscope, ArmNo1, ArmNo2, and ArmNo3 (obtained from the optimization process) are shown in Figure 4.21 (a).
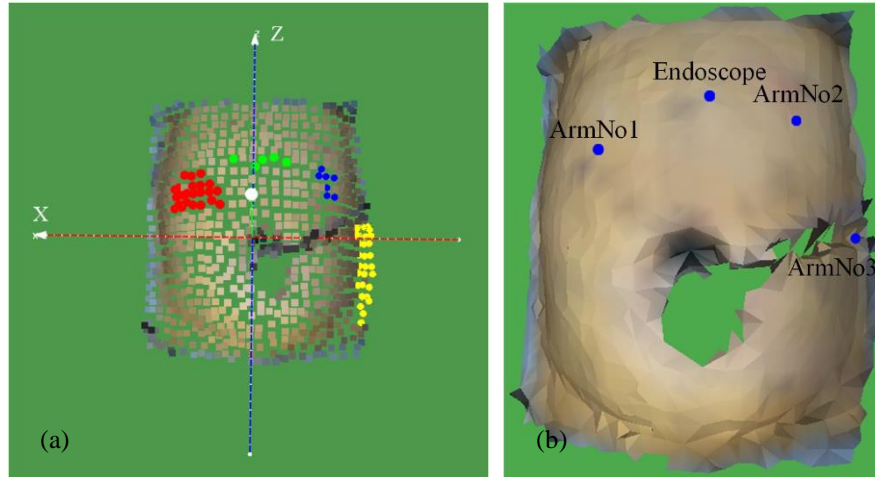
Figure 4.21 Patient2- (a) optimal ports location: the endoscope ports (in green), ArmNo1 ports (in red), ArmNo2 ports (in blue), and Arm3 ports (in yellow) (b) The final solution by choosing the ports in order

The total number of combinations of the optimal port positions for the endoscope, ArmNo1, ArmNo2, and ArmNo3 is 855. The final solution by choosing the ports in order is shown in Figure 4.21 (b).

Patient3:
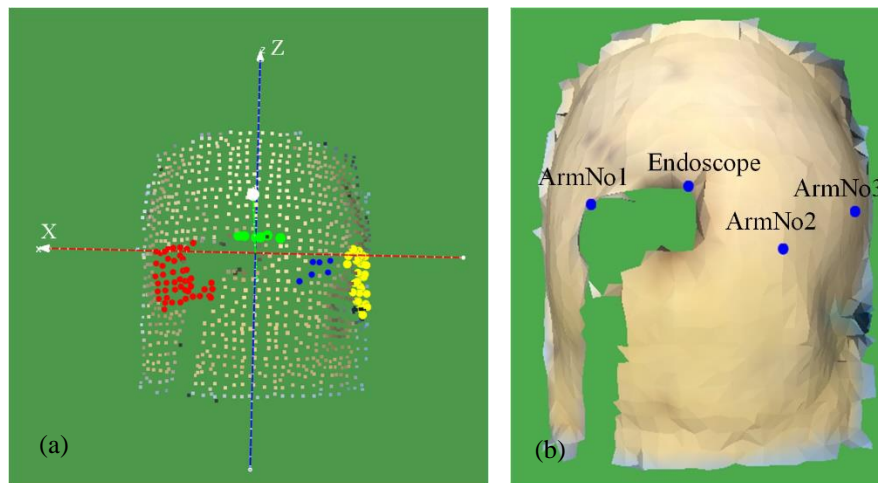
Figure 4.22 Patient3- (a) optimal port location: the endoscope ports (in green), ArmNo1 ports (in red), ArmNo2 ports (in blue), and Arm3 ports (in yellow) (b) The final solution by choosing the ports in order

The optimal positions of the entry ports for the endoscope, ArmNo1, ArmNo2, and ArmNo3 (obtained from the optimization process) are shown in Figure 4.22 (a). The total number of combinations of the optimal positions for the endoscope, ArmNo1, ArmNo2, and ArmNo3 is 1395. The final solution by choosing the ports in order is shown in Figure 4.22 (b).

The optimal position of the entry ports for the endoscope, ArmNo1, ArmNo2, and ArmNo3 (obtained from the optimization process) are shown in Figure 4.23(a).
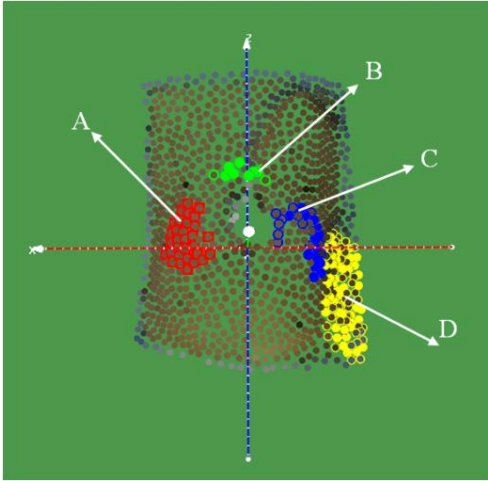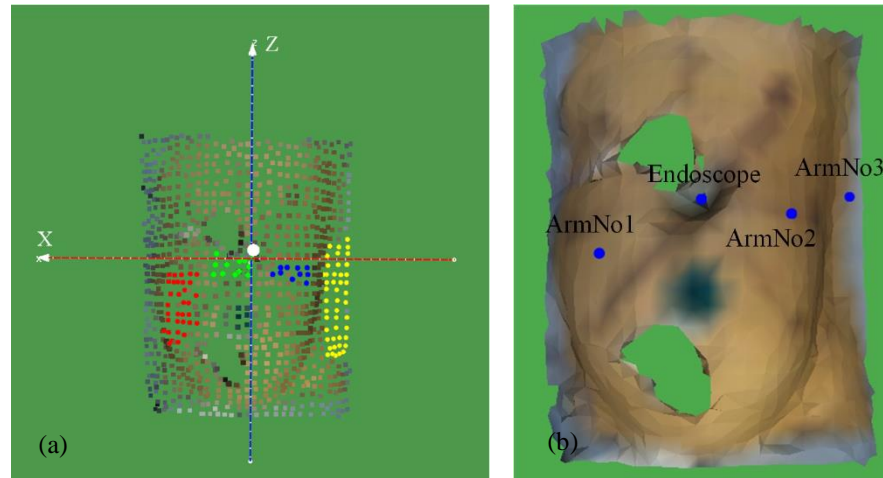

Figure 4.23 Patient4- (a) optimal port location: the endoscope ports (in green), ArmNo1 ports (in red), ArmNo2 ports (in blue), and Arm3 ports (in yellow) (b) The final solution by choosing the ports in order

The total number of combinations of the optimal positions for the endoscope, ArmNo1, ArmNo2, and ArmNo3 is 1461. The final solution by choosing the ports in order is shown in Figure 4.23 (b).

4.3   Chapter Summary

In this chapter we used our comprehensive solution for finding the optimal positions of the ports on four different patients' models. We found the optimal positions of the endoscope and the manipulators by Pareto front optimization, which is described in section 3.5. Considering the optimal positions of the manipulators for each of the patients, we calculated the optimal locations of the ports on the patients' abdominal surface. In the following chapter we will verify the calculated optimal locations by comparing the results with the optimal locations of the ports that were planned on the same patients' abdominal surface by two expert surgeons.

Chapter 5

Validation and Verification

In this chapter we verify the accuracy of our port placement system by comparing the results (optimal ports for the four patients in Chapter 4) with the actual ports' locations on the patients' bodies. Moreover, to validate the port placement system in Chapter 3, we apply our system to simulate robot docking on a body phantom to locate the ports on the phantom and compare the results with the actual ports' location when the robot (da Vinci Si) is docked to that body phantom. Finally, we use the information about the position of the targets (uterus) in seven different patient models (in Chapter 3) to predict the location and volume of the target area in hysterectomy procedures. This information is going to be used to construct the patient-specific model without constructing the internal model. We show that our estimation of the target organ's position is accurate enough to plan the ports on the patients' abdominal surface.

5.1 Verification

To verify the robustness of our designed system for planning the ports in the hysterectomy procedure, we asked two expert surgeons in Centre René Gauducheau ICO institute, Nantes-France, to mark the optimal locations of the ports on the four patients' abdominal surface in Chapter 4: Patient1, Patient2, Patient3, and Patient4 in Table 4.1. We asked the surgeons to use only the patients' external models and the CT scans for

planning the ports on the patients' abdominal surface. This is like the real condition in the operating room where they only have two sources of information: first, the shape of the patient's inflated abdomen (abdominal surface after insufflation), and second, the pre-operative medical images (CT scans).
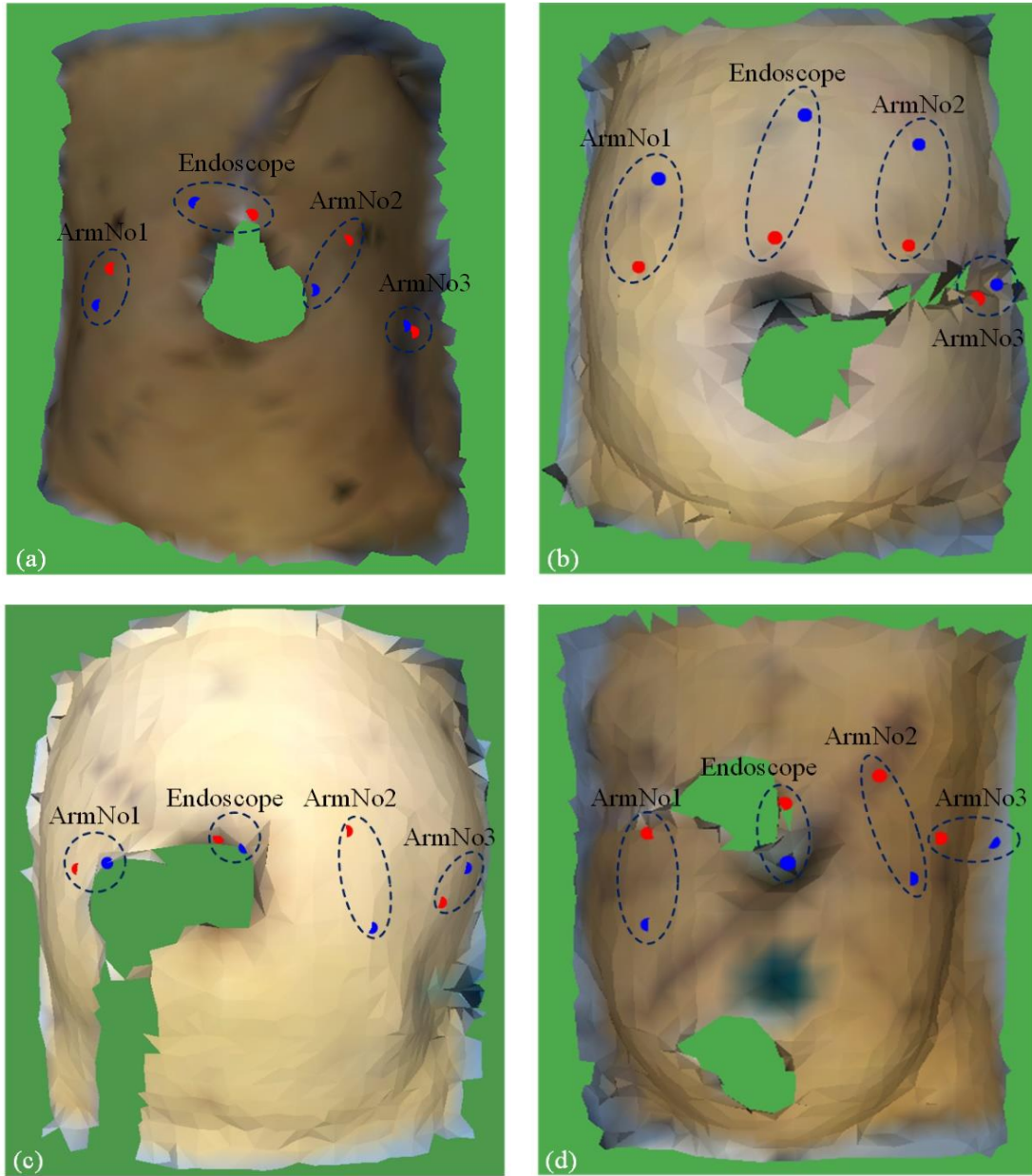
Figure 5.1 Actual ports in red and the calculated ports in blue for the endoscope, ArmNo1, and ArmNo2 on the patient model (a) Patient1 (b) Patient2 (c) Patient3 (d) Patient4

The ports' location determined by the expert surgeons, called the actual ports, for the endoscope, ArmNo1, ArmNo2, and ArmNo3 on the patients' models of Patient1, Patient2, Patient3, and Patient4 are shown as red points in Figure 5.1. We also showed the calculated optimal locations of the ports, obtained in Chapter

4, as blue points in Figure 5.1. For more accurate comparison between the computed and actual ports, we calculated the Euclidean distance between the calculated optimal ports (points in blue) and the actual points (in red) in Table 5.1.

Table 5.1 Comparison between the actual and calculated ports

	Actual			Calculated			Euclidean Distance (cm)
Patient1	X (cm)	Y (cm)	Z(cm)	X (cm)	Y (cm)	Z(cm)	
ArmNo1	7.81	-2.56	4.88	8.74	-3.31	2.46	2.69
ArmNo2	-6.12	-2.08	6.81	-4.13	-0.19	3.39	4.38
ArmNo3	-11.05	-7.09	1.31	-10.24	-5.79	1.65	1.57
Endoscope	-0.64	0.28	7.85	2.57	-0.22	8.71	3.36
Patient2							
ArmNo1	6.51	-1.84	1.67	5.65	-1.19	7.12	5.55
ArmNo2	-8.49	-1.79	3.25	-9.03	-2.29	9.56	6.35
ArmNo3	-13.18	-6.45	1.13	-15.14	-10.47	2.81	4.77
Endoscope	-1.29	-0.318	3.11	-2.65	-0.21	10.50	7.51
Patient3							
ArmNo1	9.87	-2.74	1.09	7.39	-0.36	1.11	3.43
ArmNo2	-5.34	-0.29	2.75	-6.72	-1.10	-2.25	5.24
ArmNo3	-11.01	-4.85	-0.59	-12.83	-6.59	1.65	3.36
Endoscope	1.39	-0.46	2.47	-0.02	-0.13	1.88	1.56
Patient4							
ArmNo1	9.20	-3.79	1.07	7.99	-2.33	-3.73	5.17
ArmNo2	-4.44	-2.44	3.85	-5.66	-2.95	-1.01	5.04
ArmNo3	-8.07	-5.50	1.90	-11.74	-9.41	1.87	5.37
Endoscope	1.26	-1.19	3.71	0.76	-2.71	-0.16	4.18

From Table5.1, the Euclidean distance between the position of the calculated ports and the actual ports is small for the manipulators or the endoscope in some patients. For example, in Patient3 the distance between the actual and the calculated ports for ArmNo3 is about 1.57 cm.

We already compared the average of calculated and actual ports, however, there is no evidence that shows that the computed ports are more accurate than the actual ports (planned by the surgeons on the patients' abdominal surface). In the following subsection we validate our system by computing the ports on a body phantom and compare the computed ports with the known ports (on the body phantom) that minimize the collision between the arms.

5.2 System Validation

A torso-shaped training body phantom was used to simulate the laparoscopic surgery environment as shown in Figure 5.2 (a, b). The body phantom was made from stiff plastic with some holes that are shown as black spots in Figure 5.2 (a). We used this body phantom to validate our port placement system in hysterectomy procedure as described in Chapter 3. The outer shape of the body phantom was used to simulate the inflated abdomen. A target, a small piece of soft plastic, was placed in the phantom to simulate the uterus in a hysterectomy procedure. The target was placed on a plastic made cuboid that was covered with two narrow bands of a tape (X shape) as shown in and 5.2 (c). We put the target in the middle, middle bottom, and the right corner of the base of the phantom as depicted in Figure 5.3.
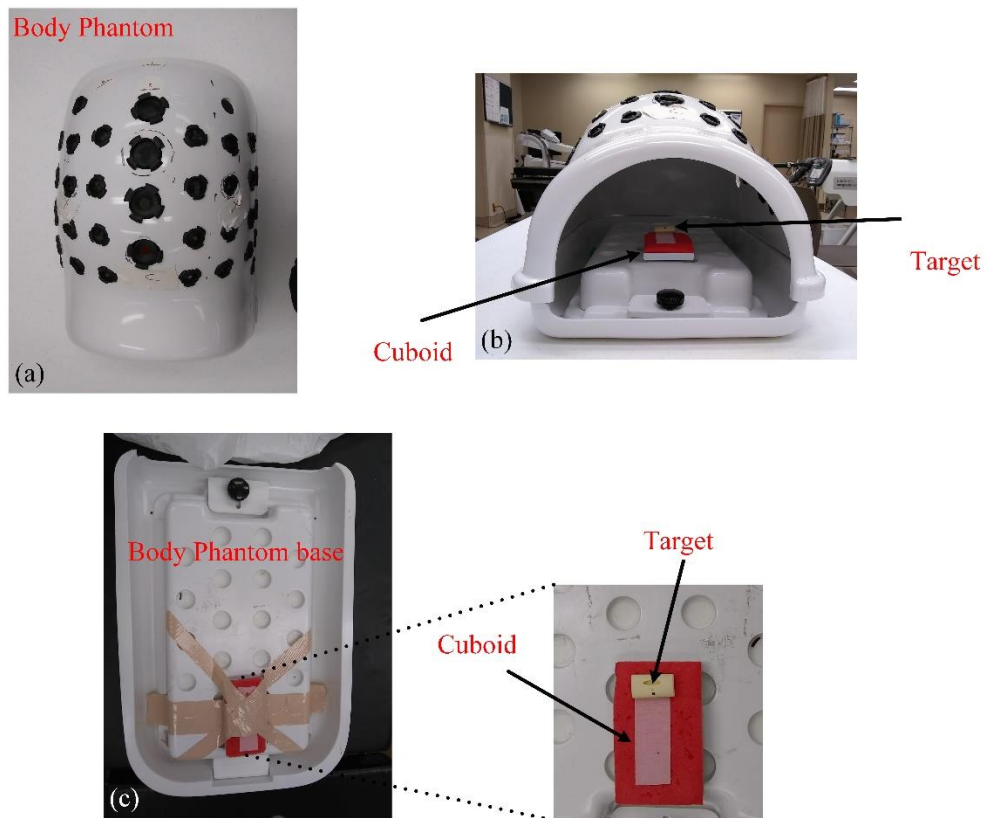
Figure 5.2 (a) The body phantom outer shape (b) The body phantom, with a target embedded (c) The body phantom base, the cuboid, and the target
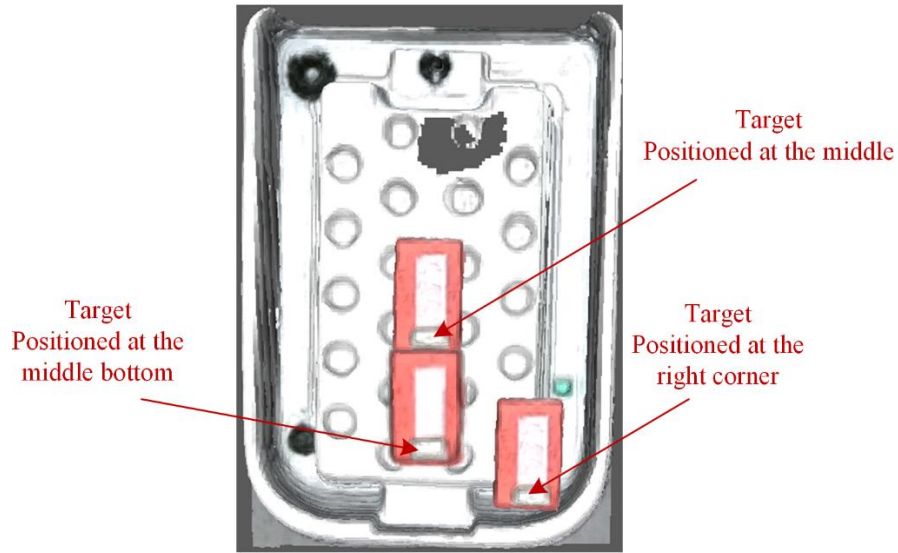
Figure 5.3 Target in different positions on the phantom base

Considering the position of the target, we set up some experiments to compare the ease of manipulating the target through the calculated entry ports (that were determined by our port placement system) with the ports that were determined by the expert surgeons.

5.2.1 Experimental Setup

The experiments were run in the Brethen Center of the Miami Valley Hospital in Dayton, Ohio. The experimental set-up, including the robot arms and the body phantom, is shown in Figure 5.4 (a). The robot position relative to the phantom are represented with "A" for the endoscope, "B" for ArmNo1, and "C" for ArmNo2 in Figure 5.4 (b).
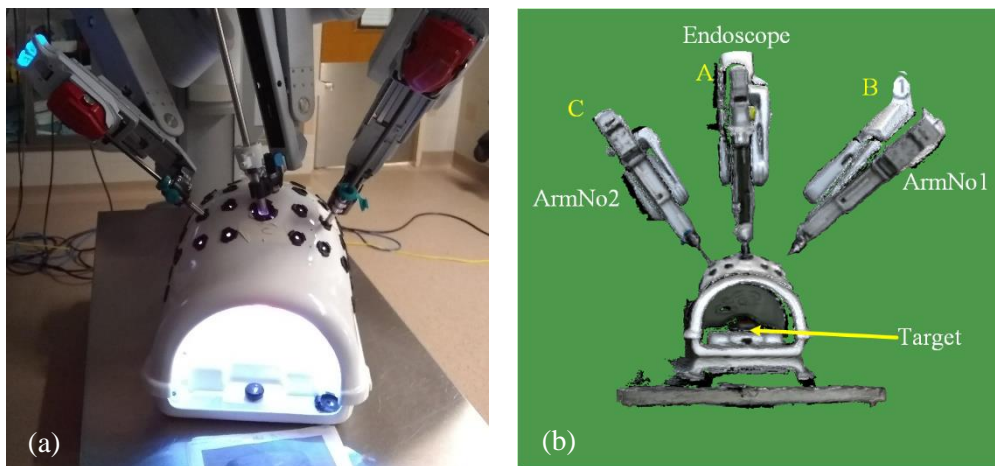
Figure 5.4 (a) The robot arms docked to the phantom (b) The position of ArmNo1, ArmNo2, and the endoscope relative to the phantom

112

The endoscope, ArmNo1, and ArmNo2 were positioned at (0, 0.75, 0), (0.46, 0.60, -0.10), and (-0.46, 0.60, -0.10) (in meter) respectively. For these given positions of the robot manipulators (A, B, and C in Figure 5.4 (b)), we used our port placement system (section 4.2.3) to determine the entry ports for each of the three positions of the target body phantom.
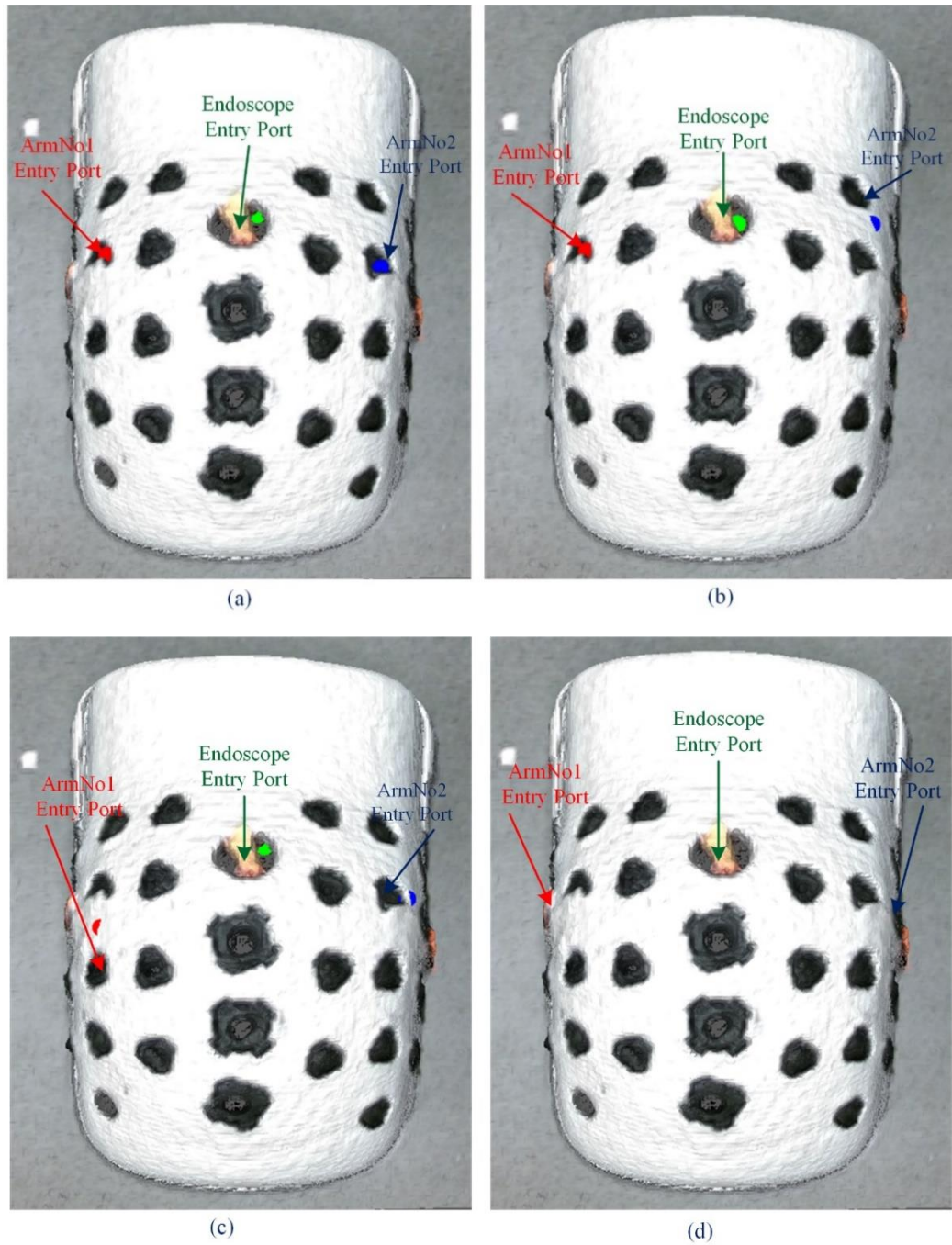
Figure 5.5 The robot entry ports: (a) Target positioned at the right corner (b) Target positioned at the middle (c) Target positioned at the bottom (d) The entry ports, determined by the surgeons

The calculated entry ports for the target position at right corner, middle, and the bottom are shown in Figure 5.5 (a), (b) and (c) respectively. The calculated entry port for ArmNo2 in Figure 5.5 (b) was aligned with none of the holes (black spots) on the body phantom, so we chose the closest hole (to the calculated entry port (blue spot)) as the entry port. Similarly, in Figure 5.5 (c), the closest holes to the red and blue points were selected as the entry ports for ArmNo1 and ArmNo2 respectively.

In addition to the calculated entry ports, two expert surgeons were asked to consider the three positions of the target (inside the phantom) to determine the optimal locations of the entry ports, called the actual ports. The actual ports on the body phantom for all the three positions of the target are shown in Figure 5.5 (d). These actual entry ports location on the body phantom were same for all three positions of the target inside the body phantom.

We designed a task item to evaluate the calculated and actual ports (Figure 5.5) for manipulating the target (Figure 5.3) by the robot arms.

5.2.2 Task

In the experiments, the surgeons were asked to use a scissor tool to cut the tape and a grasper to pick up the target from its position (the target was positioned on the cubic and covered with the X shape tape strips as shown in Figure 5.2 (c)). Similar to the hysterectomy procedure the task included cutting and removing (picking) some parts of the target by the surgical tools inside the body phantom. The task has three steps as illustrated in Figure 5.6.
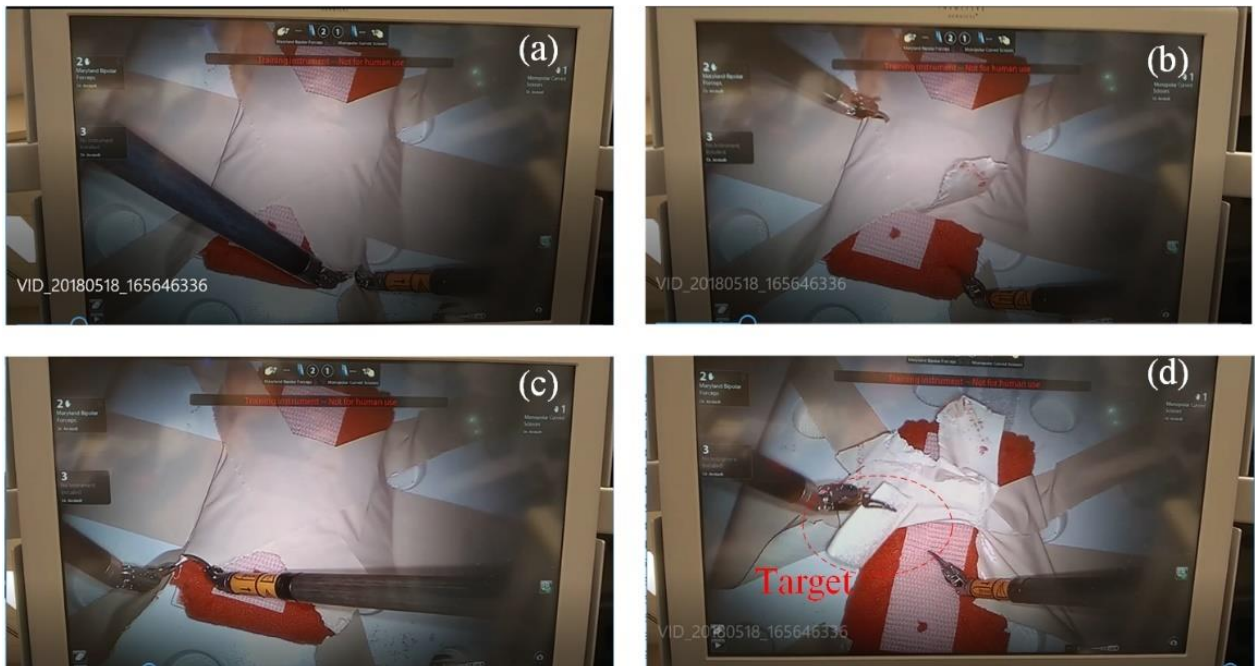
Figure 5.6 The designed task to pick the target that is covered by the X shape tape in the body phantom

First step is to cut and peel the left part of the X shape as shown in Figure 5.6 (a) and 5.6 (b). The second step is to cut and peel the right part of the X shape as illustrated in Figure 5.6 (c). Finally, the third step is to peel the center of the X shape tape away and to remove (pick up) the target as shown in 5.6 (d).

We measured the required time to complete the task to compare the calculated ports with the actual ports on the body phantom. We started with putting the target at the right corner of the base of the body phantom (Figure 5.3) and asked the surgeons to use the actual (Figure 5.5 d) and the calculate ports (Figure 5.5 a) to complete the task three times. The calculated time to complete the task with the target positioned at the right corner is shown in Table 5.2. Similarly, the calculated time to complete the task with the target positioned at the middle, and the bottom of the base are shown in Table 5.3 and 5.4 respectively.

Table 5.2 Time to complete the task for the actual and the calculated ports with the target positioned at the right corner.

	Target Position	Time to Complete the Task Using the Actual Ports (min)	Time to Complete the Task Using the Calculated Ports (min)
First Trial	Right corner	1.88	1.05
Second Trial	Right corner	1.51	1.4
Third Trial	Right corner	1.68	1.21
Mean±STD	-	1.69±0.18	1.22±0.17

Table 5.3 Time to complete the task for the actual and the calculated ports with the target positioned at the middle.

	Target Position	Time to Complete the Task Using the Actual Ports (min)	Time to Complete the Task Using the Calculated Ports (min)
First Trial	Middle right	1.52	0.75
Second Trial	Middle right	1.03	0.93
Third Trial	Middle right	1.68	0.85
Mean±STD	-	1.41±0.34	0.84±0.09

Table 5.4 Time to complete the task for the actual and the calculated ports with the target positioned at the bottom

	Target Position	Time to Complete the Task Using the Actual Ports (min)	Time to Complete the Task Using the Calculated Ports (min)
First Trial	Bottom	2.26	1.42
Second Trial	Bottom	2.05	1.18
Third Trial	Bottom	1.70	1.1
Mean±STD	-	2.00±0.28	1.23±0.16

From Table 5.2, the difference between the average of the time to complete the task (using the calculated and actual ports) is about 0.47 min. This means that the surgical tools can reach to the target easier through the calculated ports, and as a result the surgeon can complete the task faster with selecting the calculated ports. Similarly, in Table 5.3 and 5.4 the time to complete the task with selecting the calculated ports is less than the actual ports, the difference is about 0.57 min for the target positioned at the middle and 0.77 min for the target positioned at the bottom.

5.3 Reducing Pre-Operative Planning in Port Placement System

In Chapter 3 we designed a system with three main components (the patient model, the robot model and the optimization algorithm) for determining the optimal positions of the ports in laparoscopic procedures. However, each of the components (algorithms) needs a specific amount of time and effort to properly process the input data. For example, to create the 3D patient-specific model we need to correctly mark the corresponding points on the patient's abdominal surface, moreover, detecting the corresponding points in the pre-operative medical images (the internal model) is a time-consuming process.

To avoid extra processing time and the complexity of the system, we can reduce the system dependency to its components by getting enough information about the patients' size in the operating room. In this dissertation, we focused particularly on the internal model that is needed for determining the target organ's position and shape. We tried to predict the position and size of the uterus in different patients who underwent hysterectomy procedures.

The information about the uterus' position (in the reference frame) and size (for the patients in Table 4.1) is shown in Table 5.5. The size of the uterus is determined by the radius of a sphere that surrounds it as shown in Figure 3.44.

Table 5.5 Utters size and position in different patients

Patient	Uterus Position			Uterus Radius (cm)
	X (cm)	Y (cm)	Z (cm)	
Patient 1	-0.64	-13.52	-12.71	8.64
Patient 2	-1.82	-19.78	-16.33	4.81
Patient 3	1.48	-17.85	-15.53	5.29
Patient 4	0.39	-15.55	-19.84	4.71
Patient 5	2.69	-15.32	-24.03	6.97
Patient 6	-0.74	-16.61	-20.43	6.12
Patient 7	5.88	-24.24	-8.2	8.07
Average	1.03	-17.55	-16.73	6.37
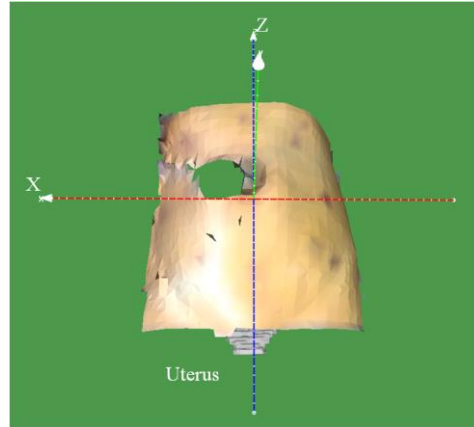
Figure 5.7 A test patient-specific 3D model.

The average uterus' position in Table 5.5 is (1.03, -17.55, -16.73), and the average radius of the uterus is 6.37 cm. We can use these average size and position of the uterus to calculate the preliminary points on any given patient model that was not listed in Table 5.5. For example, for the given patient model in Figure 5.7, called the test mode, we used the actual and estimated position and the radius of the uterus (from Table 5.5) to find the preliminary points for the endoscope arm and ArmNo1. The actual and estimated position of the uterus in the test patient model are shown in Table 5.6.

Table 5.6 The actual and estimated uterus's size and position in the test patient

	Uterus Position			Uterus Radius (cm)
	X (cm)	Y (cm)	Z (cm)	
Actual	-0.45	-17.47	-11.06	7.94
Estimated	1.03	-17.55	-16.73	6.37
Absolute Difference	1.48	0.08	5.67	1.57

We put the reference frame on the test patient's umbilicus in Figure 5.7, as the other patients in Table 5.5. From Table 5.6 the radius of the sphere that surrounds the uterus in the test patient is about 8 cm. The difference between the radius of the estimated uterus and the actual uterus is about 1.5 cm. Also, the biggest difference between the position of the estimated and the actual uterus is in Z direction, about 5.7 cm. Using both actual and estimated position of the uterus, we calculated the accessible points and the preliminary points on the test patient model as shown in Figure 5.8 (a) and 5.8 (b) for the endoscope arm.
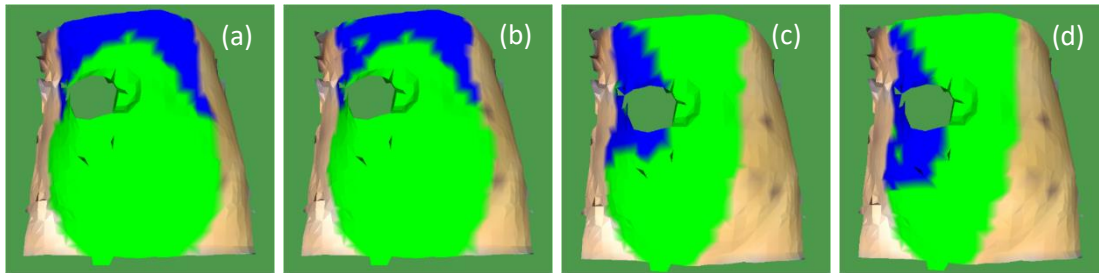
Figure 5.8 (a) the actual accessible and preliminary points for the endoscope positioned at (0.0, 0.75, 0.0)

(b) the estimated accessible and preliminary points for the endoscope positioned at (0.0, 0.75, 0.0)

(c) the actual accessible and preliminary points for ArmNo1 positioned at (0.0, 0.55, 0.0)

(d) the estimated accessible and preliminary points for ArmNo1 positioned at (0.0, 0.55, 0.0)

The accessible and the preliminary points in Figure 5.8 (a) and 5.8 (b) are almost same. This means that using the actual and estimated uterus's size and position will result in almost same position of the port for the endoscope arm. Similarly, we can show that the estimated uterus size and position can be used for determining the preliminary points for other manipulators (ArmNo1) as shown in Figure 5.8 (c) and 5.8 (d). In table 5.7 we compared the number of accessible points and the average of the manipulability index for the endoscope and the manipulators (ArmNo1 and ArmNo2) with the actual and the estimated size of the uterus.

Table 5.7 Number of the accessible points and the average of the manipulability index
with the actual and the estimated uterus' size and position.

	Actual uterus		Estimated	
	No. of the available points	The average of the Manipulability index	No. of the available points	The average of the Manipulability index
Endoscope	438	0.204	412	0.204
ArmNo1	352	0.182	331	0.180
ArmNo2	333	0.180	320	0.178

From Table 5.6, the number of the accessible points with the actual and the estimated uterus is almost same. However, for having better results with the estimated position and the radius of the uterus, we need to estimate the uterus size and position by considering more number of the patients in Table 5.5.

5.4 Chapter Summary

In this chapter we verified the optimal locations of the ports for the four patients in Chapter 4 by comparing the results with the actual positions of the ports, which were determined by two expert surgeons. We also

validated our port placement system by properly determining the known ports' location on a body phantom. Finally, we showed that having enough information (position and size) about the target organ (the uterus in the hysterectomy procedure) in different patients, we can reduce the pre-planning set-up time for constructing the patient model in laparoscopic procedures.

Chapter 6

Conclusion and Future Research

6.1 Conclusion

Robotic surgery has been the dominant method to perform most laparoscopic procedures in the operating room. The system includes a robot with three manipulators to perform the surgical task, and one endoscope arm to visualize inside the patient. The precision of manipulation with the robotic system, in comparison to traditional laparoscopic surgery, has increased magnificently. However, there are still some difficulties in the planning phase of robotic surgery. In this phase the location of the entry ports on the patient's body are determined by considering the robot position, the patient's body size, and the position of the target organ inside the patient. Surgeons usually use their experience to consider all these factors for accurate port placement in different laparoscopic procedures. However, planning the ports is a time-consuming task that even experienced surgeons complain about. Moreover, they sometimes need to replace the ports with new ones, which increases their fatigue in the operating room.

In this dissertation, we focused on hysterectomy procedures and designed a decision-aid tool for assisting the surgeon in the planning phase of robotic surgery. Using pre-operative medical images and a 3D scanner in the operating room, we created a patient-specific model that can be used as a real-time 3D model for determining the optimal location of the entry ports on the patient's abdominal surface. We simulated the robot docking on the patient-specific model, and found the optimal position of the robot arms relative to the patient by calculating the performance index of the robot manipulators. Having the optimal

positions of the robot arms, we introduced an optimization algorithm to minimize possible collisions between the surgical tools and for finding the optimal positions of the entry ports on the patient model. We verified the accuracy of our designed system by comparing the calculated ports' location with the actual ports, which were determined by two expert surgeons. Moreover, we validated the goodness of the system in correctly locating the known ports' location on a body phantom. Finally, we showed that with sufficient information about the target organ we can reduce the pre-operative planning set-up time for port placement in the hysterectomy procedure.

6.2 Limitations and Future Research Directions

In this dissertation, we presented a methodology to determine the optimal locations of the ports in hysterectomy procedure. However, there were some imitations in our research that can influence on the accuracy of the system.

For constructing the internal model, we needed high quality CT scans for the segmentation process. However, the quality of the images was out of our control since most of the patients were scanned for diagnosis purposes before they were hospitalized. Moreover, for some patients the required region of interest (uterus in hysterectomy) in the patients' bodies had not been scanned completely. In the animal study, the uterus in the pigs' bodies were not detectable in MRI images because the pigs were too young. We alternatively measured the kidneys' motion due to insufflation and applied the results to the human body for the uterus's motion. For more accurate estimation of the target organs' shift (due to insufflation), we can use MRI/CT scanning and the human subjects in the operating room. Moreover, we can predict the target organ's (uterus) size and position with using the more information from the patients in the operating room.

As we mentioned earlier, we used a least square method to superimpose the external model on the internal model. We asked the surgeons to mark four corresponding points on the patients' bodies in the operating room. The accuracy of the least square method is increased by considering more number of the corresponding points on the external and internal model. However, we had some limitations to consider more corresponding points on the patients' bodies since most of the pelvic bone and the rib cage are covered with drapes before insufflation in the operating room.

For constructing the external model, we used a Kinect device in the operating room to image the external shape of the abdominal surface after insufflation. The generated external model was not a complete mesh, because the gas tube and a trocar (and a needle), used for the insufflation, were remained in place after insufflation. As a result, the generated meshes for the external model were usually ruptured or covered by unwanted points on the abdominal surface.

As the future work, the system can be developed to work in other types of laparoscopic procedures. For example, the optimization algorithm can be developed to avoid injuries inside the patient's body in different surgical procedures. We simulated docking the *da Vinci Si* model to the patient, however, the *Xi* model can be used for the simulation in the future works. Moreover, since the non-actuated joints are adjusted manually in the operating room, the position of the actuated joints can be tracked and given to our system for more accurate port planning on the patient's body.

Bibliography

[1] Jaffray, B. "Minimally invasive surgery." Archives of disease in childhood 90, no. 5 (2005): 537-542.

[2] https://www.intuitivesurgical.com/

[3] Coste-Manière, Ève, Louaï Adhami, Fabien Mourgues, Olivier Bantiche, David Le, David Daunt, Nick Swarup, Ken Salisbury, and Gary Guthart. "Optimal planning of robotically assisted heart surgery: transfer precision in the operating room." *Experimental Robotics VIII*, pp. 424-434. Springer Berlin Heidelberg, 2003.

[4] Wang, J., Hellan, M., Lin, K., Watson, K., Galloway, M., Cao, C.G.L. (2016). "Need help with port-placement in robot-assisted surgery: a survey study". *SAGES Annual Meeting*, Boston, MA, 2016.

[5] Bañez, Jose, Stéphane Caro, Steven Schwaitzberg, Jean-Marc Classe, and Caroline GL Cao. "Modeling Patients for Optimized Port Placement in Robot-Assisted Surgery." In *ASME 2012 11th Biennial Conference on Engineering Systems Design and Analysis*, pp. 821-826. American Society of Mechanical Engineers, 2012.

[6] Simoes, Manuel, and Caroline GL Cao. "Leonardo: a first step towards an interactive decision aid for port-placement in robotic surgery." *Systems, Man, and Cybernetics (SMC), 2013 IEEE International Conference on*, pp. 491-496. IEEE, 2013.

[7] Coste-Manière, Ève, Louaï Adhami, Renaud Severac-Bastide, Adrian Lobontiu, J. Kenneth Salisbury Jr, Jean-Daniel Boissonnat, Nick Swarup, Gary Guthart, Élie Mousseaux, and Alain Carpentier. "Optimized port placement for the totally endoscopic coronary artery bypass grafting using the da Vinci robotic system." *Experimental Robotics VII*, pp. 199-208. Springer Berlin Heidelberg, 2001.

[8] Trejos, A. L., R. V. Patel, I. Ross, and B. Kiaii. "Optimizing port placement for robot-assisted minimally invasive cardiac surgery." *The International Journal of Medical Robotics and Computer Assisted Surgery* 3, no. 4 (2007): 355-364.

[9] Sun, Loi Wah, and Chung Kwong Yeung. "Port placement and pose selection of the da Vinci surgical system for collision-free intervention based on performance optimization." *Intelligent Robots and Systems, 2007. IROS 2007. IEEE/RSJ International Conference on*, pp. 1951-1956. IEEE, 2007.

[10] Chiu, Adeline M., Damini Dey, Maria Drangova, W. D. Boyd, and Terence M. Peters. "3-D image guidance for minimally invasive robotic coronary artery bypass." *Heart Surgery Forum*, vol. 3, pp. 224-231. FORUM MULTIMEDIA PUBLISHING, 2000.

[11] Yoshikawa, Tsuneo. *Foundations of robotics: analysis and control*. MIT Press, 1990.

[12] Ehrgott, Matthias. *Multicriteria optimization*. Vol. 491. Springer Science & Business Media, 2005.

[13] Sánchez-Margallo, F. M., J. L. Moyano-Cuevas, R. Latorre, J. Maestre, L. Correa, J. B. Pagador, L. F. Sánchez-Peralta, J. A. Sánchez-Margallo, and J. Usón-Gargallo. "Anatomical changes due to pneumoperitoneum analyzed by MRI: an experimental study in pigs." *Surgical and radiologic anatomy* 33, no. 5 (2011): 389-396.

[14] Schlaerth, Alan C., and Nadeem R. Abu-Rustum. "Role of minimally invasive surgery in gynecologic cancers." *The Oncologist* 11, no. 8 (2006): 895-901.

[15] Vecchio, R., B. V. MacFayden, and F. Palazzo. "History of laparoscopic surgery." *Panminerva medica* 42, no. 1 (2000): 87-90

[16] Voyles, C. Randle, Anthony B. Petro, Albert L. Meena, Alexander J. Haick, and A. Michael Koury. "A practical approach to laparoscopic cholecystectomy." *The American journal of surgery* 161, no. 3 (1991): 365-370.

[17] Reich, Harry, J. DeCAPRIO, and F. McGLYNN. "Laparoscopic hysterectomy." *Journal of Gynecologic Surgery* 5, no. 2 (1989): 213-216.

[18] Swanstrom, Lee L., and Nathaniel J. Soper, eds. *Mastery of endoscopic and laparoscopic surgery*. Lippincott Williams & Wilkins, 2013.

[19] Cadiere, Guy-Bernard, Jacques Himpens, Olivier Germay, Rachel Izizaw, Michel Degueldre, Jean Vandromme, Elie Capelluto, and Jean Bruyns. "Feasibility of robotic laparoscopic surgery: 146 cases." *World journal of surgery* 25, no. 11 (2001): 1467-1477.

[20] Zhou, Mi, and Caroline GL Cao. "Vibrotactile feedback improves laparoscopic palpation skills." In *Proceedings of the human factors and ergonomics society annual meeting*, vol. 53, no. 11, pp. 738-742. SAGE Publications, 2009.

[21] Harkki-Sirén, Päivi, and Tapio Kurki. "A nationwide analysis of laparoscopic complications." *Obstetrics & Gynecology* 89, no. 1 (1997): 108-112.

[22] Perugini, Richard A., and Mark P. Callery. "Complications of laparoscopic surgery." (2001).

[23] Miranda, Cristián S., and Antonio R. Carvajal. "Complications of operative gynecological laparoscopy." *JOURNAL-SOCIETY OF LAPAROENDOSCOPIC SURGEONS* 7, no. 1 (2003): 53-58.

[24] Magrina, Javier F. "Complications of laparoscopic surgery." *Clinical obstetrics and gynecology* 45, no. 2 (2002): 469-480.

[25] Munz, Y., K. Moorthy, A. Dosis, J. D. Hernandez, S. Bann, F. Bello, S. Martin, A. Darzi, and T. Rockall. "The benefits of stereoscopic vision in robotic-assisted performance on bench models." *Surgical Endoscopy and Other Interventional Techniques* 18, no. 4 (2004): 611-616.

[26] Moorthy, K., Y. Munz, A. Dosis, J. Hernandez, S. Martin, F. Bello, T. Rockall, and A. Darzi. "Dexterity enhancement with robotic surgery." *Surgical Endoscopy and Other Interventional Techniques* 18, no. 5 (2004): 790-795.

[27] Kaushik, Dharam, Robin High, Curtis J. Clark, and Chad A. LaGrange. "Malfunction of the Da Vinci robotic system during robot-assisted laparoscopic prostatectomy: an international survey." *Journal of endourology* 24, no. 4 (2010): 571-575.

[28] Tholey, Gregory, Jaydev P. Desai, and Andres E. Castellanos. "Force feedback plays a significant role in minimally invasive surgery: results and analysis." *Annals of surgery* 241, no. 1 (2005): 102.

[29] Cannon, Jeremy W., Jeffrey A. Stoll, Shaun D. Selha, Pierre E. Dupont, Robert D. Howe, and David F. Torchiana. "Port placement planning in robot-assisted coronary artery bypass." *IEEE transactions on Robotics and Automation* 19, no. 5 (2003): 912-917.

[30] Loulmet, Didier, Alain Carpentier, Nicola d'Attellis, Alain Berrebi, Cyril Cardon, Olivier Ponzio, Bertrand Aupecle, and John YM Relland. "Endoscopic coronary artery bypass grafting with the aid of robotic assisted instruments." *The journal of thoracic and cardiovascular surgery* 118, no. 1 (1999): 4-10.

[31] Cestari, Andrea, Nicolò Maria Buffi, Emanuele Scapaticci, Giovanni Lughezzani, Andrea Salonia, Alberto Briganti, Patrizio Rigatti, Francesco Montorsi, and Giorgio Guazzoni. "Simplifying patient positioning and port placement during robotic-assisted laparoscopic prostatectomy." *European urology* 57, no. 3 (2010): 530-533.

[32] Freschi, Cinzia, Vincenzo Ferrari, Franca Melfi, Mauro Ferrari, F. Mosca, and A. Cuschieri. "Technical review of the da Vinci surgical telemanipulator." *The International Journal of Medical Robotics and Computer Assisted Surgery* 9, no. 4 (2013): 396-406.

[33] Tabaie, Harold A., Jeffrey A. Reinbolt, W. Peter Graper, Thomas F. Kelly, and Michael A. Connor. "Endoscopic coronary artery bypass graft (ECABG) procedure with robotic assistance." In *The heart surgery forum*, vol. 2, no. 4, pp. 310-317. 1999.

[34] Adhami, Louaı. "An architecture for computer integrated mini-invasive robotic surgery: focus on optimal planning." Ph. D. Thesis, Ecole des Mines de Paris, Paris, 2002.

[35] Austad, A., Ole Jakob Elle, and Jan Sigurd Røtnes. "Computer-aided planning of trocar placement and robot settings in robot-assisted surgery." *International Congress Series*, vol. 1230, pp. 1020-1026. Elsevier, 2001.

[36] https://developer.microsoft.com/en-us/windows/kinect

[37] Feuerstein, Marco, Thomas Mussack, Sandro M. Heining, and Nassir Navab. "Intraoperative laparoscope augmentation for port placement and resection planning in minimally invasive liver resection." *IEEE Transactions on Medical Imaging* 27, no. 3 (2008): 355-369.

[38] Siewerdsen, J. H., D. J. Moseley, S. Burch, S. K. Bisland, A. Bogaards, B. C. Wilson, and D. A. Jaffray. "Volume CT with a flat-panel detector on a mobile, isocentric C-arm: Pre-clinical investigation in guidance of minimally invasive surgery." *Medical physics* 32, no. 1 (2005): 241-254.

[39] Song, Chengli, Afshin Alijani, Tim Frank, G. B. Hanna, and Alfred Cuschieri. "Mechanical properties of the human abdominal wall measured in vivo during insufflation for laparoscopic surgery." *Surgical Endoscopy And Other Interventional Techniques* 20, no. 6 (2006): 987-990.

[40] Song, Chengli, Afshin Alijani, Tim Frank, George Hanna, and Alfred Cuschieri. "Elasticity of the living abdominal wall in laparoscopic surgery." *Journal of biomechanics* 39, no. 3 (2006): 587-591.

[41] Bano, Jordan, Alexandre Hostettler, S. A. Nicolau, Stephane Cotin, Christophe Doignon, H. S. Wu, M. H. Huang, Luc Soler, and Jacques Marescaux. "Simulation of pneumoperitoneum for laparoscopic surgery planning." In *International Conference on Medical Image Computing and Computer-Assisted Intervention*, pp. 91-98. Springer, Berlin, Heidelberg, 2012.

[42] Chen, Fang, Gordon M. Brown, and Mumin Song. "Overview of 3-D shape measurement using optical methods." *Optical engineering* 39, no. 1 (2000): 10-23.

[43] Tepper, Oren M., Jacob G. Unger, Kevin H. Small, Daniel Feldman, Naveen Kumar, Mihye Choi, and Nolan S. Karp. "Mammometrics: the standardization of aesthetic and reconstructive breast surgery." *Plastic and reconstructive surgery* 125, no. 1 (2010): 393-400.

[44] Freedman, Barak, Alexander Shpunt, Meir Machline, and Yoel Arieli. "Depth mapping using projected patterns." U.S. Patent 8,493,496, issued July 23, 2013.

[45] Grzegorzek, Marcin, Christian Theobalt, Reinhard Koch, and Andreas Kolb, eds. *Time-of-Flight and Depth Imaging. Sensors, Algorithms and Applications: Dagstuhl Seminar 2012 and GCPR Workshop on Imaging New Modalities*. Vol. 8200. Springer, 2013.

[46] Smisek, Jan, Michal Jancosek, and Tomas Pajdla. "3D with Kinect." In *Consumer depth cameras for computer vision*, pp. 3-25. Springer, London, 2013.

[47] Khoshelham, Kourosh. "Accuracy analysis of kinect depth data." In *ISPRS workshop laser scanning*, vol. 38, no. 5, p. W12. 2011.

[48] Yang, Lin, Longyu Zhang, Haiwei Dong, Abdulhameed Alelaiwi, and Abdulmotaleb El Saddik. "Evaluating and improving the depth accuracy of Kinect for Windows v2." *IEEE Sensors Journal* 15, no. 8 (2015): 4275-4285.

[49] Henseler, Helga, Alina Kuznetsova, Peter Vogt, and Bodo Rosenhahn. "Validation of the Kinect device as a new portable imaging system for three-dimensional breast assessment." *Journal of Plastic, Reconstructive & Aesthetic Surgery* 67, no. 4 (2014): 483-488.

[50] Wheat, J. S., Simon Choppin, and A. Goyal. "Development and assessment of a Microsoft Kinect based system for imaging the breast in three dimensions." *Medical engineering & physics* 36, no. 6 (2014): 732-738.

[51] Newcombe, Richard A., Shahram Izadi, Otmar Hilliges, David Molyneaux, David Kim, Andrew J. Davison, Pushmeet Kohi, Jamie Shotton, Steve Hodges, and Andrew Fitzgibbon. "KinectFusion: Real-time dense surface mapping and tracking." In *Mixed and augmented reality (ISMAR), 2011 10th IEEE international symposium on*, pp. 127-136. IEEE, 2011.

[52] http://graphics.stanford.edu/data/3Dscanrep/

[53] Maddah, Mohammad R., and Caroline GL Cao. "Application of the Alpha Shape Method to Visualize and Analyze Surgical Motion." *Surgical Science* 8, no. 11 (2017): 464.

[54] https://www.artec3d.com/3d-software

[55] Schroeder, William J., Kenneth M. Martin, and William E. Lorensen. "The design and implementation of an object-oriented toolkit for 3D graphics and visualization." In *Proceedings of the 7th conference on Visualization'96*, pp. 93-ff. IEEE Computer Society Press, 1996.

[56] Yoo, Terry S., Michael J. Ackerman, William E. Lorensen, Will Schroeder, Vikram Chalana, Stephen Aylward, Dimitris Metaxas, and Ross Whitaker. "Engineering and algorithm design for an image processing API: a technical report on ITK-the insight toolkit." *Studies in health technology and informatics* (2002): 586-592.

[57] Fleischmann, Dominik, and Boas, F. Edward. "Computed tomography—old ideas and new technology." *European radiology* 21, no. 3 (2011): 510-517.

[58] Fleischmann, Dominik, Boas, F. Edward, Tye G. A., D., Sheahan, and L. Z. Molvin. "Effect of low radiation dose on image noise and subjective image quality for analytic vs iterative image reconstruction in abdominal CT." *RSNA. Chicago* (2011).

[59] Yushkevich, Paul A., Joseph Piven, Heather Cody Hazlett, Rachel Gimpel Smith, Sean Ho, James C. Gee, and Guido Gerig. "User-guided 3D active contour segmentation of anatomical structures: significantly improved efficiency and reliability." *Neuroimage* 31, no. 3 (2006): 1116-1128.

[60] Weissheimer, Andre, Luciane Macedo de Menezes, Glenn T. Sameshima, Reyes Enciso, John Pham, and Dan Grauer. "Imaging software accuracy for 3-dimensional analysis of the upper airway." *American Journal of Orthodontics and Dentofacial Orthopedics* 142, no. 6 (2012): 801-813.

[61] Kaganami, Hassana Grema, and Zou Beiji. "Region-based segmentation versus edge detection." In *Intelligent Information Hiding and Multimedia Signal Processing, 2009. IIH-MSP'09. Fifth International Conference on*, pp. 1217-1221. IEEE, 2009.

[62] Adams, Rolf, and Leanne Bischof. "Seeded region growing." *IEEE Transactions on pattern analysis and machine intelligence* 16, no. 6 (1994): 641-647.

[63] Canny, John. "A computational approach to edge detection." *IEEE Transactions on pattern analysis and machine intelligence* 6 (1986): 679-698.

[64] Amenta, Nina, Marshall Bern, and Manolis Kamvysselis. "A new Voronoi-based surface reconstruction algorithm." *Proceedings of the 25th annual conference on Computer graphics and interactive techniques*, pp. 415-421. ACM, 1998.

[65] Liu, Xu-min, Hou-kuan Huang, Wei-xiang Xu, and Jing Chen. "Research on the reconstruction method of B-spline surface based on radius basis function neural networks." In *Cybernetics and Intelligent Systems, 2004 IEEE Conference on*, vol. 2, pp. 1123-1127. IEEE, 2004

[66] Wen, P. Z., X. J. Wu, Y. Zhu, and X. W. Peng. "LS-RBF network based 3D surface reconstruction method." In *2009 Chinese Control and Decision Conference*, pp. 5785-5789. IEEE, 2009.

[67] Kazhdan, Michael, Matthew Bolitho, and Hugues Hoppe. "Poisson surface reconstruction." In *Proceedings of the fourth Eurographics symposium on Geometry processing*, vol. 7. 2006.

[68] Amenta, Nina, Sunghee Choi, and Ravi Krishna Kolluri. "The power crust, unions of balls, and the medial axis transform." *Computational Geometry* 19, no. 2 (2001): 127-153.

[69] Rogers, David F. *An introduction to NURBS: with historical perspective*. Elsevier, 2000.

[70] Ton, Duc, and Helmut Mayer. "3D least-squares-based surface reconstruction." *Photogrammetric Image Analysis PIA* 7 (2007): 2007.

[71] Edelsbrunner, Herbert, and Ernst P. Mücke. "Three-dimensional alpha shapes." *ACM Transactions on Graphics (TOG)* 13, no. 1 (1994): 43-72.

[72] Schroeder, Will J., Bill Lorensen, and Ken Martin. *The visualization toolkit: an object-oriented approach to 3D graphics*. Kitware, 2004.

[73] Kuo, Chin-Hsing, Jian S. Dai, and Prokar Dasgupta. "Kinematic design considerations for minimally invasive surgical robots: an overview." *The International Journal of Medical Robotics and Computer Assisted Surgery* 8, no. 2 (2012): 127-145.

[74] Caenen, J. L., and J. C. Angue. "Identification of geometric and nongeometric parameters of robots." In *Robotics and Automation, 1990. Proceedings., 1990 IEEE International Conference on*, pp. 1032-1037. IEEE, 1990.

[75] Banez, Jose. "Design and evaluation of a planning aid for port placement in robot-assisted laparoscopic surgery." PhD diss., Tufts University, 2012.

[76] Ferzli, G.S. and Fingerhut, A., 2004. Trocar placement for laparoscopic abdominal procedures: a simple standardized method. *Journal of the American College of Surgeons*, *198*(1), pp.163-173.

[77] Demyttenaere, Scbastian, Liane S. Feldman, and Gerald M. Fried. "Effect of pneumoperitoneum on renal perfusion and function: a systematic review." *Surgical endoscopy* 21, no. 2 (2007): 152-160.

[78] Falabella, Andres, Earl Moore-Jeffries, Michael J. Sullivan, Rebecca Nelson, and Michael Lew. "Cardiac function during steep Trendelenburg position and CO2 pneumoperitoneum for robotic-assisted prostatectomy: a trans-oesophageal Doppler probe study." *The International Journal of Medical Robotics and Computer Assisted Surgery* 3, no. 4 (2007): 312-315.

[79] Hasukić, Š. "Postoperative changes in liver function tests: randomized comparison of low-and high-pressure laparoscopic cholecystectomy." *Surgical Endoscopy and Other Interventional Techniques* 19, no. 11 (2005): 1451-1455.

[80] Knolmayer, T. J., M. W. Bowyer, J. C. Egan, and H. J. Asbun. "The effects of pneumoperitoneum on gastric blood flow and traditional hemodynamic measurements." *Surgical endoscopy* 12, no. 2 (1998): 115-118.

[81] Tunon, M. J., P. Gonzalez, F. Jorquera, A. Llorente, M. Gonzalo-Orden, and J. Gonzalez-Gallego. "Liver blood flow changes during laparoscopic surgery in pigs." *Surgical endoscopy* 13, no. 7 (1999): 668-672.

[82] Langen, K. M., and D. T. L. Jones. "Organ motion and its management." *International Journal of Radiation Oncology• Biology• Physics* 50, no. 1 (2001): 265-278.

[83] Brandner, Edward D., Andrew Wu, Hungcheng Chen, Dwight Heron, Shalom Kalnicki, Krishna Komanduri, Kristina Gerszten, Steve Burton, Irfan Ahmed, and Zhenyu Shou. "Abdominal organ motion measured using 4D CT." *International Journal of Radiation Oncology• Biology• Physics* 65, no. 2 (2006): 554-560.

[84] Suramo, I., M. Päivänsalo, and V. Myllylä. "Cranio-caudal movements of the liver, pancreas and kidneys in respiration." *Acta radiologica. Diagnosis* 25, no. 2 (1984): 129-131.

[85] Balter, James M., Randall K. Ten Haken, Theodore S. Lawrence, Kwok L. Lam, and John M. Robertson. "Uncertainties in CT-based radiation therapy treatment planning associated with patient breathing." *International Journal of Radiation Oncology• Biology• Physics* 36, no. 1 (1996): 167-174.

[86] Beyer, W.A., Fawcett, L.R., Mauldin, R.D. and Swartz, B.K., 1987. The volume common to two congruent circular cones whose axes intersect symmetrically. *Journal of Symbolic Computation*, *4*(3), pp.381-390.

[87] R Core Team (2013). R: A language and environment for statistical computing. R Foundation for Statistical Computing, Vienna, Austria. URL http://www.R-project.org/

[88] Patrick Roocks (2016). rPref: Database Preferences and Skyline Computation. R package version 1.2. URL https://CRAN.R-project.org/package=rPref

[89] Hoppe, Hugues. "New quadric metric for simplifying meshes with appearance attributes." In *Proceedings of the conference on visualization'99: Celebrating ten years*, pp. 59-66. IEEE Computer Society Press, 1999.